

**Development and Initial Evaluation of an MR Compatible Preclinical  
SPECT Insert for Simultaneous SPECT/MR Imaging**

by

Andrew Joseph Rittenbach

A dissertation submitted to Johns Hopkins University in conformity with the  
requirements for the degree of Doctor of Philosophy

Baltimore, Maryland

October, 2015

## **Abstract**

Multi-modality medical imaging systems have become increasingly important in research and clinical applications of biomedical imaging. Two complementary imaging modalities that have not yet been fully integrated into a multimodality system are Single Photon Emission Computed Tomography (SPECT) and Magnetic Resonance Imaging (MRI). To this end, our team has developed an MR compatible SPECT insert for simultaneous preclinical SPECT/MR imaging. The SPECT insert's detector is composed of five rings Cadmium Zinc Telluride (CZT) detector modules and an interchangeable cylindrical multi-pinhole (MPH) collimator. This dissertation discusses several new and significant contributions made towards the development of our SPECT insert.

We developed methods to determine optimized design parameters for MPH collimators for the SPECT insert. These methods were used to design two MPH collimators with different imaging resolutions. Simulation results demonstrated that both collimators can be used to obtain artifact-free SPECT images with the designed resolutions. We then developed novel techniques to fabricate the collimators using MR compatible materials.

Without proper system calibration and data correction, SPECT images reconstructed from data acquired with our insert exhibit poor image quality. We developed a novel energy calibration method to identify the photopeak of the gamma photons from a Tc-99m source at all 24,320 detector pixels simultaneously and a two-stage detector uniformity correction method to identify and correct for non-uniformities and malfunctioning pixels in the detector modules. Additionally, a method was developed to correct for the drift of electron-hole pairs within the detector modules due to the

Lorentz force when operating the SPECT insert inside a magnetic field. After applying the system calibration and correction methods to the acquired data, reconstructed SPECT images showed significant improvement in terms of resolution, uniformity, contrast, and artifact reduction.

Finally the SPECT insert was evaluated experimentally as a standalone SPECT system and as an insert inside an MRI system for simultaneous SPECT/MR imaging through phantom and small animal studies. The experimental results demonstrated that the SPECT insert met design specifications. Most importantly, results demonstrate that the insert can be used to obtain high quality SPECT images during simultaneous SPECT/MR image acquisition.

Dissertation Readers:

Dr. Benjamin M. W. Tsui (advisor)

Dr. Jingyan Xu

## **Acknowledgements**

There are so many people that I need to thank for helping me during my graduate studies. First and foremost, I would like to thank my advisor Dr. Benjamin M. W. Tsui for taking me on as a research assistant and giving me this amazing opportunity. I have learned so much about not just medical imaging but also how to plan and carry out long term research projects. Much of what I have learned will help me throughout my future endeavors.

I would also like to thank Dr. Jingyan Xu, not only for spending time to read this dissertation, but also for the countless hours I spent meeting with her to discuss the many projects that I have been involved with. She always found time in her busy schedule to meet with me.

The work described in this dissertation was a collaboration with the Division of MR Research in the Department of Radiology at Johns Hopkins University and Gamma Medica- Ideas, now TriFoil Imaging. I would like to thank Dr. AbdEl-Monem ElSharkawy, the late Dr. William Edelstein, Dr. James Hugg, Dr, Xiaoming Guo, Ang Liu, and Kevin Parnham for their assistance on this project.

I also need to thank Martin Stumpf; this work could not have been completed without the DMIP computer cluster, and he made sure that the cluster was up and running.

Thanks also goes to LaVahn Tunstall, for assistance with ordering needed materials and activity for all of the experiments I conducted, and to Phil Joslin for managing the accounts needed to purchase the materials.

Special thanks goes to former DMIP students Dr. Mickel Ghaly, Dr. Xing Rong, and Dr. Xiaolan Wang for the friendships that were developed in lab, in classes, and on the Johns Hopkins Shuttle.

Thanks goes out to my good friends Dr. Christopher Rock, Andrew Rock, and Kent Munson. I am happy that we managed to remain friends despite being scattered across the east coast (and for a time, the Atlantic Ocean).

I would also like to thank my parents Tom and Betsy Rittenbach, my sisters Lauren and Cynthia Rittenbach, and grandmother Josephine Welter for all of the encouragement that they have given me over the years. I hope that they are proud of the person that I have become.

Finally, I absolutely need to thank my wife, Maria Rosario Rittenbach. She has made my time in Baltimore infinitely more enjoyable and I still feel so lucky that I met her here. I love her so much and I can't wait to see where we go with our lives together. This dissertation is dedicated to her.

# Table of Contents

Abstract .....	ii
Acknowledgements .....	iv
Table of Contents .....	vi
List of Tables .....	xiii
List of Figures .....	xiv
Chapter 1: Introduction and Background .....	1
1.1. Motivation .....	1
1.2. Thesis Goal .....	3
1.3. Background .....	4
1.3.1. SPECT Imaging .....	4
1.3.1.1. Traditional SPECT Imaging System Components .....	4
1.3.1.2. Hardware used for Preclinical SPECT Imaging .....	9
1.3.1.3. Semiconductor Photon Detectors .....	12
1.3.1.4. SPECT System Calibration .....	13
1.3.1.5. ML-EM SPECT Image Reconstruction Method .....	15
1.3.2. MR Imaging .....	18
1.3.2.1. Nuclear Magnetic Resonance .....	18
1.3.2.2. MR Imaging System Components .....	20
1.3.2.3. Traditional MR Image Acquisition .....	21

1.3.3. Previous Work on Simultaneous SPECT/MR Imaging .....	22
1.3.3.1. Previous Work Conducted by Other Research Groups .....	22
1.3.3.2. Previous Work Conducted by Our Research Group.....	23
1.3.4. Improvements of Second Generation SPECT/MR System over Prototype System .....	24
Chapter 2: Methods.....	26
2.1. Design, Evaluation, and Implementation of Multi-pinhole (MPH) Collimators for the SPECT/MR System .....	26
2.1.1. Methods to Determine Final Multi-pinhole (MPH) Collimator Design Parameters .....	27
2.1.1.1. Multi-pinhole (MPH) Collimator Design Parameters .....	28
2.1.1.2. Multi-pinhole (MPH) Collimator Design Constraints.....	34
2.1.1.3. Systematic Methods to Evaluate Multi-pinhole (MPH) Collimator Designs	36
2.1.1.4. Area Based Method for Multi-pinhole (MPH) Collimator Design .....	41
2.1.1.5. Limitations of the Area Based Method.....	43
2.1.1.6. Model Based Method for Multi-pinhole (MPH) Collimator Design.....	46
2.1.1.7. Comparison of Collimator Design Methods.....	52
2.1.2. Methods to Evaluate Final Multi-pinhole (MPH) Collimator Designs Through Simulation .....	55
2.1.2.1. Analytical Simulation of Multi-pinhole (MPH) Collimator Designs.....	57
2.1.2.2. Monte Carlo Simulation of Multi-pinhole (MPH) Collimator Designs .....	59

2.1.3. Method to Implement Final Multi-pinhole (MPH) Collimator Designs .....	60
2.2. Development of Energy Calibration, Uniformity Calibration, and Lorentz Force Drift Correction Methods for the SPECT/MR System.....	63
2.2.1. Method to Acquire Detector Flood Image Used to Study SPECT/MR System Detector Energy and Uniformity Properties.....	64
2.2.1.1. Annular Shell Phantom Used to Acquire Flood Images.....	65
2.2.1.2. Measurement of SPECT/MR Detector Count Rate Performance .....	65
2.2.2. Development of SPECT/MR System Calibration and Correction Methods.....	67
2.2.2.1. SPECT/MR Detector Energy Calibration Method .....	67
2.2.2.2. SPECT/MR Detector Uniformity Calibration Method.....	71
2.2.2.3. Application of System Calibration Method to Acquired Data .....	73
2.2.2.4. Lorentz Force Drift Correction Method for Data Acquired in the Presence of a Magnetic Field .....	74
2.2.2.5. Application of System Calibration Method to Data Acquired in the Presence of a Magnetic Field.....	77
2.2.3. Evaluation of the SPECT/MR System Calibration and Correction Methods .....	78
2.2.3.1. Evaluation of System Calibration Method with Annular Shell Phantom.....	79
2.2.3.2. Evaluation of System Calibration Method with Uniform Cylinder Phantom .....	80
2.2.3.3. Evaluation of System Calibration Method with Resolution Phantom.....	81



2.2.3.4. Evaluation of System Calibration Method and Lorentz Force Correction Method with Resolution Phantom .....	83
2.3. Procedures for Experimental Evaluation of SPECT/MR System .....	84
2.3.1. Standalone SPECT Imaging of Resolution Phantom with Tc-99m .....	84
2.3.2. Standalone SPECT Imaging of Mouse Skull Tc-99m MDP .....	89
2.3.3. Standalone SPECT Imaging of Mouse Kidneys with Gadolinium Nanoparticles Labeled with Tc-99m .....	90
2.3.4. Simultaneous SPECT/MR Imaging of Resolution Phantom with Tc-99m .....	91
2.3.5. Simultaneous SPECT/MR Imaging of Mouse Kidneys with Tc-99m MAG3 ....	95
Chapter 3: Results .....	99
3.1. Results of Multi-pinhole (MPH) Collimator Design, Evaluation, and Implementation .....	99
3.1.1. Final Multi-pinhole (MPH) Collimator Designs .....	99
3.1.1.1. High Resolution Collimator Design Parameters .....	99
3.1.1.2. General Purpose Collimator Design Parameters .....	102
3.1.1.3. Final MPH Collimator Design Parameters .....	103
3.1.2. Results of Simulations Used to Evaluate Final Multi-pinhole (MPH) Collimator Designs .....	105
3.1.2.1. Simulated Analytical Projection Sets and Reconstructed SPECT Images of Resolution Phantom .....	105

3.1.2.2. Simulated Analytical Projection Sets and Reconstructed SPECT Images with MOBY Phantom .....	110
3.1.2.3. Simulated Monte Carlo Projection Sets and Reconstructed SPECT Images of Resolution Phantom.....	113
3.1.3. Final Implementation of MR Compatible MPH Collimators .....	115
3.2. Results of Evaluation of SPECT/MR System Calibration and Correction Methods	116
3.2.1. Effect of Nonstandard Detector Pixels on Flood Image Distribution .....	116
3.2.2. Results from Evaluation of System Calibration Method with Annular Shell Phantom.....	118
3.2.3. Results from Evaluation of System Calibration Method with Uniform Cylinder Phantom.....	120
3.2.4. Results from Evaluation of System Calibration Method with Resolution Phantom .....	126
3.2.5. Results from Evaluation of System Calibration Method and Lorentz Force Correction Method with Resolution Phantom.....	132
3.3. Results of Experimental Evaluation of SPECT/MR System .....	134
3.3.1. Results of SPECT Imaging Experiment with Resolution Phantom .....	135
3.3.1.1. Acquired Projection Sets of Resolution Phantom .....	135
3.3.1.2. Reconstructed SPECT Images of Resolution Phantom.....	136
3.3.1.3. Analysis of Resolution Phantom SPECT Images.....	140
3.3.2. Results of SPECT Imaging Experiment of Mouse Skull with Tc-99m MDP...	141

3.3.2.1. Acquired Projection Sets of Mouse Skull Acquired with Tc-99m MDP ...	141
3.3.2.2. Reconstructed SPECT Images of Mouse Skull Acquired with Tc-99m MDP .....	142
3.3.3. Results of SPECT Imaging Experiment of Mouse Kidneys Imaged with Gadolinium Nanoparticles Labeled with Tc-99m.....	144
3.3.3.1. Acquired Projection Set of Mouse Kidneys Acquired with Gadolinium Nanoparticles Labeled with Tc-99m .....	144
3.3.3.2. Reconstructed SPECT images of Mouse Kidneys Acquired with Gadolinium Nanoparticles Labeled with Tc-99m .....	144
3.3.4. Results of Simultaneous SPECT/MR Imaging Experiment with Resolution Phantom.....	145
3.3.4.1. Acquired Projection Sets of Resolution Phantom with Tc-99m Obtained During Simultaneous SPECT/MR Experiment .....	146
3.3.4.2. Reconstructed SPECT Image of Resolution Phantom with Tc-99m Obtained During Simultaneous SPECT/MR Experiment .....	146
3.3.4.3. Analysis of SPECT and MR Images of Resolution Phantom with Tc-99m Obtained During Simultaneous SPECT/MR Experiment .....	147
3.3.5. Results of Simultaneous SPECT/MR Imaging Experiment of Mouse Kidneys with Tc-99m MAG3 .....	150
3.3.5.1. Acquired Projection Sets of Mouse Kidneys Imaged with Tc-99m MAG3 Obtained During Simultaneous SPECT/MR Experiment .....	150

3.3.5.2. Reconstructed SPECT Image of Mouse Kidneys with Tc-99m MAG3 Obtained During Simultaneous SPECT/MR Experiment .....	152
3.3.5.3. Analysis of Image of Mouse Kidneys with Tc-99m MAG3 Obtained During Simultaneous SPECT/MR Experiment .....	154
Chapter 4: Discussion and Future Work.....	157
4.1. Discussion .....	157
4.1.1. Discussion of Collimator Design Method.....	157
4.1.2. Discussion of System Calibration Method.....	160
4.1.3. Discussion of Experimental Evaluation .....	162
4.1.4. Significant Contributions .....	163
4.1.5. Future Work .....	166
References.....	170
Curriculum Vitae .....	179

## List of Tables

Table 2.1: Design Parameters for Sample Collimators in Fig. 2.4 .....	32
Table 2.2: Simulation Parameters for Projection Sets of Resolution Phantom for HR MPH collimator (HRC) and GP MPH collimator (GPC) .....	58
Table 2.3: Parameters for Experimentally Acquired Projection Sets of Resolution Phantom for HR MPH collimator (HRC) and GP MPH collimator (GPC).....	88
Table 3.1. Final MPH Collimator Design Parameters Using the Area Based Method (black text) and Model Based Method (red text) .....	104
Table 3.2: Simulation Parameters for Projection Sets of Resolution Phantom for HR MPH collimator (HRC) and GP MPH collimator (GPC) .....	105
Table 3.3. Integral and Differential Uniformity Calculations.....	120
Table 3.4. Integral Uniformity Calculations for ROI in Uniform Cylinder Phantom ....	125
Table 3.5: Parameters for Experimentally Acquired Projection Sets of Resolution Phantom for HR MPH collimator (HRC) and GP MPH collimator (GPC).....	136
Table 3.6. Average Distance Between Rods in Image of Ultra Micro Hot Spot Phantom and Percent Error .....	140
Table 3.7 Average Distance Between Rods in Image of Resolution Phantom and Percent Error in SPECT images acquired obtained standalone SPECT and during simultaneous SPECT/MR acquisition.....	149
Table 3.8. Average Distance Between Rods in Image of Ultra Micro Hot Spot Phantom and Percent Error in MR image during simultaneous SPECT/MR acquisition.....	150

## List of Figures

Fig. 1.1. Major Components of a Gamma Camera Used for Clinical SPECT. ....	5
Fig. 1.2. Magnification and Minification Property of the Pinhole Collimator .....	12
Fig. 1.3. Steps in ML-EM image reconstruction process .....	18
Fig. 1.4. Major Components of an MRI System.....	21
Fig. 2.1. Sample cylindrical MPH collimator design for the SPECT/MR system. In this figure, the gray blocks represent detector modules, the yellow cones represent pinhole projections, the green cylinder is the MPH collimator, and the blue sphere is the MPH collimator's CVOV.....	27
Fig. 2.2. Pinhole collimator design parameters (left)- transaxial view of pinhole collimator, and (right)- sagittal view of a cylindrical pinhole collimator.....	28
Fig. 2.3. Nine pinhole collimator with multiplexed projections. The black arrow points to an example of projection multiplexing. ....	30
Fig. 2.4. Two MPH collimator designs with same target system resolution .....	32
Fig. 2.5. Space Utilization of the SPECT/MR system.....	34
Fig. 2.6. Effect of Detector Intrinsic Resolution on Pinhole Collimator Geometric Efficiency for Fixed Target System Resolution of 1 mm at Different Collimator Sleeve Radii.....	35
Fig. 2.7. System geometry used in development of area based and model based methods .....	40

Fig. 2.8. Collimator Design Results using the Area Based Method for High Resolution and GP MPH collimators .....	42
Fig. 2.9. Pinhole projection boundaries onto a flat surface (left) and a curved surface (right) .....	45
Fig. 2.10. Geometry Used to Estimate Effect of Detector Curvature on Pinhole Projection Image. When using a ring type detector, pinhole projection images will be elliptical rather than circular. The length of the projection's diameter in the transaxial direction of the detector can be estimated using the red dashed line in the figure above, while the length of the projection in the axial direction can be estimated using the orange dashed line.....	48
Fig. 2.11. The Three Steps of the Model Based Collimator Design Method. Step 1- For a given collimator sleeve radius, estimate the amount of detector area covered by a single pinhole projection. Step 2- Estimate the number of pinholes that can be placed on the central ring of the collimator. Step 3- Estimate the total number of rings of pinholes that can be used while still allowing at least half of the pinhole projection to project onto the surface of the detector. ....	50
Fig. 2.12. Collimator Design Results using the Model Based Method for High Resolution and GP MPH collimators. The black numbers near the curves show the total number of pinholes used in the collimator. ....	52
Fig. 2.13. Comparison of Area Based Method to Model Based Method for the HR MPH collimator (a), GP MPH collimator (b), and comparison estimation of total number of pinholes for the GP MPH collimator (c).....	54

Fig. 2.14. Data Spectrum Ultra Micro Hot Spot Phantom a) Phantom Geometry b) Photograph of Physical Phantom from Data Spectrum's Website .....	56
Fig. 2.15. Sample Slices of MOBY Phantom Simulating an MDP Bone scan.....	57
Fig. 2.16. Materials Used to Implement MPH Collimator a) 3D drawing of plastic collimator shell of GP MPH collimator. b) Plastic shell for GP MPH collimator. c) Tungsten pinhole inserts for HR MPH collimator. d) Tungsten pinhole inserts for GP MPH collimator .....	61
Fig. 2.17. Photograph of GP MPH collimator being filled with High Density Tungsten Powder .....	63
Fig. 2.18. Annular cylindrical shell phantom used for flood acquisition of SPECT/MR system a) Photograph of cylindrical shell phantom b) Phantom inserted into SPECT/MR detector after collimator has been removed .....	65
Fig. 2.19. SPECT/MR system detector count rate using the cylindrical shell phantom filled with Tc-99m at different levels of activity .....	66
Fig. 2.20. Acquired energy spectra from three separate detector pixels from annular shell phantom.....	69
Fig. 2.21. Sample energy spectrum for same pixel from cylindrical shell phantom (red) and phantom imaging experiment (blue) .....	70
Fig. 2.22. Effect of Lorentz force on CZT Detector Module. The charged particles produced by interaction of a gamma photon with the detector will drift inside the detector module before reaching collection circuitry. ....	75



Fig. 2.23. Sample detector module flood image acquired in the presence of a magnetic field. Direction of drift of charged particles is shown with the red arrow.....	76
Fig. 2.24. SPECT/MR System placed inside clinical MR scanner for simultaneous SPECT/MR data acquisition.....	92
Fig. 3.1. Initial (top) and Final (bottom) Pinhole Layout for HR MPH collimator using the Area Based Method.....	100
Fig. 3.2. Final Pinhole Layout for GP MPH collimator.....	103
Fig. 3.3. Analytical Simulated Projection sets of the Ultra Micro Hot Spot Phantom generated using the HR MPH collimator. For projection sets with more than one projection acquisition, the amount of collimator rotation between acquisitions is given.....	106
Fig. 3.4. Analytical Simulated Projection sets of the Ultra Micro Hot Spot Phantom generated using the and GP MPH collimator. For the projection sets with more than one projection acquisition, the amount of collimator rotation between acquisitions is given.....	107
Fig. 3.5. Simulated SPECT Images reconstructed from Analytical Projection Sets Using the HR MPH collimator.....	109
Fig. 3.6. Simulated SPECT Images reconstructed from Analytical Projection Sets Using the GP MPH collimator.....	110
Fig. 3.7. Analytical Simulated Projection sets of the MOBY Phantom generated using the HR MPH collimator (top) and GP MPH collimator (bottom).....	111

Fig. 3.8. Simulated SPECT Images of the MOBY phantom (top) reconstructed from Analytical Projection Sets Using the HR MPH collimator (lower left) and GP MPH collimator (lower right).....	112
Fig. 3.9. Simulated Monte Carlo Projection Sets of the resolution phantom using the HR MPH collimator (top) and GP MPH collimator (bottom).....	113
Fig. 3.10. Simulated SPECT Images reconstructed from Monte Carlo Projection Sets Using the HR MPH collimator (top) and GP MPH collimator (bottom).....	115
Fig. 3.11. Prototype of the HR MPH collimator (left) and the GP MPH collimator (right). .....	116
Fig. 3.12. Distribution of counts in an acquired flood image before (a) and after (b) identifying hypoactive and hyperactive detector pixels.....	117
Fig. 3.13. Sample detector module showing flood image data before (a) and after (b) applying detector uniformity calibration and pixel correction. The blue and red lines correspond to the profiles shown in Fig. 3.14.....	119
Fig. 3.14. Sample image profile across the same detector module taken before (blue) and after (red) application of uniformity correction method. ....	119
Fig. 3.15. Results of Uniform Cylinder Experiment to Evaluate System Calibration Method. (a) and (b) show projections and reconstructed SPECT of the uniform cylinder phantom before applying uniformity corrections and hypo/hyperactive pixel correction. (c) and (d) show projections and reconstructed SPECT of the uniform cylinder phantom after applying uniformity corrections but before applying hypo/hyperactive pixel	

correction. (e) and (f) show projections and reconstructed SPECT of the uniform cylinder phantom after applying uniformity corrections and hypo/hyperactive pixel correction. 121

Fig. 3.16. Image profiles taken across projection image and reconstructed SPECT image of uniform cylinder phantom. .... 124

Fig. 3.17. Results of Resolution Phantom Experiment to Evaluate System Calibration Method. (a) and (b) show projections and reconstructed SPECT of the uniform cylinder phantom before applying uniformity corrections and hypo/hyperactive pixel correction. (c) and (d) show projections and reconstructed SPECT of the uniform cylinder phantom after applying uniformity corrections but before applying hypo/hyperactive pixel correction. (e) and (f) show projections and reconstructed SPECT of the uniform cylinder phantom after applying uniformity corrections and hypo/hyperactive pixel correction. 128

Fig. 3.18. Image Profiles to Study the Effect of the System Calibration Method on reconstructed images of Resolution Phantom..... 129

Fig. 3.19. SPECT images of the Ultra Micro Hot Spot phantom reconstructed from projection sets generated without (a) and with (b) energy calibration..... 131

Fig. 3.20. Image profile across the 2.0 mm segment of the SPECT image of the Resolution Phantom with and without application of energy calibration method..... 131

Fig. 3.21. SPECT images of the Ultra Micro Hot Spot phantom reconstructed from projection sets acquired in the presence of a magnetic field without (a) and with (b) correction for drift caused by Lorentz force. .... 132

Fig. 3.22. Effect of shifting projection image acquired in the presence of a magnetic field during simultaneous SPECT/MR image acquisition by various amounts. .... 134

Fig. 3.23. Sample experimental projection acquisitions of the Ultra Micro Hot Spot Phantom using the HR MPH collimator (top) and GP MPH collimator (bottom) .....	136
Fig. 3.24. Reconstructed images of the Ultra Micro Hot Spot Phantom acquired using the HR MPH collimator with different number of projection acquisitions and ML-EM iterations.....	138
Fig. 3.25. Reconstructed images of the Ultra Micro Hot Spot Phantom acquired using the GP MPH collimator with different number of projection acquisitions and ML-EM iterations.....	139
Fig. 3.26. Sample experimental projection acquisitions of a mouse's skull obtained using Tc-99m MDP Bone scan Study using the (top) HR MPH collimator and (bottom) GP MPH collimator .....	142
Fig. 3.27. Reconstructed SPECT Images of mouse skull obtained using Tc-99m MDP using the (top) HR MPH collimator and (bottom) GP MPH collimator.....	143
Fig. 3.28. Sample experimental projection acquisition of a mouse kidney acquired using gadolinium nanoparticles labeled with Tc-99m.....	144
Fig. 3.29. Reconstructed SPECT Images of mouse kidney obtained using gadolinium nanoparticles labeled with Tc-99m.....	145
Fig. 3.30. Projection Image of Resolution Phantom Acquired During Simultaneous SPECT/MR Study.....	146
Fig. 3.31. Reconstructed SPECT images of Ultra Micro Hot Spot Phantom acquired during simultaneous SPECT/MR study .....	147

Fig. 3.32. Reconstructed SPECT images of Resolution Phantom acquired during (left) standalone SPECT acquisition and during (right) simultaneous SPECT/MR image acquisition.....	148
Fig. 3.33. Simultaneously Acquired SPECT and MR Images of the Ultra Micro Hot Spot Phantom. SPECT Image (left), MR Image (center), Fused Image (right).....	149
Fig. 3.34. Static projection image of mouse kidney obtained using Tc-99m MAG3 during simultaneous SPECT/MR imaging experiment.....	151
Fig. 3.35. Projection Images from First Ten Frames of MAG3 Study to Reconstruct a Dynamic Image.....	152
Fig. 3.36. Reconstructed static MAG3 SPECT image of mouse kidneys (top) and MR image of kidneys averaged from 22 dynamic MR frames (bottom).....	153
Fig. 3.37. Dynamic Images From SPECT/MR MAG3 study (top) First Ten Frames of Reconstructed SPECT Image (bottom) First Three Frames of Acquired MR Image.....	154
Fig. 3.38. Fusion of static SPECT and MR images from MAG3 experiment.....	155
Fig. 3.39. First three frames of fused dynamic SPECT and MR images from MAG3 experiment.....	155
Fig. 3.40. Time activity curve generated from dynamic SPECT/MR Tc-99M MAG3 study.....	156

# **Chapter 1: Introduction and Background**

## **1.1. Motivation**

During the past decade, multimodality imaging systems have become increasingly important in the biomedical imaging field [1]. Multimodality imaging systems combine two or more imaging modalities that provide complementary information about the patient being imaged. This information is used by imaging scientists to improve the quality of the images, by biomedical researchers to better understand the biomedical processes, and by physicians to make better diagnoses, treatment and management of their patients. For example, physicians can use Positron Emission Tomography/Computed Tomography (PET/CT) systems to obtain functional information from the PET images and anatomical information from the CT images. Furthermore, the CT images can also be used for attenuation correction of the PET images for improved image quality and quantitation [2].

Research on multimodality systems began with Single Photon Emission Computed Tomography/Computed Tomography (SPECT/CT) systems [3, 4] and later with PET/CT systems [5, 6]. In time, both of these multimodality systems became widely accepted and have since been put into clinical use [7-9]. Recently, there have been growing interests in the development of multimodality systems that combine nuclear medicine and magnetic resonance (MR) imaging. Dual-modality PET/MR systems have been developed by the major manufacturers of medical imaging systems [10, 11]. One particularly exciting development of PET/MR imaging is the ability to acquire static and dynamic PET and MR images simultaneously [12]. However, dual-modality SPECT/MR

systems remain in the research stage, although there are many reasons why simultaneous SPECT/MR imaging would be beneficial to both researchers and physicians [13].

There are several advantages of using an additional modality when conducting SPECT imaging. First, SPECT is a functional imaging modality. While it can obtain high quality images of changes in brain activity, track the flow of blood through the heart, or determine whether a kidney is working properly, SPECT is not capable of providing high quality anatomical images. Just as SPECT systems cannot provide high quality anatomical images, CT systems cannot provide high quality functional images. This is the major advantage of a SPECT/CT system. A SPECT/CT system also allows more accurate registration of the SPECT and CT images and the resulting fused image provides more information than either image would have provided on its own.

Like a CT system, an MRI system is also capable of providing high quality anatomical images. However, an important advantage of MRI over CT is that the MRI system does not utilize ionizing radiation as compared to a CT system where x-ray radiation is used. As a result the radiation dose given to the patient is limited to what is required to obtain the SPECT image. Another advantage of MRI over CT is that MR is capable of obtaining high contrast images of soft tissue, something that cannot easily be obtained using CT. In addition, ongoing research in utilizing MR images for attenuation correction in PET reconstruction in PET/MR [14] will also benefit SPECT/MR in improving the quality and quantitative accuracy of SPECT images. However, before the application of SPECT/MR can truly begin, it is first necessary that we develop a SPECT/MR system capable of obtaining high quality simultaneous SPECT/MR images.

## 1.2. Thesis Goal

The design and development of a simultaneous SPECT/MR imaging system is a significant undertaking, requiring a team with a wide range of expertise including detector electronic design, SPECT and MR imaging physics, image reconstruction methods, mechanical engineering, and biomedical application scientists. This thesis details the significant contributions made towards the development of an MR compatible SPECT insert for simultaneous SPECT/MR imaging of small animals. A brief description of the significant results discussed in this thesis will now be given.

We developed two methods to systematically determine the design of the MPH collimators for the SPECT/MR system. These methods allowed us to determine, for a target system resolution, the MPH collimator design parameters that maximized the collimator's geometric efficiency at the center of the MPH collimator's field-of-view and were used to design two collimators. Simulated projection and reconstructed SPECT images were generated to evaluate the collimator designs. Prototypes of each collimator designs were implemented using nonmagnetic materials and were used for SPECT imaging.

The detector of the SPECT/MR system discussed in this thesis consists of 95 Cadmium Zinc Telluride (CZT) modules with 24,320 total detector pixels. A novel system calibration method was developed to accurately identify the energy of detected gamma photons at all detector pixels simultaneously. Furthermore, we also developed a two-stage uniformity calibration method to identify and correct for detector non-uniformity and dead, hypoactive, and hyperactive pixels. Additionally, a method to correct for the drift of charged particles within the system's detector modules during



simultaneous SPECT/MR image acquisition was also developed. SPECT images were reconstructed from acquired data with and without application of the system calibration and correction methods. When applied, reconstructed images showed significant improvement in terms of resolution, uniformity, contrast, and artifact reduction.

Furthermore, a series of experiments were conducted in our initial evaluation of the system, ranging from standalone SPECT phantom studies to a dynamic simultaneous SPECT/MR live animal study. Experimental results show our system can obtain high quality SPECT and MR images simultaneously.

## **1.3. Background**

### **1.3.1. SPECT Imaging**

#### **1.3.1.1. Traditional SPECT Imaging System Components**

This section will briefly discuss the major components of traditional clinical SPECT systems and describe how SPECT images are acquired. The information summarized in this section can be found in greater detail in [15-17]. As mentioned, SPECT is a functional imaging modality. At the start of a SPECT procedure, a radiopharmaceutical, which is a drug designed to uptake in a specific body part, such as bone, heart, or kidneys, is given to the patient. This drug is attached to a radionuclide such as Tc-99m, Tl-201, or I-123, which will emit gamma photons at known energies as the radionuclide decays. During clinical SPECT image acquisition, the SPECT system's detectors will rotate about the patient to acquire projection images from the emitted gamma photons at many different angles. The acquired projection images are then used to reconstruct a SPECT image, which is a 3D tomographic image of the distribution of the radiopharmaceutical inside the patient. From these images, physicians can determine

whether the organ being imaged is functioning properly, or whether the patient has an illness. During clinical SPECT acquisition, projection images are obtained using a detector known as a gamma camera. The main components of a gamma camera are shown below, in Fig. 1.1.

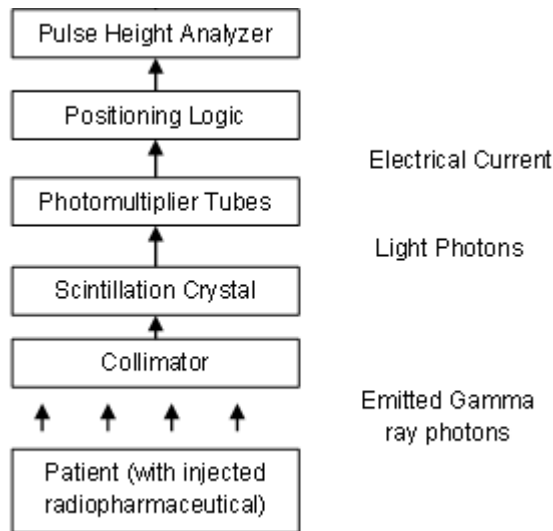


Fig. 1.1. Major Components of a Gamma Camera  
Used for Clinical SPECT.

The method used to acquire the projection images with a gamma camera will now be described. Because the radionuclide attached to the radiopharmaceutical given to the patient will emit gamma photons uniformly in all directions, it is necessary to use a collimator to limit which emitted photons are used to form each projection image. Collimators are used to attenuate photons traveling in a direction that is not desired for image formation. As an example, for typical clinical SPECT image acquisition, a parallel-hole collimator is used. The parallel-hole collimator consists of a grid with many tiny openings and is constructed out of a material with a high attenuation coefficient, such as lead, and is placed over the detector surface. This type of collimator is designed to attenuate photons that do not travel along a perpendicular, or nearly perpendicular,

path from the patient to the detector. Photons attenuated by the collimator will not contribute to the image that is formed. On the other hand, photons that pass through the parallel holes of the collimator and reach the detector, photons that penetrate the collimator, and photons that scatter from the collimator and reach the detector, all contribute to the acquired projection image. These photons are detected by the gamma camera through an indirect conversion process. In this process, detected gamma photons are first used to generate light photons, which are then used to generate a measurable electrical signal. The hardware components in a gamma camera that carry out this process will now be described.

Most of the gamma photons that pass through the collimator are absorbed by a scintillation crystal; the exact percentage depends on the type of crystal used as well as the crystal's thickness. After the absorption, the scintillation crystal emits light photons. These light photons are then detected by photomultiplier tubes which use the light photons to produce a measurable electrical signal. A photomultiplier tube consists of a photocathode followed by a series of dynodes that are held at successively higher voltage levels. After the light photons emitted from the scintillation crystal are absorbed by the photocathode, electrons are released. These electrons are then drawn to the first dynode. For each electron that hits the dynode, three to six new electrons are released. The new electrons are then drawn to the second dynode, which is held at a higher voltage than the first dynode is. This pattern repeats several times, and when the electrons have reached the anode of the photomultiplier tube, the number of electrons has been multiplied by  $10^6$  to  $10^8$ , which is a sufficient number of electrons to produce an electrical signal. This signal is sent to positioning circuitry to determine the location on the detector where the

gamma photon interacted with the crystal and a pulse height analyzer to determine the gamma photon's energy.

Whenever an electrical signal is received by the pulse height analyzer, the signal is shaped into a pulse and the pulse's height is measured. The pulse's height is proportional to the energy of the gamma photon that produced the pulse. Therefore, the pulse height analyzer is used to identify detected gamma photons that have been scattered due. Gamma photons emitted by the radiopharmaceutical can be scattered inside the patient, inside the collimator, or even inside the detector. Scattered gamma photons do not accurately represent where the radiotracer is distributed in the patient, because the photons are detected at a different position on the detector than where they were emitted from the patient. If scattered photons are included in the projection image produced by the detector, image contrast is reduced. However, when a gamma photon undergoes Compton scattering, it loses some of its energy. The greater the angle that the gamma photon is scattered, the more energy the gamma photon will lose. Therefore, because the energy of the gamma photons emitted by the radiopharmaceutical is known, the pulse height analyzer electronics can be configured to reject scattered photons.

Depending on how data is being acquired, the detected scattered photon is handled in different ways. In frame mode acquisition, a window that determines a range of energies that will be accepted is determined prior to data acquisition. Detected photons with energy that falls above or below this range will be rejected. In this thesis, all experimental data was acquired in a list-mode format. In list-mode format, the position, energy and time of each photon that hits the detector and detected are stored. The list-mode data can later be binned in various ways to generate projection images created by

photons within a particular energy range, or detected during a particular time. In both formats, detected photons are used to produce a projection image, where each pixel in the image corresponds to the number of photons detected by the detector at that pixel's location. The resolution of this image depends on both the design parameters of the collimator and the thickness of the scintillation crystal, although the collimator typically has a much greater influence on image resolution than the crystal thickness does.

To obtain projection images at different angles, a clinical SPECT detector is typically attached to a gantry which allows it to rotate around the patient. The total number of projection images that are obtained during the SPECT procedure varies depending on the procedure that is being performed. The complete set of projection images are used to produce a tomographic reconstruction of the distribution using image reconstruction methods.

Over time, many different image reconstruction methods have been developed; these methods fall into two main categories, analytical reconstruction methods and iterative reconstruction methods. When using the same acquired projection images, a subset of iterative reconstruction methods, called statistical iterative reconstruction methods are designed to produce reconstructed images with lower noise than an image reconstructed using an analytical method [18]. This occurs for several reasons. While analytical methods are theoretically exact, they cannot be implemented exactly, as the equations used to derive analytical image reconstruction methods are continuous. Furthermore, the mathematics used to derive analytical image reconstruction methods does not take degradations of the data due to noise or the physics of the imaging process into account. When using iterative reconstruction methods, any aspect of the imaging

process can be modeled and included in the reconstruction method, including the physics of the imaging process that degrade acquired data. For these reasons, in this thesis the statistical iterative reconstruction method ML-EM, which will be discussed later in Section 1.3.1.5, was used.

### 1.3.1.2. Hardware used for Preclinical SPECT Imaging

Projection images acquired with parallel hole collimators will be the same size as the object being imaged [15]. This property of the parallel-hole collimator causes difficulties when using a parallel-hole collimator to image small objects. Because the size of the projection image will be the same size as the object being imaged, it is likely that a significant portion of the detector surface will remain unused. Moreover, if the small object has details that are finer than the detector's intrinsic resolution, it will be impossible to image them regardless of the resolution of the collimator that is used. The pinhole collimator, which is largely used in today's state of the art preclinical imaging systems [19-23], can be used to alleviate these difficulties. A well designed pinhole collimator can be used to obtain a high resolution projection image of a small volume while still maintaining a high geometric efficiency. Single pinhole collimators consist of an opening with a diameter in the submillimeter to millimeter range surrounded by a cone constructed of a dense attenuating material. Only photons that pass through the opening of the cone reach the detector at the cone's base. The imaging properties of the pinhole collimator are well known and are given in Equations (1-4) [24].

$$R_p = \frac{D_e(L + Z)}{L} \quad (1)$$

$$G = \frac{D_e^2 \cos\left(\frac{\theta}{2}\right)^3}{16Z^2} \quad (2)$$

$$D_e = \sqrt{D \left( D + \frac{2}{\mu} \tan\left(\frac{\theta}{2}\right) \right)} \quad (3)$$

$$R_s = \sqrt{R_p^2 + R_i^2 \left(\frac{Z}{L}\right)^2} \quad (4)$$

In these equations,  $L$  is the distance from the pinhole to the detector and is known as the focal length.  $Z$  is the distance from the pinhole to the center of the collimator's field-of-view and is known as the collimator radius.  $D$  is the pinhole aperture's diameter, and  $\theta$  is the cone angle of the pinhole. Equations 1 and 2 describe how to calculate the resolution and geometric efficiency of a pinhole collimator. Equation 3 describes one method of calculating the effective aperture of a pinhole collimator. This equation is used to take into account the fact that photons can potentially penetrate a pinhole collimator at the pinhole's edges. The amount of penetration that occurs depends on the linear attenuation coefficient of the material used to construct the pinhole collimator. It should be noted that Equation 3 is a simple model for photon penetration. In the above equations, the same effective aperture is used in the calculation of both the collimator's resolution and geometric efficiency. More rigorous models for photon penetration have been developed that use different effective apertures for calculation of resolution and geometric efficiency. [25, 26]. Equation 4 describes the resolution an imaging system using a pinhole collimator will be able to obtain, taking into account the intrinsic resolution of the imaging system's detector.

When designing a pinhole collimator, the key design parameters are the pinhole diameter, the pinhole cone angle, the collimator focal length, and the collimator radius. As seen in Equations 1 and 2, the diameter of the pinhole collimator determines the

collimator's resolution as well as its geometric efficiency. A larger pinhole diameter will improve the collimator's geometric efficiency, but also cause the collimator's resolution to degrade. The pinhole cone angle determines the pinhole collimator's field of view. For a pinhole collimator with a fixed pinhole diameter, focal length, and collimator radius, the larger the pinhole cone angle the larger the collimator's field of view will be. As seen in Equation 2, the collimator radius is the other collimator parameter that determines the collimator's geometric efficiency. As the pinhole is closer to the object being imaged, geometric efficiency will increase. Finally, in addition to the diameter of the collimator's aperture, the collimator's radius and focal length also determine the collimator's resolution. The ratio of the collimator's focal length to the collimator's radius plays an important role in the design of a pinhole collimator. This relationship will now be discussed.

Unlike a parallel-hole collimator, the projection image produced by a pinhole collimator is not the same size as the object that was imaged. The size will vary depending on the ratio of the focal length to the collimator radius [19]. If the focal length is greater than the collimator radius, the projection image will be magnified, and the projection image will be larger than the object. Magnification allows small details in the object being imaged to spread across a wider area of the detector surface. This property enables a system using a pinhole collimator to potentially obtain a SPECT image at a higher resolution than the system detector's intrinsic resolution. Conversely, if the focal length is smaller than the collimator radius, the projection image will be minified and the projection image will be smaller than the object. Minification has been used to design collimators with multiple pinholes to obtain several projection images simultaneously



onto a small detector [27]. In both cases, the projection image produced by a pinhole collimator is inverted with respect to the object. Fig. 1.2 shows the imaging properties of a pinhole collimator.

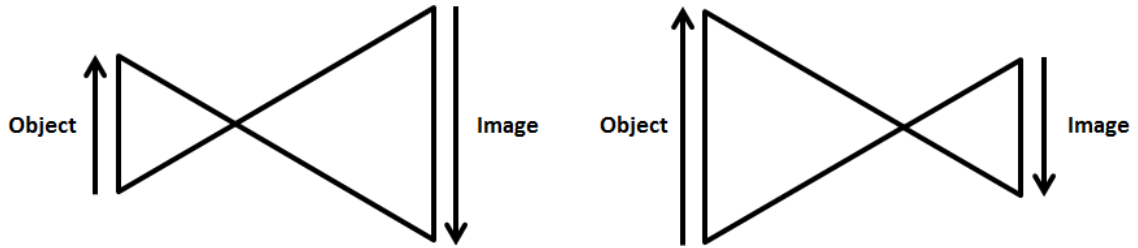


Fig. 1.2. Magnification and Minification Property of the Pinhole Collimator

### 1.3.1.3. Semiconductor Photon Detectors

Semiconductor photon detectors are an alternative to the scintillation detectors used in traditional SPECT imaging systems. [15, 28]. With this type of detector, a piece of semiconductor crystal such as Cadmium Zinc Telluride (CZT) is held in between a cathode and an anode. When a gamma photon interacts with the semiconductor, ionization occurs and the electrons produced are pulled towards the anode and are measured as a current. By pixelating the detector, the position that the photon interacted with the detector can be determined. Semiconductor detectors are capable of achieving higher energy resolution than traditional scintillation detectors can, which allows for improved differentiation of photons with different energies. However, semiconductor detectors are not widely used in clinics due to the costs and difficulties to grow a semiconductor crystal at a low cost to the size that is needed for clinical SPECT imaging.

One of the initial challenges in this work was determining what sort of detector would be used for the SPECT/MR system. As will be discussed in Section 1.3.2, a strong uniform magnetic field is needed for acquisition of MR images. Unfortunately, traditional scintillation detectors that utilize photomultiplier tubes are highly susceptible to strong

magnetic fields and are not MR compatible. This is because of a physical property called the Lorentz force [29]. As shown in Equation 5, the presence of a magnetic field produces a force on moving charged particles. As discussed earlier, scintillation detectors produce a measurable electrical signal through the use of photomultiplier tubes (PMTs). For PMTs to function properly, the electrons produced at the photocathode are accelerated and amplified through a series of dynodes and finally reach the anode of the PMT. When a PMT is operating in the presence of a strong magnetic field, an additional force, mainly the Lorentz force, given by

$$\vec{F} = q(\vec{E} + \vec{v} \times \vec{B}) \quad (5)$$

will act on and deflect the fast moving electrons inside the PMT and severely affect its performance. In this equation, F is force, q is the charge of the particle, E is electric field strength, v is the velocity of the charged particle, and B is magnetic field strength. As a result, scintillation based detectors that use photomultiplier tubes are not MR compatible.

Studies have shown that, unlike traditional scintillation detectors coupled to PMTs and typically used in gamma cameras, the imaging performance characteristics of semiconductor detectors is not significantly impacted when operating in the presence of a magnetic field [30, 31]. While both semiconductor detectors and scintillation detectors are affected by the Lorentz Force, the effect of the Lorentz Force in a semiconductor detector can be corrected for, as will be shown in chapters two and three. The same cannot be said for scintillation based detectors that use photomultiplier tubes.

#### **1.3.1.4. SPECT System Calibration**

Before a SPECT system's detector can be used to acquire usable projection images, there are several issues that need to be corrected for first. One important issue is

the correction of detector nonuniformity [15]. Detector nonuniformity can be caused by variations in the detector's electronics as well as variations in the sensitivity in different regions of the detector. Without correcting for the non-uniformities in acquired data, the non-uniformities will produce artifacts in SPECT images acquired with the detector. One well known artifact caused by non-uniformities are ring artifacts [32, 33]. These artifacts are particularly visible when imaging what would otherwise be a uniform object. Depending on the position of the defect, detector non-uniformity will cause the reconstructed image to have a variation in the image's pixel intensity, making what was supposed to be a uniform part of an image non-uniform. For pinhole collimators, if the non-uniformity is at the center of the detector, the artifact will appear in the shape of a circle. However, as the uniformity is moved away from the center of the detector, the artifact will appear in the shape of a ring, the diameter of which will depend on the position of the non-uniformity on the detector.

There are two ways that uniformity of a detector can be measured [15]. The intrinsic uniformity of a detector is measured when the collimator is removed, while the extrinsic uniformity is measured when the collimator is attached to the detector. To measure the uniformity of a detector, a flood field image is generated. A flood field image of the intrinsic uniformity of a detector can be acquired by positioning a point source sufficiently far away from the detector surface. To measure the extrinsic uniformity of a detector, a sheet phantom filled with activity can be placed over the face of the detector's collimator. After flood images are acquired, two measurements can be taken to quantify the uniformity of the detector: integral uniformity and differential uniformity.

To make these two measurements, first the flood image is smoothed using the mask shown in Equation 6. To calculate integral uniformity the maximum and minimum pixel values in the flood image are used in Equation 7. To calculate differential uniformity, for every five adjacent pixels in either a column or a row in the flood image, the highest and lowest pixel values are used in Equation 8.

$$M = \begin{bmatrix} 1 & 2 & 1 \\ 2 & 4 & 1 \\ 1 & 2 & 1 \end{bmatrix} \quad (6)$$

$$IU = \frac{(\text{max. pixel count}) - (\text{min. pixel count})}{(\text{max. pixel count}) + (\text{min. pixel count})} * 100 \quad (7)$$

$$DU = \frac{(\text{high} - \text{low})}{(\text{high} + \text{low})} * 100 \quad (8)$$

Integral uniformity gives a global value and is used to determine the maximum difference in detector pixel values for the entire detector. Differential uniformity is used to find the maximum difference in pixel values for a small region of the detector. Both of the parameters are useful to help characterize the uniformity performance of the detector.

### 1.3.1.5. ML-EM SPECT Image Reconstruction Method

The ML-EM algorithm [18, 34-36] is a statistical iterative image reconstruction algorithm used to reconstruct tomographic images from acquired projection images. The relationship between the imaging system response, 3D tomographic object being imaged, and the 2D projection image data are given in Equation 9 [18].

$$g = Hf \quad (9)$$

In this equation,  $f$  is a discretized description of the object being imaged, each value represents an element of the 3D tomographic object. Although the object is represented as a 3D matrix, here  $f$  is a column vector containing all of the values of the

3D matrix. Next,  $g$  is a discretized description of the 2D projection images acquired during the imaging process; like  $f$ ,  $g$  is also a column vector and each value in  $g$  represents one pixel in the set of acquired projection images. Finally,  $H$  is a system matrix that describes the imaging process and is used to map  $f$  to  $g$ . A system matrix includes the orientation of the imaging system during data acquisition, but can also include models of the imaging physics that affect the imaging process, such as photon attenuation or modeling of the collimator detector response.

In SPECT image reconstruction, the objective is to obtain an estimate of the distribution of the radiotracer  $f'$  using the acquired projection data  $g$  and the system matrix  $H$ . This can be expressed as the inverse problem to Equation 9, as shown in Equation 10.

$$f' = H^{-1}g \quad (10)$$

However, Equation 10 is not used to obtain the estimate  $f'$ . The system matrix  $H$  may not always be invertible, and even if it is, the size of the matrix  $H$  makes direct inversion impractical. Therefore, several iterative methods to obtain  $f'$  have been developed [18]. One such approach is the ML-EM reconstruction algorithm, which will now be briefly discussed.

The ML-EM algorithm is called a statistical iterative image reconstruction method because it is derived based on a statistical model of the noise fluctuations of the acquired projection images. When using this algorithm, it is assumed that the elements of the vector  $g$  are a set of independent Poisson random variables with mean  $Hf$ . The joint distribution of all elements of  $g$  can be expressed as shown in Equation 11. In this equation,  $h_{jk}$  are elements of the system matrix  $H$ .

$$Prob[\mathbf{g}|\mathbf{f}; \mathbf{H}] = \prod_j \exp \left[ - \sum_k h_{jk} f_k \right] \left( \sum_k h_{jk} f_k \right)^{g_j} (g_j!)^{-1} \quad (11)$$

Of course, in reality,  $\mathbf{f}$  is an unknown parameter. If we want to obtain an estimate for  $\mathbf{f}$ ,  $\mathbf{f}'$ , the likelihood function for this distribution is given as shown in Equation 12.

$$L(\mathbf{f}') = \prod_j \exp \left[ - \sum_k h_{jk} f'_k \right] \left( \sum_k h_{jk} f'_k \right)^{g_j} (g_j!)^{-1} \quad (12)$$

The ML-EM image reconstruction algorithm uses the Expectation Maximization (EM) [37] algorithm to find the  $\mathbf{f}'$  which maximizes Equation 12; the  $\mathbf{f}'$  that maximizes this equation is known as the Maximum Likelihood (ML) solution. A derivation of the ML-EM algorithm can be found in [18]. An update equation for the ML-EM image reconstruction method is shown in Equation 13.

$$f_j^{n+1} = \frac{f_j^n}{\sum_l h_{lj}} \sum_i h_{ij} \frac{g_i}{\sum_k h_{ik} f_{ik}^n} \quad (13)$$

The ML-EM algorithm can be broken down into the following steps. First, an initial estimate of the object space,  $\mathbf{f}'$ , is determined. In many cases, a uniform image is used as the initial estimate. Using system matrix  $\mathbf{H}$ , each voxel in the object space is projected into the projection image space. After this, each pixel in the projection of  $\mathbf{f}'$  is compared with its corresponding pixel in  $\mathbf{g}$  by taking the ratio of the acquired data to the estimate of the projection. The ratios are then backprojected into the object space using  $\mathbf{H}$ . Each voxel in  $\mathbf{f}'$  is updated by multiplying it with the backprojected ratio. The updated voxel is then normalized by the summation of the system matrix elements that were used in the backprojection of the comparison ratio. When all voxels in  $\mathbf{f}'$  are updated, an iteration of the ML-EM method is completed. The process can then be repeated with the

updated estimate. Every iteration of the ML-EM method brings the estimate of  $f$  closer to the ML solution. Fig. 1.3 shows how each portion of the ML-EM update equation corresponds to the process that was just discussed. It should be noted that the image reconstruction program is stopped prior to reaching the actual ML estimate. This is because the image showing the ML estimate will be dominated by image noise. Instead, reconstruction is simply stopped after a certain number of iterations, depending on the procedure used.

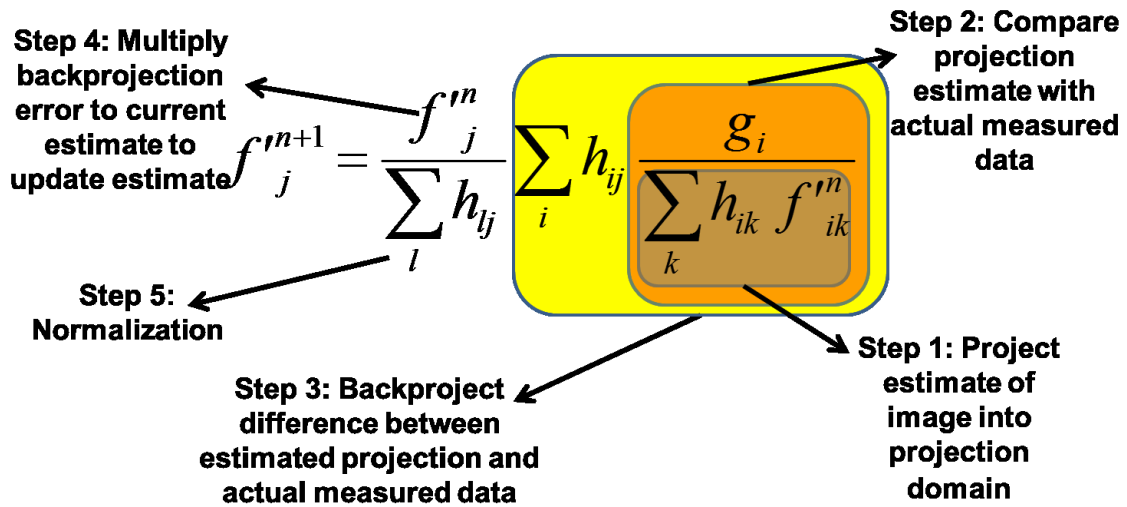


Fig. 1.3. Steps in ML-EM image reconstruction process

## 1.3.2. MR Imaging

### 1.3.2.1. Nuclear Magnetic Resonance

Magnetic Resonance Imaging (MRI) is an imaging modality that utilizes nuclear magnetic resonance (NMR) to produce an image. The following is a brief description of how NMR signals are generated, a more detailed description can be found in [17, 38]. To begin, any nucleus with an odd atomic number has a tiny magnetic field. Typically, a collection of a large number of these nuclei does not have a net magnetic field because the fields are not oriented in any particular direction and will cancel each other out.

However, this changes when the collection is placed within a strong static magnetic field; given time, many of the tiny magnetic fields will orient themselves in the same direction of the static field, producing a net magnetic moment in that direction.

If an additional magnetic field is generated, the orientation of the net magnetic moment of the collection can be manipulated. This is known as excitation. Magnetic fields used for excitation can be generated by surrounding the collection with a coil. When current is run through the coil, a second magnetic field that is perpendicular to the static magnetic field can be generated. During the generation of an NMR signal, current is pulsed through the coil at a specific frequency, the Larmor frequency. This frequency depends on the type of nuclei in the collection as well as the strength of the static magnetic field. When current is pulsed through the coil at the Larmor frequency, a time varying magnetic field will be generated. The excitation from the additional time varying magnetic field will cause the aligned magnetic moment of the collection to undergo a forced precession. As such, the net magnetic moment of the collection will no longer remain aligned with static magnetic field and will also begin to rotate about the static magnetic field at the Larmor frequency. If the excitation of the net magnetic moment continues, the orientation of the magnetic moment of the collection will be forced into a direction perpendicular to the static magnetic field. The rotation of the magnetic moment causes an RF signal to be emitted from the collection of nuclei. This signal can be received by an antenna and measured as a current.

After the excitation stops, the individual components of the magnetic moment will break apart from each other and the NMR signal will start to decay. Eventually, each component of the magnetic moment will return to equilibrium and become reoriented



with the static magnetic field. This is known as relaxation.

There are two key time measurements during the relaxation of the NMR signal that can be used to produce an MR image. The time that it takes for the magnetic moment to become completely reoriented with the static magnetic field is known as the T1 relaxation time. Furthermore, the time taken for the NMR signal to decay after the time varying magnetic field is no longer pulsed is known as the T2 relaxation time. The T1 relaxation time is usually longer than the T2 relaxation time. Different materials have different T1 and T2 relaxation times. These differences can be taken advantage of to produce an MR image of an object composed of different materials.

### **1.3.2.2. MR Imaging System Components**

The key hardware components in an MRI system are shown in Fig. 1.4. First, all MRI systems require a large annular magnet which is used to produce the constant magnetic field that will align the magnetic moment of the object to be imaged that is placed within it. Second, MRI systems require a set of gradient coils which current can run through. These coils are designed so that as current runs through them, an additional spatially variant magnetic field will be added to the constant magnetic field produced by the main magnet. There are three gradient coils, one for each dimension; they are used to determine the position of the acquired NMR signal within the object being imaged. As a simple example, when current runs through the z gradient, the magnetic field inside the MRI varies in the transaxial direction. Therefore, NMR can be induced in a single slice in the transaxial direction because each slice will have a different Larmor frequency. Traditional MR image acquisition, and the specific roles of all three gradient coils will be discussed in the next section. Another key hardware component of an MR system is the

RF coil, which is used to initiate the forced precession in the object being imaged. Some RF coils are designed to receive the NMR signal from the object as well. Finally, the pulse sequence programmer is used to control the gradient coils and initiate data acquisition.

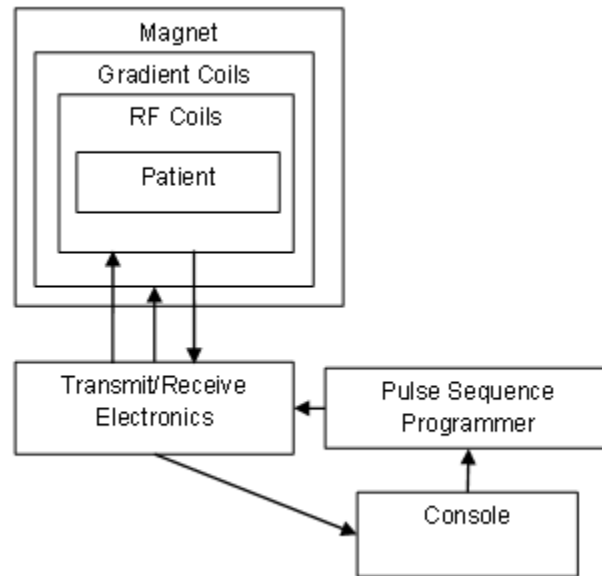


Fig. 1.4. Major Components of an MRI System

### 1.3.2.3. Traditional MR Image Acquisition

During the acquisition of an MR image, k-space data is obtained [17]. This data contains the spatial frequency information of the MR image that is being acquired. The procedure used to acquire all of the data required to produce an MR image is called a pulse sequence. There are many different pulse sequences and the type used to acquire data depends on the type of diagnostic information needed. However, the basic structure of a pulse sequence is as follows [17, 38]. First, current is run through the z gradient to determine the transaxial slice in the MR system where image data will be acquired. Then, the y gradient is applied at a specific amplitude that identifies which row of k-space data will be acquired. Finally, the x gradient is applied while acquiring data to acquire k-space

data from that particular row. This process is repeated while changing the amplitude of the y gradient to allow for data to be acquired in all of the k-space rows in the slice. Then, the inverse Fourier Transform on all of the acquired k-space data is taken in order to generate an image of the transaxial slice.

### **1.3.3. Previous Work on Simultaneous SPECT/MR Imaging**

#### **1.3.3.1. Previous Work Conducted by Other Research Groups**

There are currently only a few research groups actively working on the development of SPECT/MR systems. One group, led by Dr. Nalcioglu in UC Irvine has published on an MR compatible small animal SPECT system that they have been developing [39, 40]. However, their most recent papers show that the system is capable of producing images with resolution of  $\sim 1.9$  mm. State of the art small animal SPECT systems are capable of obtaining images with  $\sim 1$  mm or submillimeter resolution, which suggests that the system will be of limited use beyond a proof of concept showing that the system is capable of obtaining simultaneous SPECT/MR images. Another group, led by Dr. Meng at University of Illinois, has published on a system capable of obtaining high resolution SPECT/MR images of mouse brains [41, 42]. However, due to the system's geometry, it is unable to obtain full body images of mice, again limiting its use in preclinical research. Recently, other research groups have published on the development of preclinical SPECT/MR systems, but these systems are still in the simulation stage [43].

As of yet, there has not been any published work on completed clinical SPECT/MR system. However, research groups are currently investigating the potential of using SPECT/MR imaging for neurological and oncological research [44]. Additionally, multiple groups have proposed systems for clinical SPECT/MR imaging of the human

brain [45, 46]. These proposals discuss potential detector configuration and collimator design for clinical SPECT/MR systems, but as of now the work from these groups is still in the simulation stage.

### **1.3.3.2. Previous Work Conducted by Our Research Group**

Our group has previously developed a first generation prototype whole body preclinical SPECT/MR system [47-49]. The prototype system was designed to fit inside the 12 cm diameter bore of a 9.7 T Bruker small animal MRI system. Due to the design constraints, this system can only produce images with resolution of 2 to 3 mm, depending on the collimator used. Like the system developed by Dr. Nalcioglu's group, while this prototype shows that it is possible to develop a simultaneous SPECT/MR system, this system is also of limited use for preclinical research.

As discussed in Section 1.3.1.3, the imaging characteristics of semiconductor photon detectors are minimally affected in the presence of a magnetic field. For this reason, the prototype's detector was composed of semiconductor cadmium zinc telluride (CZT) modules. The system's detector consisted of three rings of CZT modules, with eight CZT modules per ring. Each square CZT module had a side length of 2.54 cm and had 16x16 pixels with a pixel side length 1.6 mm. For SPECT data acquisition, a multi-pinhole (MPH) collimator with 24 pinholes was built using a plastic shell made with a rapid prototyping method and was then filled with high density tungsten powder. The 24 pinholes were designed to project a 30 mm diameter common volume-of-view (CVOV) of the small animal to be imaged onto the corresponding 24 CZT detector modules. Finally, for MR data acquisition, an RF birdcage coil that surrounded the MPH collimator was used.

### **1.3.4. Improvements of Second Generation SPECT/MR System over Prototype System**

Development of the SPECT/MR system discussed in this thesis builds on what was learned during the development of the first generation prototype SPECT/MR system [50]. As discussed, the first generation prototype SPECT/MR system was composed of three rings containing eight CZT modules each. The inner diameter of the ring detector array was 61.3 mm. This small diameter limited the performance of the prototype system in many ways. First, the diameter of the detector caused the focal length of any MPH collimator designed for the system to be limited. This in turn, limited the magnification factor that could be achieved by the MPH collimator, which is one of the reasons that the original prototype system had poor resolution.

In comparison, the second generation SPECT/MR insert described in this work is composed of five rings each containing nineteen CZT modules. The CZT detector modules used in the second generation detector have the same dimensions, number of pixels, and pixel side length as the modules used in the prototype system. However, these detector modules were designed such that the pixel pitch of the detector was a seamless 1.6 mm throughout the entire detector, even between detector modules and detector panels. The increase in the number of CZT modules per ring led to an increased inner diameter of the detector of 153.2 mm, over twice the length of the prototype insert's diameter. This allowed us to design MPH collimators with higher magnification factors and better imaging resolution. The new detector was built for us by our collaborators at Gamma Medica-Ideas, now TriFoil Imaging.

The second generation SPECT/MR insert also features improved collimator

design. While the prototype's MPH collimators featured pinhole apertures manufactured using a rapid prototyping process, the collimators of the second generation system utilizes pinholes machined out of solid tungsten. Using machined pinholes allowed us to use pinholes with much smaller diameters, which allowed for improved image resolution. More details about the design and implementation of the collimators for the second generation system will be discussed in chapters two and three.

Finally, in the first-generation SPECT/MR prototype system, the RF coil was designed to be placed outside of the collimator because of the limited size of the detector. However, the second-generation system's larger detector diameter enabled us to design collimators where the RF coil could be placed within the MPH collimator. This change in design improves the performance of the MR system by increasing the SNR of acquired data. To acquire MR images with the second-generation SPECT/MR system, a custom transmit/receive RF coil was designed by our collaborative partners in the Division of MR Research with the Department of Radiology. A birdcage coil for each of the collimators designed was constructed. During imaging experiments, the RF coil was inserted into the collimator. To protect the coil from receiving interference from the electronics in the SPECT detector, it was surrounded by a copper shield. The shield was designed such that, less than ~5% of the gamma ray photons emitted from the object being imaged will be attenuated, to limit the influence that the MR coil would have on SPECT data acquisition.

## **Chapter 2: Methods**

### **2.1. Design, Evaluation, and Implementation of Multi-pinhole (MPH) Collimators for the SPECT/MR System**

The following section will discuss the methods used to design, evaluate, and ultimately implement two MR compatible multi-pinhole (MPH) collimators for the SPECT/MR system. As will be shown there were several collimator parameters to consider. To aid in the design of the MPH collimators, we developed methods that allowed us to systematically compare different collimator designs as design parameters were varied. These methods were used to design two MPH collimators for different imaging purposes. Both MPH collimator designs were evaluated using analytical and Monte Carlo simulation methods to ensure they could be used to obtain artifact free SPECT images. After the collimator designs had been evaluated, MR compatible prototypes of each collimator were built.

As described in Section 1.3.4, the SPECT/MR system uses a 19 sided ring detector with a seamless 1.6 mm pixel pitch throughout the entire detector. To best take advantage of the SPECT/MR system detector's ring type geometry, we chose to use cylindrical MPH collimators fitted with multiple rings of equally spaced pinholes focusing on a spherical common-volume-of-view (CVOV). Fig. 2.1 shows a 3D model of a sample cylindrical MPH collimator, the collimator's CVOV, and the SPECT/MR ring detector. As shown by Fig. 2.1, a cylindrical collimator design is well suited for use with our ring detector. This is because cylindrical collimators can be designed such that projections from the collimator cover the entire detector, maximizing use of the detector's surface area. Furthermore, additional projections views can easily be obtained

by rotating the collimator about the cylinder's axis of rotation, if they are needed for artifact free reconstruction of SPECT images. An additional advantage to the cylindrical MPH collimator design is that the geometric efficiency at the center of the CVOV will be higher than if a single pinhole collimator was used instead. This is because all pinholes in the cylindrical MPH collimator are focused on the center of the CVOV.

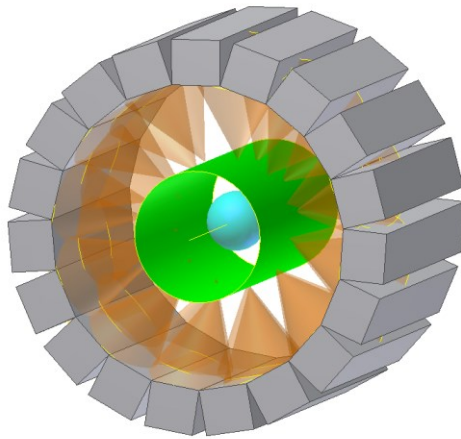


Fig. 2.1. Sample cylindrical MPH collimator design for the SPECT/MR system. In this figure, the gray blocks represent detector modules, the yellow cones represent pinhole projections, the green cylinder is the MPH collimator, and the blue sphere is the MPH collimator's CVOV.

### **2.1.1. Methods to Determine Final Multi-pinhole (MPH) Collimator Design Parameters**

In this section, we will identify each of the MPH collimator design parameters considered and discuss how varying these parameters impact the collimator's performance in terms of imaging resolution and geometric efficiency. Constraints impacting the design of the MPH collimator will also be discussed. Finally, methods developed that allow us to systematically evaluate possible collimator designs as design parameters are varied will be introduced.



### 2.1.1.1. Multi-pinhole (MPH) Collimator Design Parameters

While designing the MPH collimators for use with the SPECT/MR system, there were many collimator parameters to consider: CVOV diameter, pinhole cone angle, collimator sleeve radius, pinhole diameter, pinhole tilt angle, total number of projections acquired, degree of projection multiplexing, system resolution, and collimator geometric efficiency. The parameters that determine the geometry or position of a pinhole in the collimator can be seen in Fig. 2.2. Each of these parameters will now be briefly explained.

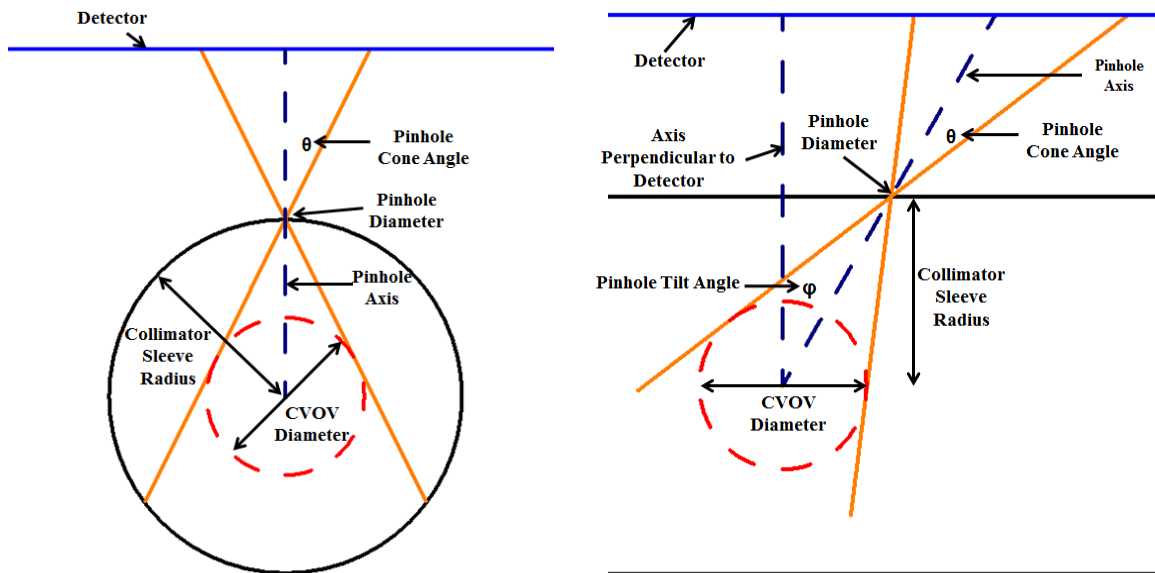


Fig. 2.2. Pinhole collimator design parameters (left)- transaxial view of pinhole collimator, and (right)- sagittal view of a cylindrical pinhole collimator.

CVOV diameter refers to the diameter of the spherical volume of space that all pinholes in the MPH collimator are focused on. Any object placed inside this spherical volume will be seen by all of the pinholes in the collimator, allowing for the acquisition of MPH projection images. If the diameter of the CVOV is too small, it will result in truncation of the object being imaged. Pinhole cone angle determines the CVOV

diameter that can be imaged. Collimator sleeve radius refers to the distance from the center of the spherical CVOV to the center of the pinhole, while pinhole diameter refers to the size of the aperture of the pinhole collimator that allows photons to reach the detector. To utilize the entire detector surface area, some of the pinholes focused on the CVOV must be tilted; as shown in Fig. 2.2, pinhole tilt angle is the angle between the pinhole's axis and an axis that is perpendicular to the detector's surface that passes through the center of the CVOV. It should be noted that tilting pinholes can lead to a reduction in geometric efficiency. For the same resolution as a nontilted pinhole, at the same collimator sleeve radius, a tilted pinhole's geometric efficiency is reduced by  $\cos(\varphi)^2$ , where  $\varphi$  is the tilt angle of the pinhole. Total number of projections acquired is equivalent to the total number of pinholes used in the collimator; for each pinhole in the collimator, we will obtain a projection of the object on the detector. However, because the amount of detector surface area is fixed, for a fixed collimator sleeve radius, as the number of projections obtained is increased, the amount of projection multiplexing is increased as well. Projection multiplexing occurs when projection images from two or more pinholes overlap each other on the detector surface. As an example, Fig. 2.3 shows the projection of the CVOV when using a nine pinhole collimator that allows for projection multiplexing. The arrow points to a region where two projections are overlapping, resulting in projection multiplexing. It has been shown that as the amount of multiplexing increases, the amount of artifacts in the reconstructed SPECT image acquired will also increase [51, 52]. Therefore, the degree of projection multiplexing allowed limits the total number of pinholes that can be placed on the collimator for a given sleeve radius.

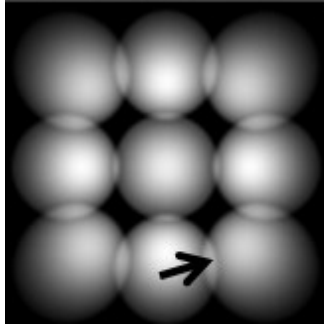


Fig. 2.3. Nine pinhole collimator with multiplexed projections. The black arrow points to an example of projection multiplexing.

System resolution refers to the smallest distance between two details that can be separated in the reconstructed SPECT image. This parameter includes the effect of the collimator as well as the system detector's intrinsic resolution. Geometric efficiency refers to the percent of photons that pass through the collimator when compared with the total number of photons emitted from the object being imaged. For an MPH collimator, the geometric efficiency can be calculated by summing the geometric efficiency of each pinhole. Both system resolution and geometric efficiency can be calculated using the equations for pinhole collimator imaging shown in Section 1.3.1.2.

Ideally, a cylindrical MPH collimator would have the highest possible imaging resolution, the highest possible geometric efficiency, and would acquire the largest possible number of projection images simultaneously under the given system configuration. A collimator with these characteristics could be used to obtain high resolution SPECT images reconstructed from projection images with a high number of photon counts without having to acquire data for an extended length of time. Furthermore, if the collimator was able to acquire many projection images

simultaneously, SPECT images free of reconstruction artifacts could be obtained while leaving the collimator stationary.

Unfortunately, these three characteristics conflict with each other. As shown in Section 1.3.1.2, collimators designed to have high imaging resolution will have low geometric efficiency, while collimators with high geometric efficiency will have poor resolution. Furthermore, for reasons that will be discussed further in Section 2.1.1.3, for a fixed target system resolution, in many cases geometric efficiency decreases as the number of total projection views increases. Briefly, when adding pinholes to a collimator, to ensure that the amount of projection multiplexing between neighboring pinholes remains the same, the magnification of each pinhole must be decreased. As magnification decreases, the pinhole is taken farther from the center of the CVOV. To maintain a fixed target resolution, the pinhole's diameter must be decreased. Both of these changes reduce the geometric efficiency of each pinhole in the collimator. Therefore, even though the total number of pinholes in the collimator increases, the net geometric efficiency of the collimator is reduced.

Fig. 2.4 shows two possible cylindrical MPH collimator designs for the SPECT/MR system, and Table 2.1 shows each of the collimator's key design parameters. Both images show how the CVOV projects onto the surface of the SPECT/MR system's ring detector through each pinhole in the collimator. Each image shown has matrix size 80x16x19 with pixel size of 1.6 mm. Furthermore, each 80x16 image shows what is seen on one panel of the ring detector. To ease visualization, in the images below the ring detector area has been 'rolled out' and displayed as a single flat detector surface. If the ring detector was a true cylinder, the horizontal and vertical lengths of these images

would correspond respectively to the cylinder’s circumference and height. All ring detector projection images shown in this thesis are displayed in the same format.

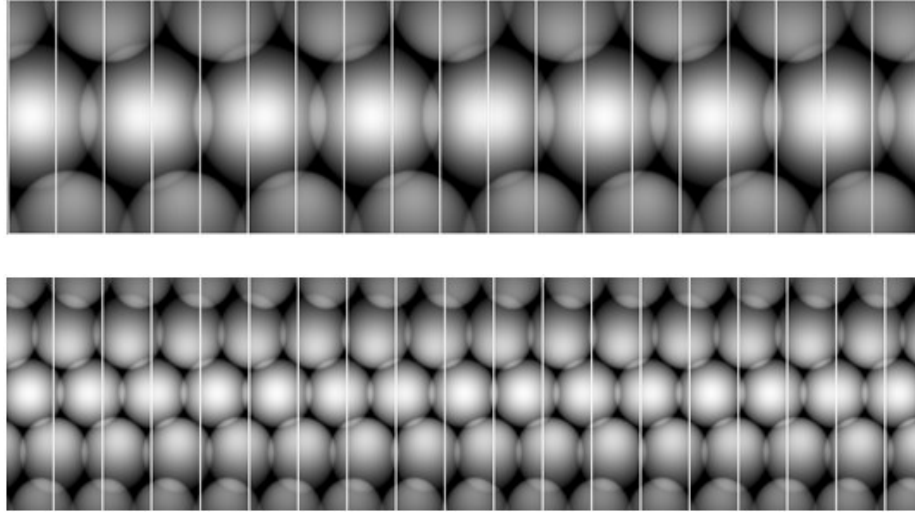


Fig. 2.4. Two MPH collimator designs with same target system resolution

# of Pinholes	24	75
Collimator Sleeve Radius	24.6 mm	35.9 mm
Pinhole Magnification	2.11	1.14
Pinhole Diameter	0.88 mm	0.28 mm
Pinhole Tilt Angles	$0^\circ, \pm 39.7^\circ$	$0^\circ, \pm 21.2^\circ, \pm 39.7^\circ$
System Resolution	1.5 mm	1.5 mm
Geometric Efficiency	1.39E-03	2.16E-04

The collimators shown in Fig. 2.4 were designed with matching target system resolution, CVOV diameter, and degree of projection multiplexing. However, it is immediately clear that there are substantial differences between the two collimator designs. The first collimator has three rings of pinholes with eight pinholes per ring with significant magnification of each pinhole’s projection. The second collimator design has five rings of pinholes with 15 pinholes per ring with projections that are only slightly magnified. To fit 75 projections on the detector surface while maintaining the same degree of projection multiplexing as the collimator design with 24 pinholes, a larger

collimator diameter was needed, as is shown in Table 2.1. As the collimator diameter increased, the focal length of the pinholes decreased, which reduced the amount of magnification of the CVOV. Furthermore, because the pinholes in the first collimator are closer to the center of the CVOV, the pinholes can have a larger aperture while maintaining the same system resolution of the second pinhole collimator. Using the equation for pinhole geometric efficiency shown in Section 1.3.1.2 with the collimator parameters shown in Table 2.1, and taking pinhole tilt angle into account, it can be shown that despite having fewer pinholes, the 24 pinhole collimator has a higher geometric efficiency at the center of the collimator's CVOV than the 75 pinhole collimator does.

Both of the collimators shown in Fig. 2.4 have their own advantages. While the 24 pinhole collimator design shown has a higher geometric efficiency than the 75 pinhole collimator, the 75 pinhole collimator will provide more than three times as many pinhole projections during acquisition of experimental data. To achieve artifact free image reconstruction, the 24 pinhole collimator will have to be rotated to obtain additional projections for the SPECT reconstruction, but this is not necessarily the case for the 75 pinhole collimator. If we were to pick between the two collimators, we would have to consider what sort of experiments the collimator would be used for. For example, if we wanted to conduct dynamic SPECT studies, the 75 pinhole collimator would be the better choice, because projection data could be acquired while leaving the collimator stationary. From this example, it is clear that design of a MPH collimator is not a trivial matter due to the number of parameters to consider.

### 2.1.1.2. Multi-pinhole (MPH) Collimator Design Constraints

When designing the MPH collimators for the SPECT/MR system, it was important to identify outside constraints that could impact design of the collimators. Ultimately, we determined that there were two significant constraints on the collimator design: the space allocated for the MR RF coil that was to be held within the MPH collimator, and the ring detector's intrinsic resolution. The position and size of the MR RF coil inside the collimator was a constraint specific to the development of a SPECT/MR system, while detector intrinsic resolution is a constraint that affects the design of every pinhole collimator. Fig. 2.5, shows how the space inside the detector was utilized. The space allocated for the MR RF coil meant that the minimum collimator diameter was 45 mm. This meant that there was a maximum amount of magnification that the pinhole collimator could achieve, in turn, limiting the highest possible that could be obtained by the system.

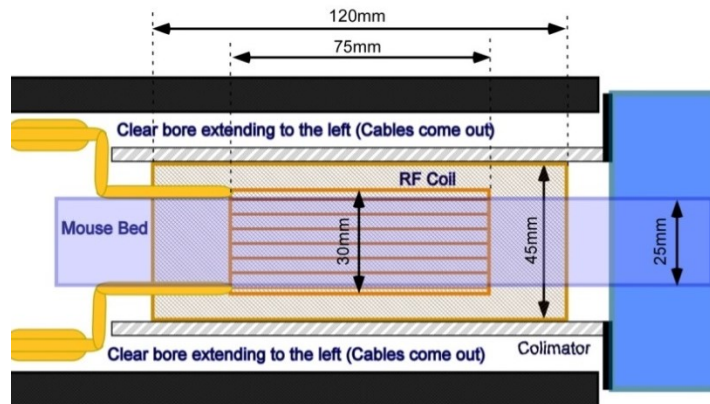


Fig. 2.5. Space Utilization of the SPECT/MR system

The other significant constraint on the collimator design was the detector's intrinsic resolution. As discussed in Section 1.3.1.2, a SPECT system's image resolution is determined by the resolution of its collimator as well as the detector's intrinsic

resolution. The effect of intrinsic resolution on the design of a single pinhole collimator can be seen in Fig 2.6. This graph shows how geometric efficiency at the center of a single pinhole collimator's CVOV varies as collimator sleeve radii increases. At all collimator sleeve radii, the collimator is designed to have target system resolution of 1 mm and to have a CVOV diameter of 30 mm. Furthermore, the distance from the center of the CVOV to the detector surface is 76.7 mm, the same distance in the design of the SPECT/MR system detector. The figure shows that as collimator sleeve radius increases, the pinhole geometric efficiency decreases. This is because as collimator sleeve radius increases, the pinhole collimator's diameter must be made smaller to maintain the target system resolution of 1 mm. Both of these changes result in a reduction of the collimator's geometric efficiency.

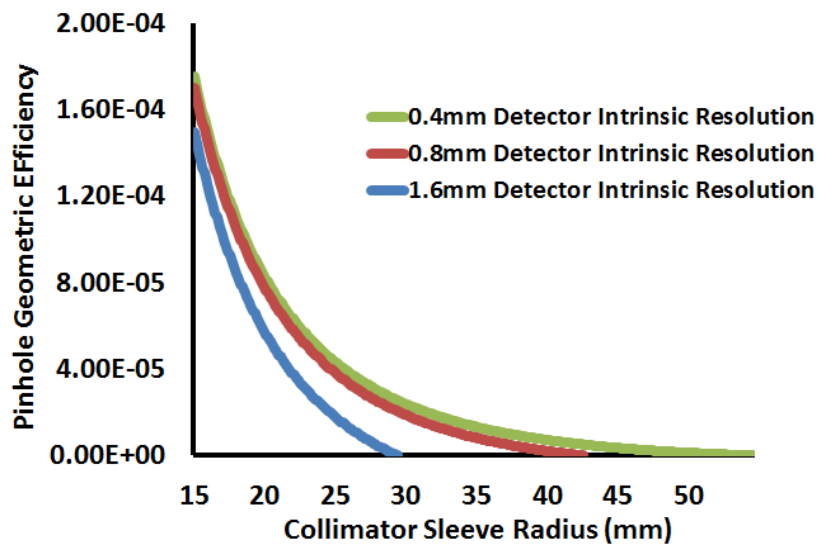


Fig. 2.6. Effect of Detector Intrinsic Resolution on Pinhole Collimator Geometric Efficiency for Fixed Target System Resolution of 1 mm at Different Collimator Sleeve Radii

However, system resolution depends on both the pinhole collimator's resolution and the detector's intrinsic resolution. As intrinsic resolution is improved, a pinhole



collimator with same collimator sleeve radius can be designed with a larger pinhole aperture to obtain the same overall system resolution. This increase in pinhole aperture diameter directly results in an increase in the collimator's geometric efficiency. Furthermore, as intrinsic resolution improves, the pinhole collimator can be held further from the CVOV's center and still maintain the target system resolution. Fig. 32.6 shows that when a detector with 1.6 mm intrinsic resolution is used, the pinhole can be at most 29.5 mm from the CVOV's center in order to maintain 1 mm system resolution. In comparison, with a detector with 0.4 mm intrinsic resolution, the pinhole can be as far as 54.7 mm from the center of the CVOV.

When using a ring detector of fixed diameter, increasing the collimator sleeve radius reduces the pinhole's focal length, which means that the pinhole magnification will decrease. This means that, as collimator sleeve radius increases, more pinhole projection images can be fit onto the surface area of the detector. Therefore, intrinsic resolution of the detector also determines the total number of views that can be simultaneously obtained by a MPH collimator.

### **2.1.1.3. Systematic Methods to Evaluate Multi-pinhole (MPH) Collimator Designs**

As discussed in Section 2.1.1.1, there are many parameters that must be considered when designing MPH collimators. Changing a single parameter while leaving the rest the same can significantly impact the collimator's performance. For example, if a collimator's sleeve radius is increased while leaving all other parameters the same, the collimator's resolution, and geometric efficiency will decrease. To design the collimators for our SPECT/MR system, we needed to develop methods to systematically evaluate

how collimator performance changed as design parameters were varied. These methods allowed us to compare different collimator designs and ultimately were used to determine our final collimator design parameters. Specifically, the systematic methods to evaluate collimator design allow us to identify, for a target system resolution, the MPH collimator design with the highest geometric efficiency at the center of the collimator's CVOV. It should be noted that ultimately, the MPH collimator with the highest geometric efficiency found using our systematic methods may not always be a usable design due to other constraints, such as the placement of the MR RF coil, as described in Section 2.1.1.2. Nevertheless, they provide a guide for the highest possible geometric efficiency for a target system resolution that can be obtained with an MPH collimator for the SPECT/MR system. This knowledge allows us to compare other potential designs and to learn how far away they are from the optimal design, in terms of geometric efficiency.

Over the course of this project, we developed two different systematic methods to evaluate different MPH collimator designs. Other systematic methods developed to evaluate different collimator designs can be found in [53, 54]. The two evaluation methods we developed were named the area based method and the model based method. The area based method was developed first and was used to determine the final collimator designs for the SPECT/MR system. The model based method builds upon the area based method and allows for more realistic evaluation of different collimator designs. However, the model based method was not developed until after the MPH collimator designs for our SPECT/MR system had been finalized.

The area based method was used to design two collimators for different imaging purposes. The first collimator was designed for high resolution preclinical imaging while

having the highest possible collimator geometric efficiency. We were not concerned with the total number of simultaneous views obtained by the high resolution (HR) MPH collimator and allowed for rotation of the collimator to obtain additional views for artifact free SPECT image reconstruction, if necessary. The second collimator was designed for both general purpose imaging and fast dynamic SPECT studies. This meant that the collimator needed to obtain a sufficient number of views simultaneously to allow for artifact free SPECT image reconstruction without additional collimator rotation.

To simplify development of the design methods, we initially fixed three collimator parameters: CVOV diameter, system resolution, and degree of projection multiplexing. First, we decided that a 30 mm diameter CVOV would be sufficient to fit most mice used in imaging experiments. Second, we decided that the system would achieve 1 mm resolution at the center of the CVOV when imaging with the HR MPH collimator, and 1.5 mm resolution at the center of the CVOV when imaging with the general purpose (GP) MPH collimator. Third, we decided that we would allow no more than 20% multiplexing of a single pinhole projection by adjacent projections in order to minimize artifacts in the reconstructed image. This percentage of multiplexing was chosen due to results shown in [51, 52].

The remaining collimator design parameters, pinhole diameter, cone angle, collimator geometric efficiency, tilt angle, and number of projection views can be expressed as functions of collimator sleeve radius. As discussed in Section 1.3.1.2, pinhole geometric efficiency depends on the distance from the object to the center of the pinhole, in this case, this distance is equivalent to collimator sleeve radius. After fixing system resolution, due to the detector's ring type geometry, pinhole diameter can be

expressed as a function of collimator sleeve radius using the equation for system resolution with a pinhole collimator that was shown in Section 1.3.1.2, as shown below in Equation 14. In Equation 14,  $R_s$  is the target system resolution and  $R_i$  is the detector's intrinsic resolution. Furthermore, as shown in Fig. 2.7,  $Z$  is collimator sleeve radius, and  $K$  is the ring detector's radius. The size of the actual pinhole diameter is determined by the material the pinhole is made out of as well as the pinhole's cone angle. Given a fixed CVOV, simple geometry can be used to express pinhole cone angle as a function of collimator sleeve radius, and is shown below in Equation 15. In this equation,  $Z$  is collimator sleeve radius and  $R$  is the radius of the CVOV.

$$D_e(Z) = \sqrt{\left(R_s^2 - \left(\frac{Z * R_i}{K - Z}\right)^2\right) * \left(\frac{K - Z}{K}\right)^2} \quad (14)$$

$$\theta(Z) = 2 * \sin^{-1}\left(\frac{R}{Z}\right) \quad (15)$$

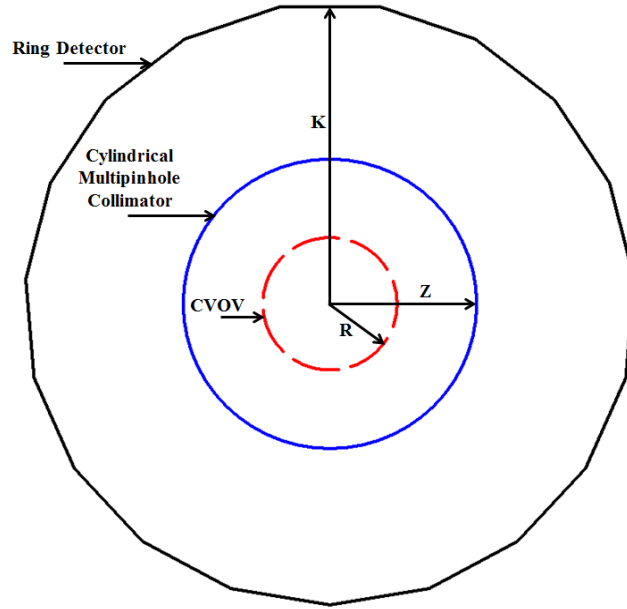


Fig. 2.7. System geometry used in development of area based and model based methods

It is important to note that when system resolution ( $R_s$ ) is fixed, as collimator sleeve radius ( $Z$ ) increases, pinhole diameter ( $D_p$ ) will decrease. This occurs so that the chosen system resolution will be maintained as the collimator sleeve radius increases. As a result, when collimator sleeve radius increases, a pinhole's geometric efficiency at the center of the detector's CVOV will decrease. This is because the pinhole is both farther from the CVOV and has a smaller diameter. When collimator sleeve radius increases, the pinhole is placed closer to the detector's surface. This reduces the pinhole's focal length, and results in a decrease of pinhole magnification. As magnification decreases, the surface area of the detector covered by a pinhole projection will decrease as well. In turn, to maximize detector surface area usage, we can increase the total number of pinholes used. Thus, for a fixed degree of projection multiplexing, as collimator sleeve radius increases, the number of projection views in the collimator will increase as well.

As will be shown, the most significant difference between the area based method and the model based method is how the two methods estimate the total number of pinholes that can be used for a given collimator sleeve radius.

#### **2.1.1.4. Area Based Method for Multi-pinhole (MPH) Collimator Design**

The area based method uses the following steps to determine MPH collimator design parameters. To begin, a CVOV diameter and system resolution at the CVOV's center are chosen. Then, for a given collimator sleeve radius, the surface area of the projection of the CVOV from a single pinhole onto a flat detector, both held directly over the CVOV is calculated. To estimate the total number of pinholes that can be used for the given collimator sleeve radius, the total surface area of the detector is divided by the surface area used by the projection of the CVOV from the single pinhole. The total surface area of the ring detector is given by the system design. As described, each side of the ring detector consists of five CZT detector modules, each with side length of 2.54 cm. Therefore, the area of each side of the detector is  $\sim 32.25 \text{ cm}^2$ , and the total surface area of the detector is  $612.75 \text{ cm}^2$ .

The ratio between the total surface area of the detector and the surface area used by the projection of the CVOV is used as an estimate of the number of pinholes that can be used with the given collimator sleeve radius. Then, the effective pinhole diameter required to achieve the target system resolution is calculated using Equation 14, shown earlier. After the effective pinhole diameter has been calculated, the geometric efficiency at the center of the CVOV from a single pinhole is calculated using the effective pinhole diameter and the collimator sleeve radius. The estimate of the total number of pinholes and the geometric efficiency calculation are then used to estimate the geometric

efficiency of a MPH collimator with the given sleeve radius by multiplying the calculated geometric efficiency by the estimated number of total pinholes that can be utilized. This process is then repeated with larger collimator sleeve radii until a radius is reached when the calculated pinhole aperture required to achieve the target system resolution is 0 mm. Plots of collimator sleeve radius and geometric efficiency for both the HR MPH collimator and the GP MPH collimator obtained using the area based method are shown in Fig. 2.8.

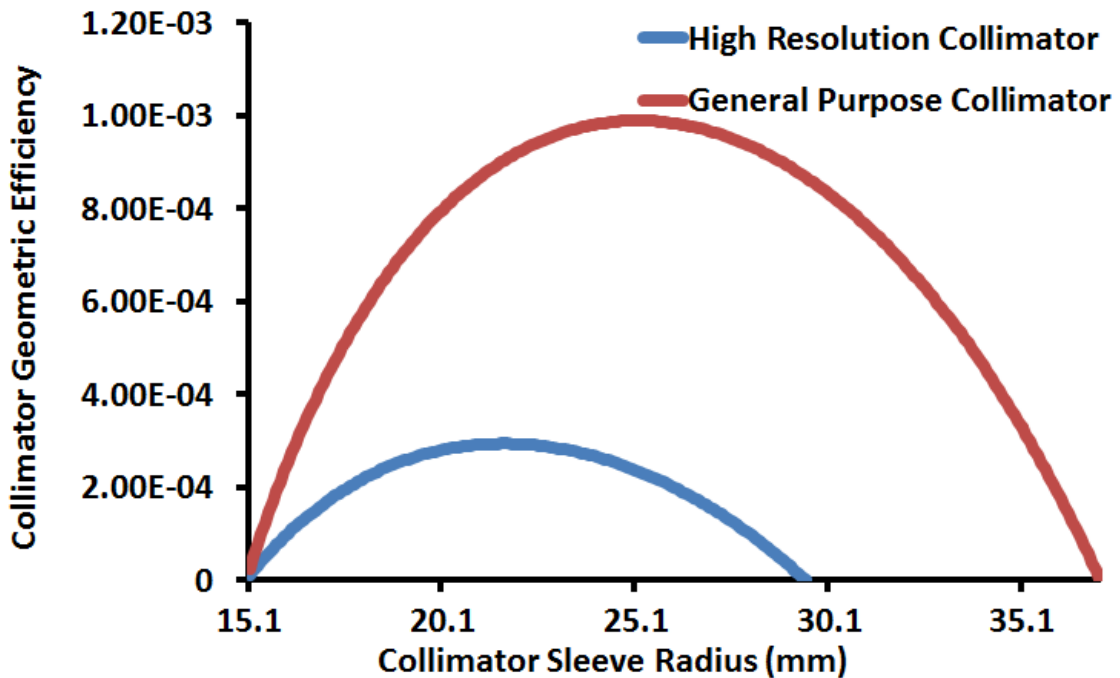


Fig. 2.8. Collimator Design Results using the Area Based Method for High Resolution and GP MPH collimators

There are several noteworthy features of these plots. First, for any given collimator sleeve radius, the geometric efficiency of the GP MPH collimator is always higher than the HR MPH collimator. At each collimator sleeve radius, all collimator design parameters for the two collimators match except for pinhole diameter. Furthermore, for all collimator sleeve radii in the range plotted in Fig. 2.8, the pinhole

diameter required to obtain 1 mm system resolution is always smaller than the pinhole diameter required to obtain 1.5 mm system resolution. This explains why the GP MPH collimator has a higher geometric efficiency than the HR MPH collimator, regardless of collimator sleeve radii. Secondly, the GP MPH collimator can have a larger collimator sleeve radius than the HR MPH collimator. The detector's intrinsic resolution limits the largest possible sleeve radius for a target system resolution. As target system resolution improves, the possible range of collimator sleeve radii decreases. Finally, both curves have a single point that has the highest estimated geometric efficiency. This makes it very easy to identify the optimal collimator sleeve radius using the area based method. Most importantly, it shows us that certain pinhole collimator designs have better performance than others. For example, for the HR MPH collimator design, any collimator design with sleeve radius greater than 27 mm will have a geometric efficiency that is less than 50% of the optimal collimator's geometric efficiency.

#### **2.1.1.5. Limitations of the Area Based Method**

However, there are some limitations when using the area based method. Most importantly, it does not provide any information about the collimator's pinhole configuration. As an example, the area based method estimated that the optimal collimator sleeve radius for the HR MPH collimator could fit approximately twelve pinholes. It is not immediately clear, however, whether the pinhole configuration of the HR MPH collimator should be one ring of twelve pinholes, two rings of six pinholes each, or three rings each with four pinholes. Furthermore, the area based method does not provide a discrete estimate of the number of pinholes to be used in the collimator. Mechanical drawings are needed to determine the exact number of pinholes to be used as



well as which pinhole configuration maximizes usage of the detector surface.

Additionally, the geometric efficiency calculated is only an approximation. For every pinhole on the collimator to cover the same CVOV and to utilize the entire detector surface area, some of the pinholes on the collimator must be tilted, as shown earlier in Fig. 2.2. For the same resolution as a nontilted pinhole, a tilted pinhole's geometric efficiency is reduced by  $\cos(\theta)^2$ , where theta is the tilt angle of the pinhole. The area based method does not account for this loss of geometric efficiency.

Finally, the projection of the CVOV onto the surface of the detector is not necessarily a perfect circle, as is assumed with the area based method. This is because the SPECT/MR system detector is a ring, instead of a single flat surface. The estimate of the number of pinholes to be used in the collimator can be improved if the effect of the detector's curvature on the projection is considered. The first image in Fig. 2.9 shows the projection of the CVOV from a single pinhole onto a flat surface, while the second image in Fig. 2.9 shows the projection of the CVOV from the same pinhole projected onto the ring detector used for the SPECT/MR system. In the second case, the pinhole projection covers three different detector panels. For ease of visualization, the three detector panels are shown as if they had placed directly adjacent to each other, and the detector curvature is not shown. However, the effect of the detector curvature onto the projection of the CVOV has been included as well. As a result of the detector curvature, the projection onto the detector is an ellipse instead of a circle. The two projections have radii of the same length in the axial direction of the detector. However, as demonstrated in Fig. 2.9, the transaxial radius of the projection onto the ring detector is shorter than the transaxial radius of the projection onto the flat detector.

With these facts in mind, a second method to evaluate collimator designs was developed: the model based method. By taking into account the detector geometry and making assumptions about the pinhole configuration in advance, more realistic estimates about the number of pinholes to be used can be made. In turn, this leads to improved estimates of the collimator's geometric efficiency for a given sleeve radius. Furthermore, with the model based method a pinhole configuration with a discrete number of pinholes is automatically determined; there is no need for additional mechanical drawings as is the case with the area based method. Finally, the model based method takes pinhole tilt angles into account, resulting in a better estimate of collimator geometric efficiency. The model based method will now be discussed.

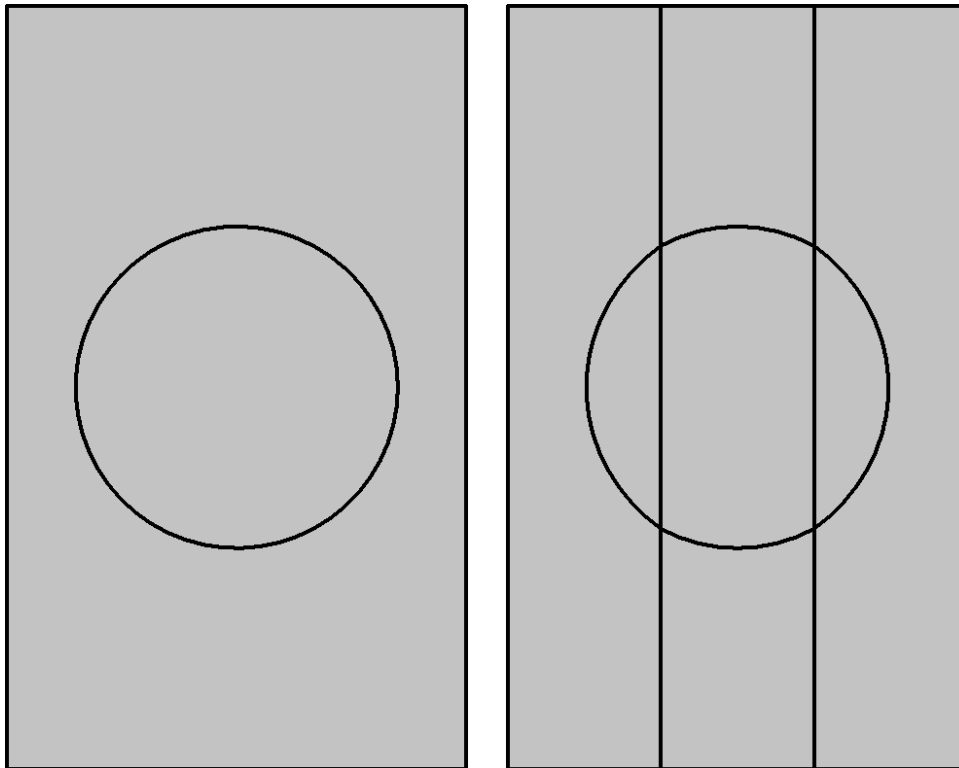


Fig. 2.9. Pinhole projection boundaries onto a flat surface (left) and a curved surface (right)

### **2.1.1.6. Model Based Method for Multi-pinhole (MPH) Collimator Design**

All MPH collimators designed with the model based method have the same basic pinhole configuration. This pinhole configuration will now be described. The collimators designed using the model-based method have a central ring of nontilted pinholes focused directly on the CVOV. If the collimator sleeve radius is sufficiently far from the CVOV to allow for additional rings of pinholes, additional rings of tilted pinholes are included on either side of the central ring. Therefore, all collimators designed with the model-based method have an odd number of pinhole rings. Secondly, the pinholes for each ring are spaced equally apart from other pinholes in the same ring. Furthermore, the side rings of pinholes are rotated by  $R \cdot N / M$  degrees with respect to the central ring where  $N$  is the angle between each pinhole in a single ring,  $M$  is the total number of rings, and  $R$  is an integer ranging from  $-(M-1)/2$  to  $(M-1)/2$ , excluding zero. This rotation ensures that each ring of pinhole covers a different set of angles. For example, for a 24 pinhole configuration three rings with eight pinholes each, the central ring would cover angles  $0^\circ$ ,  $45^\circ$ ,  $90^\circ$ ,  $135^\circ$ , ...,  $270^\circ$ , and  $315^\circ$ , one side ring would cover angles  $15^\circ$ ,  $60^\circ$ ,  $105^\circ$ , ...,  $285^\circ$ , and  $330^\circ$ , while the other side ring would cover angles  $30^\circ$ ,  $75^\circ$ ,  $120^\circ$ , ...,  $300^\circ$ , and  $345^\circ$ .

The following will describe how the model based method estimates the number of pinholes that can be used for a given collimator sleeve radius. To begin, as with the area based method, a CVOV diameter, target system resolution at the CVOV's center, and amount of multiplexing allowed are chosen. Then, for a given collimator sleeve radius, the dimensions of the boundary of the CVOV's projection from a single pinhole onto the detector surface are calculated. To be as accurate as possible, it is necessary to take the

curvature of the detector into account. The radius of the projection onto the ring detector in the axial direction of the ring detector has the same length as the radius of the projection onto a flat surface and can be easily calculated using similar triangles using the known cone angle of the pinhole collimator. However, it is not as straightforward to calculate the radius of the projection in the transaxial direction, and the following method is used. First, the curvature of the detector is approximated as a circle with the same radius of the ring detector. Then, for a given collimator sleeve radius, the cone angle of the single pinhole is extended to the edge of the circular detector as shown in Fig. 2.10. After this, the length of the red chord in Fig. 2.10 is calculated. The length of this chord is used as the length of the diameter of the pinhole projection in the transaxial direction.

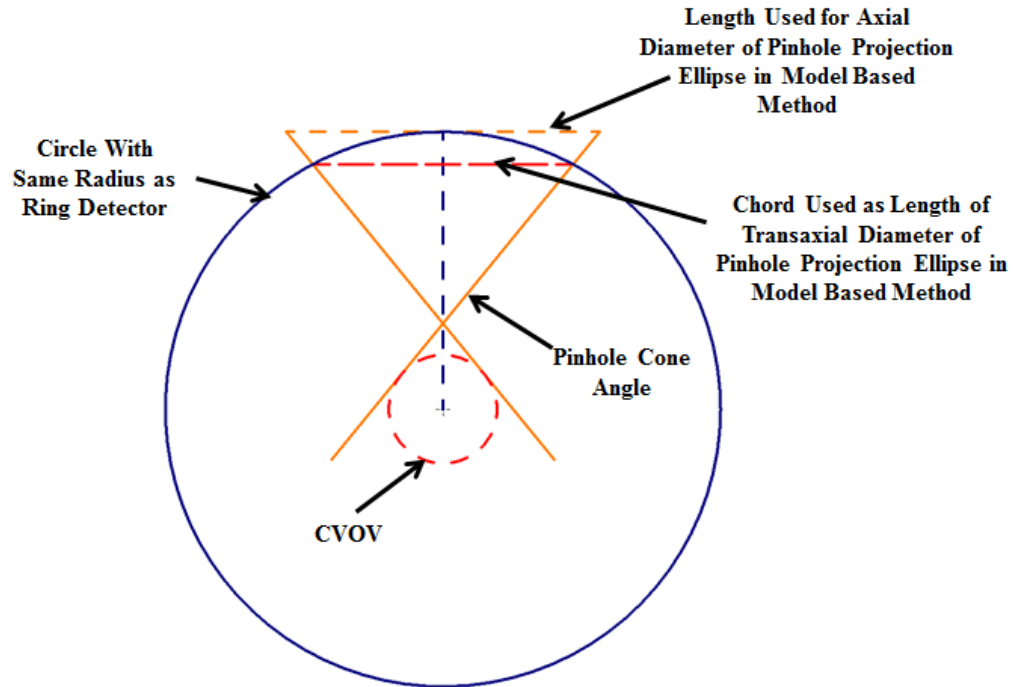


Fig. 2.10. Geometry Used to Estimate Effect of Detector Curvature on Pinhole Projection Image. When using a ring type detector, pinhole projection images will be elliptical rather than circular. The length of the projection's diameter in the transaxial direction of the detector can be estimated using the red dashed line in the figure above, while the length of the projection in the axial direction can be estimated using the orange dashed line.

After the length of the radii of the elliptical pinhole projection in both the axial and transaxial directions are known, the amount of detector area covered by a single projection of the CVOV can be calculated, as shown in Step 1 in Fig. 2.11. Next, given the total degree of multiplexing allowed, we can calculate the total number of pinholes that can be placed in a single ring surrounding the object at the center of the collimator when the pinholes are equally spaced from each other, as shown Step 2 in Fig. 2.11. This calculation is made using the detector's circumference and the pinhole projection's diameter in the transaxial direction. After this, the total number of rings of pinholes that can be placed on the collimator such that at least half of the CVOV will still project up to

the surface of the detector through each pinhole in the additional rings, while still maintaining the allowed degree of projection multiplexing, as seen in Step 3 in Fig. 2.11. During this step, the tilt angles of the pinholes in the side rings are determined such that all pinholes focus on the same CVOV.

Then, the effective pinhole diameter needed to achieve the target system resolution given the collimator sleeve radius is calculated. The geometric efficiency at the center of the CVOV for the entire MPH configuration can then be calculated using the estimate of the total number of pinholes, the pinhole effective diameter, and the tilt angle of pinholes in the side rings. The length of the collimator sleeve radius is increased and this process is repeated until a radius is reached when the calculated pinhole aperture required to achieve the target system resolution is 0 mm. It is at this point that the systematic process is stopped.

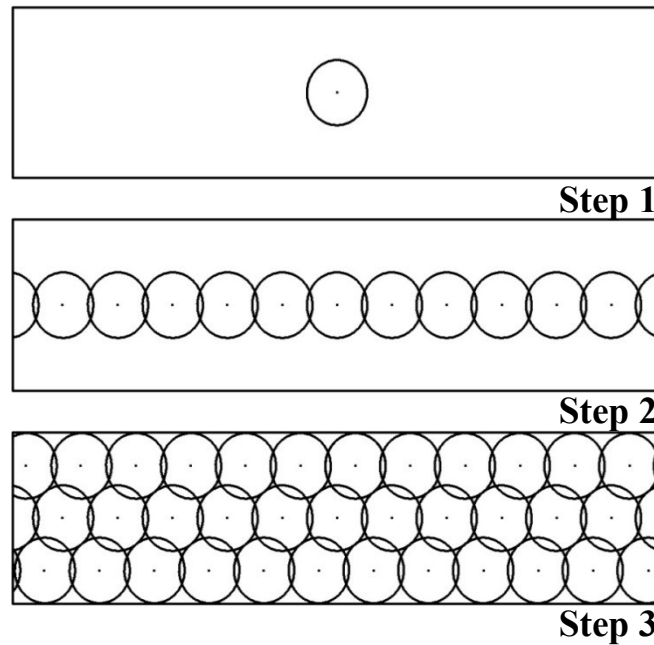


Fig. 2.11. The Three Steps of the Model Based Collimator Design Method. Step 1- For a given collimator sleeve radius, estimate the amount of detector area covered by a single pinhole projection. Step 2- Estimate the number of pinholes that can be placed on the central ring of the collimator. Step 3- Estimate the total number of rings of pinholes that can be used while still allowing at least half of the pinhole projection to project onto the surface of the detector.

The output of the model based method for both the HR MPH collimator and the GP MPH collimator can be seen in Fig. 2.12. These plots show the calculated geometric efficiency at the center of the collimator's CVOV as well as the total number of pinholes used in the collimator for a given collimator sleeve radius. To describe the salient features of these plots, the results for the GP MPH collimator will be discussed. It is important to realize that initially, the collimator consists of a single ring of four pinholes placed at the center of ring detector. As the collimator sleeve radius increases, geometric efficiency decreases because the pinholes are moved farther away from the center of the

CVOV and because the size of the pinhole aperture decreases in order to maintain the target system resolution. Eventually a point is reached where an additional pinhole can be placed in the ring without adjacent pinhole projection images overlapping by more than 20%. This is due to the decrease in pinhole magnification that occurs as the collimator sleeve radius increases; the additional pinhole results in an increase in geometric efficiency, which is why the plots have a saw tooth nature. A significant increase in geometric efficiency occurs when the collimator sleeve radius reaches 24.6 mm. At this collimator sleeve radius, two additional rings of pinholes can be placed on the collimator sleeve without adjacent pinhole projection images overlapping by more than 20%. Furthermore, at 35.9 mm, another two additional rings of pinholes are added to the collimator, meaning that at this point the collimator has five rings of pinhole. However, at this collimator sleeve radius there is not much increase of an increase in total geometric efficiency because the effective pinhole aperture required to maintain the target system resolution is 0.27 mm, and because the pinholes are far from the CVOV. Finally, due to the detector pixel size of 1.6 mm, a collimator with system resolution of 1.5 mm cannot be achieved when the collimator sleeve radius is greater than 37.1 mm. The plot for the HR MPH collimator can be similarly understood except that the maximum collimator sleeve radius that can be used is 29.7 mm because the target system resolution is higher.



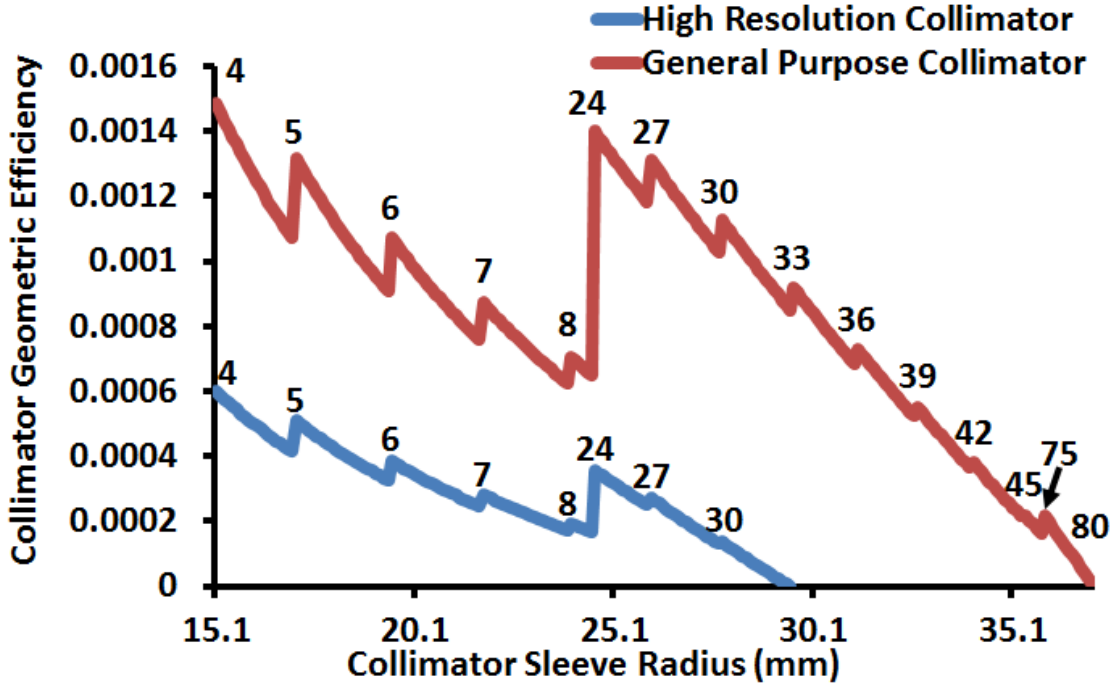


Fig. 2.12. Collimator Design Results using the Model Based Method for High Resolution and GP MPH collimators. The black numbers near the curves show the total number of pinholes used in the collimator.

### 2.1.1.7. Comparison of Collimator Design Methods

Fig. 2.13a and 2.13b compare the results obtained using the area based method and the model based method for each of the collimator designs, while Fig. 2.13c compares the number of pinholes to be used with the GP MPH collimator at different sleeve radii estimated by the two methods. The plots start at 24.5 mm as this is the shortest collimator sleeve radius that can be used due to space taken in the SPECT/MR system by the MR RF coil that is placed inside the collimator, while also allowing at least 2 mm between the inner diameter of the collimator and the pinhole. Both design methods show that collimator designs with smaller sleeve radius length will have higher geometric efficiency. However, for both the high resolution and GP MPH collimators, the

maximum geometric efficiency estimated by the model based method is higher than the estimate made with the area based method.

The reason for this variation will now be discussed. First, as detailed earlier, the projection of a spherical CVOV onto a flat surface is a circle, but the projection of the same CVOV onto a curved surface is an ellipse. The ellipse's radius in the curved direction of the detector is smaller than the radius of the circular projection onto a flat surface. The area based method does not take this into account and therefore underestimates the total number of pinhole projections that can fit onto the detector surface when the collimator radius is smaller. This is demonstrated in Fig. 2.13c. Between collimator sleeve radii of 24.6 mm and 32.2 mm, the area based method estimates that fewer total pinholes can be fit on the collimator. This underestimation has a greater effect on the estimation of the MPH collimator's geometric efficiency when the collimator sleeve radius is smaller because the increased magnification of the projection images means that there are fewer total number of pinholes. In turn, this means that each pinhole has a greater contribution to the geometric efficiency of the collimator.

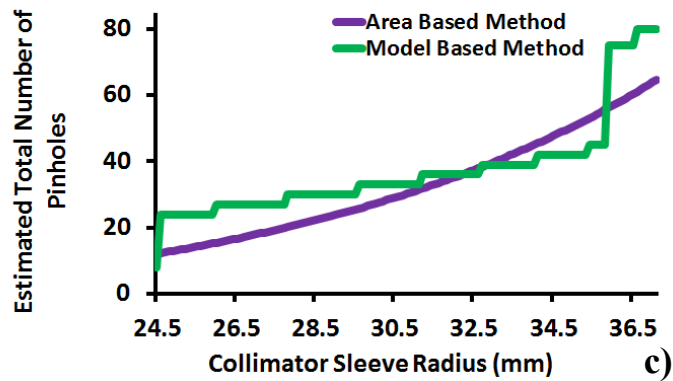
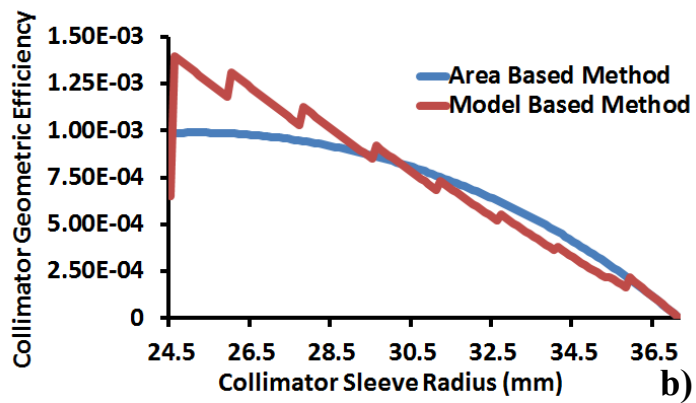
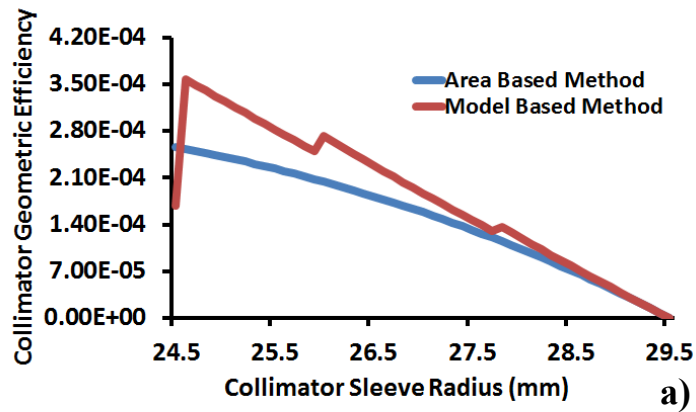


Fig. 2.13. Comparison of Area Based Method to Model Based Method for the HR MPH collimator (a), GP MPH collimator (b), and comparison estimation of total number of pinholes for the GP MPH collimator (c).

As collimator sleeve radius increases, the size of each projection image from each pinhole decreases. The curvature of the detector has less of an effect on each projection image, and the estimation made by the area based method of the total number of pinhole that can be used improves. However, this improvement can lead to an overestimation of the geometric efficiency of the collimator. This is because the area based method does not take into account the decrease in geometric efficiency caused by the tilted pinholes, as was discussed earlier. Despite the limitations discussed, the area based method can still be used to determine MPH collimator design parameters. In fact, the model based method was not developed until after the MPH collimator design parameters had been finalized, using design parameters determined using the area based method. The final design parameters for both the High Resolution and the GP MPH collimators will be shown in Section 3.1.1.

### **2.1.2. Methods to Evaluate Final Multi-pinhole (MPH) Collimator Designs Through Simulation**

Before implementing either of the collimator designs, the designs were evaluated through simulations. The purpose of these simulations were to determine whether the collimators were capable of obtaining SPECT images with the designed target system resolutions and to find the minimum number of projections, or collimator rotational stops, needed such that artifact free SPECT images could be reconstructed from the simulated projection sets. In these simulation studies, projections were generated using both an analytical projector and through Monte Carlo methods. The simulated projections were then reconstructed using a 3D ML-EM method that included a pinhole collimator detector

response [55]. The effect of total number of collimator rotations and number of ML-EM iterations used to reconstructed SPECT images used were both studied.

In our simulations, two different digital phantoms were used. The first phantom was the resolution phantom seen in Fig. 2.14; this phantom was based on the design of Data Spectrum’s Ultra Micro Hot Spot phantom [56]. This phantom has six segments with rods of different diameters. In each segment, the distance from center to center of two adjacent rods is equal to twice the rod diameter. This phantom was used to evaluate the resolution of simulated reconstructed SPECT images. As will be shown later, because we own a physical copy of this phantom, we were able to compare actual experimental results with the results of our simulations.

The second phantom used in our simulation studies was the MOBY (Mouse Whole-Body) phantom [57]. For the simulations, the phantom’s pixel intensities were set to simulate an MDP bone scan [58]. This phantom was used to determine whether the two collimators could be used to acquire SPECT images of a more biologically realistic phantom than the resolution phantom. Sample slices of the MOBY phantom are shown in Fig. 2.15.

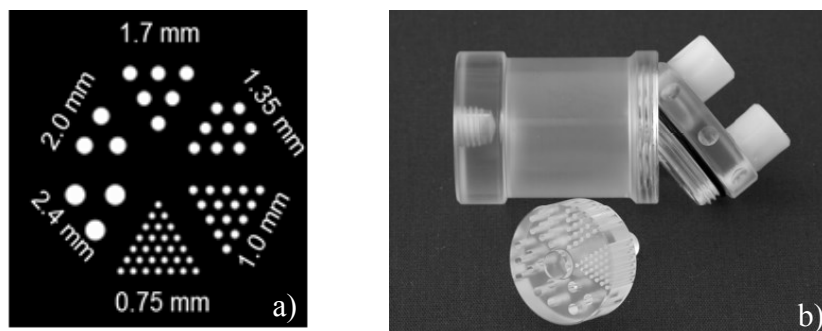


Fig. 2.14. Data Spectrum Ultra Micro Hot Spot Phantom a) Phantom Geometry b) Photograph of Physical Phantom from Data Spectrum’s Website

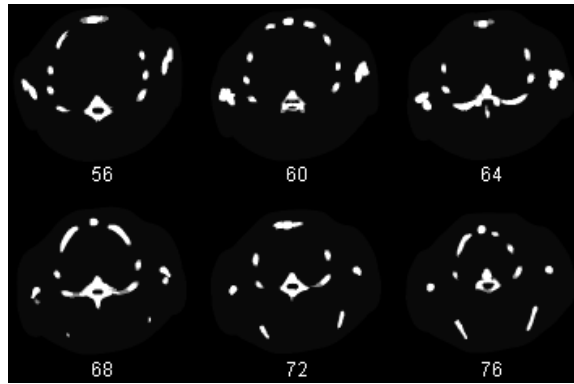


Fig. 2.15. Sample Slices of MOBY Phantom  
Simulating an MDP Bone scan

### **2.1.2.1. Analytical Simulation of Multi-pinhole (MPH) Collimator Designs**

As discussed, when simulating acquisition of the resolution phantom, one of our primary goals was to determine the minimum number of total projection acquisitions needed from each of the two collimators to obtain artifact free reconstructed SPECT images. Initially, we were unsure as to how many projection acquisitions were needed when using the HR MPH collimator, but we hoped that the GP MPH collimator would provide enough views such that additional projection acquisitions were unneeded. To this end, we used an analytical projector with pinhole collimator detector response modeled to simulate acquisition of four projection sets with the HR MPH collimator. The image used to simulate projections had matrix size  $240 \times 240 \times 240$  and pixel length of 0.125 mm. The total number of projection acquisitions and angle of collimator rotation between projection acquisitions for the four projection sets can be seen in Table 2.2. We used the same analytical projector to simulate acquisition of two projection sets with the GP MPH collimator, and parameters of the different projection sets are shown in Table 2.2 as well.

The amount that the collimators were rotated for a given projection set was determined by the number of projection acquisitions in the projection set and the number of pinholes in an individual ring of pinholes. As will be shown in Section 3.1.1.1, in the HR MPH collimator, each pinhole in an individual ring is separated by  $60^\circ$ . Therefore, for each projection set, the amount of collimator rotation was  $60^\circ$  divided by the total number of projection acquisitions in the projection set. This allowed us to obtain equally spaced projection acquisitions for each of the projection sets. Similarly, as will be shown in Section 3.1.1.2, in the GP MPH collimator, each pinhole in an individual ring is separated by  $30^\circ$ . When generating the projection set with two projection acquisitions, the collimator was rotated by  $15^\circ$  to generate two equally spaced projection acquisitions.

Table 2.2: Simulation Parameters for Projection Sets of Resolution Phantom for HR MPH collimator (HRC) and GP MPH collimator (GPC)		
Projection Set Name	Number of Projection Acquisitions	Angle Between Projection Acquisitions
HRC Projection Set 1	1	N/A
HRC Projection Set 2	2	$30^\circ$
HRC Projection Set 3	3	$20^\circ$
HRC Projection Set 4	4	$15^\circ$
GPC Projection Set 1	1	N/A
GPC Projection Set 2	2	$15^\circ$

Simulated SPECT images of the phantom were then reconstructed using a 3D ML-EM method with modeled pinhole collimator detector response. The reconstructed images had matrix size  $120 \times 120 \times 120$  with pixel size 0.25 mm. The image quality of the simulated images was evaluated in terms of image resolution and amount of reconstruction artifacts. Results of these simulations will be shown in Section 3.1.2.1.

As will be shown in greater detail in Section 3.1.2.1, we found that when using the HR MPH collimator, acquisition of three projections with  $20^\circ$  rotation between each acquisition (HRC Projection Set 3 in Table 2.2) was sufficient to obtain SPECT images

free of reconstruction artifacts. Furthermore, we found when using the GP MPH collimator, acquisition of a single set of projections was sufficient for artifact free SPECT images (GPC Projection Set 1 in Table 2.2). These two acquisition strategies were then used in the remainder of the simulations that will now be described.

Analytical projections of the MOBY phantom described in Section 2.1.2 were generated using with an analytical projector with pinhole collimator detector response modeled. The phantom had image matrix size of 240x240x240 with pixel size 0.125 mm. Simulated SPECT images were reconstructed using a 3D ML-EM method with pinhole collimator detector response modeled. Reconstructed images had matrix size 120x120x120 with pixel size 0.25 mm. Results of this simulation will be discussed in Section 3.1.2.2.

#### **2.1.2.2. Monte Carlo Simulation of Multi-pinhole (MPH) Collimator Designs**

To perform a more realistic simulation of imaging the resolution phantom, the Monte Carlo program GATE [59] was used to generate projection sets of the phantom for each of the two collimator designs. The main purpose of this study was to validate the results obtained from the simulations performed using the analytical projector. When simulating the HR MPH collimator, a projection set containing three projection acquisitions was generated; the projection acquisitions were separated by a collimator rotation of 20° between each acquisition. When simulating the GP MPH collimator, the projection set containing a single projection acquisition was generated. Each projection acquisition contains approximately 10 million counts to ensure that the projection sets had low noise properties. This allowed us to ensure that any artifacts observed were not



due to noisy projection sets and instead from the image reconstruction. Simulated SPECT images of the resolution phantom were reconstructed using the same 3D ML-EM method used to reconstruct images from the analytical projections. Results of this simulation will be discussed in Section 3.1.2.3.

### **2.1.3. Method to Implement Final Multi-pinhole (MPH) Collimator Designs**

To implement the SPECT/MR system's MPH collimators, it was necessary to use nonmagnetic materials to allow the collimators to be taken safely into the MRI system's operating room. The collimators were built with three components: a hollow plastic shell, high density tungsten powder, and solid tungsten pinhole inserts. Tungsten was used as the shielding material because it features a high linear attenuation coefficient and is not magnetic. However, to reduce the amount of conductive material taken into the MRI system, the walls of the collimator were shielded using high density coated tungsten powder. This material was chosen in an attempt to reduce eddy currents in the MPH collimator. As described in [60], the gradient coils of the MR system can induce eddy currents on conductive material within the MR system. In turn, these eddy currents can produce additional magnetic fields which can impact the image quality of acquired MR images. For this reason, coated tungsten powder with minimal conductivity was chosen to minimize the induced eddy current on the MPH collimator. The only part of the collimator that used solid metal were the pinhole inserts, which were machined. This ensured that the pinholes all had the exact (or nearly exact) pinhole diameter and cone angle when determining final collimator design parameters. Any variance in the pinhole's aperture would affect the collimator's resolution and geometric efficiency, while variance

in the pinhole's cone angle would affect the size of the collimator's CVOV as well as the amount of projection multiplexing. Sample pinhole inserts for both collimators can be seen in Fig. 2.16.

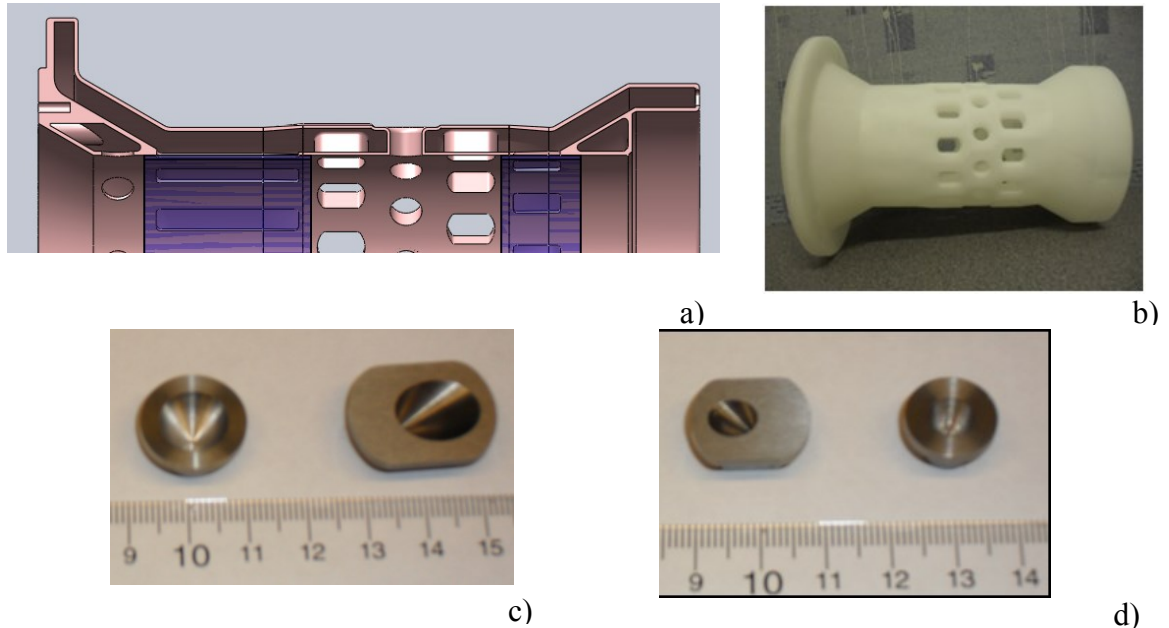


Fig. 2.16. Materials Used to Implement MPH Collimator a) 3D drawing of plastic collimator shell of GP MPH collimator. b) Plastic shell for GP MPH collimator. c) Tungsten pinhole inserts for HR MPH collimator. d) Tungsten pinhole inserts for GP MPH collimator

The pinhole inserts was held in place using plastic shells, also shown in Fig. 2.16. These shells were designed by a mechanical engineer from Gamma Medica. The shells are not perfectly cylindrical but are instead polygonal. This modification allows each individual pinhole insert to lie flush against the surface of the shell. Although the shells are not cylindrical, they are designed such that all of the prototype collimator design parameters match exactly with the designed MPH collimator parameters.

The plastic shells were fabricated using a rapid prototyping method called stereolithography. They were designed with 1 mm plastic walls on the inner and outer diameter of the collimator, with a 5 mm gap in between. We calculated that after filling

the 5 mm gap with high density tungsten powder, 99.99% of all photons with energy 140 keV would be absorbed by the collimator walls. In this calculation, we assumed that the high density tungsten powder had a density of 10 g/cm<sup>3</sup>.

The procedure to fabricate the prototype collimators will now be discussed. First, the interiors of the plastic shells were flushed with water to guarantee that any leftover support material from the manufacturing of the collimators was washed away. Any support material left inside the hollow shell would take away space that would otherwise be used by the high density tungsten powder. As such, it was very important to completely clear out the hollow plastic shells as otherwise the collimator shielding would be weakened, and gamma photons could potentially pass through the collimator walls and reach the detector. Then, each pinhole insert was stuck into a separate socket of the plastic shell and fastened with epoxy. After allowing the epoxy to dry, the collimator was completely filled with the high density tungsten powder. While filling the collimator, the collimator was continuously tapped while rotating the collimator shell in order to make sure that the powder settled uniformly throughout the collimator. This process allowed us to make sure that the collimator had been completely filled. After this, the collimator was sealed with epoxy, to ensure that the tungsten powder would remain inside the collimator during experiments. Finally, the outside of the plastic shell was coated with a mixture of epoxy and tungsten powder, to allow for additional shielding. A photograph taken during the fabrication of the GP MPH collimator is shown in Fig. 2.17.



Fig. 2.17. Photograph of GP MPH collimator being filled with High Density Tungsten Powder

## **2.2. Development of Energy Calibration, Uniformity Calibration, and Lorentz Force Drift Correction Methods for the SPECT/MR System**

The following section will discuss the system calibration methods developed to process experimental data acquired using the SPECT/MR system. As discussed in Section 1.4.4, proper calibration of SPECT imaging systems is needed in order to obtain images with high image quality. When calibrating a SPECT system, measurements of certain properties of the system are taken, and these measurements are then used to apply corrections to acquired experimental data. Without proper system calibration, image quality of reconstructed SPECT images will be impacted in terms of image contrast, uniformity, resolution, and by the generation of image artifacts. Although methods to calibrate typical clinical SPECT systems are well known, the ring type geometry, the CZT modules used to construct the detector of our SPECT/MR system, and the large

number of total detector pixels (24,320) in our system's detector posed unique calibration challenges. In this section, we will introduce the challenges faced when calibrating our SPECT/MR system and then discuss the new calibration methods that we developed to tackle these challenges. Specifically, this section will discuss the methods developed to perform both energy and uniformity calibration for all 24,320 pixels of the SPECT/MR system simultaneously. This section also discusses imaging studies conducted with our SPECT/MR system to evaluate the performance of the developed system calibration methods.

Additionally, this section will also discuss a method developed to correct for the effect that the Lorentz force has on the performance of our SPECT/MR system while acquiring SPECT and MR data simultaneously. Without this correction, experimental results show that any reconstructed SPECT image from data acquired during simultaneous SPECT/MR acquisition will be dominated by artifacts.

### **2.2.1. Method to Acquire Detector Flood Image Used to Study SPECT/MR System Detector Energy and Uniformity Properties**

Traditionally, to study the detector uniformity of a gamma camera, a planar flood phantom is used [15]. This phantom is a thin rectangular shell that fits over the entire detector surface. When filled with activity and placed onto the detector, a flood image can be obtained which is used to measure the detector's intrinsic uniformity can be measured. However, because of the geometry of the SPECT/MR system's ring shaped detector, it is not feasible to acquire uniformity data using a traditional planar flood phantom. An alternative phantom used to obtain a flood image for our SPECT/MR System will now be discussed.

### 2.2.1.1. Annular Shell Phantom Used to Acquire Flood Images

To acquire detector flood images, we fabricated an annular cylindrical shell phantom with an outer diameter equal to the SPECT/MR detector's inner diameter. As shown in Fig. 2.18., the cylindrical shell phantom fits tightly within the detector, and is held close to the detector surface. When the cylindrical shell phantom is filled with activity, the performance of the system when all of its pixels are active can be studied. As will be shown, the data acquired using this phantom allowed us to study each pixel's energy binning performance and sensitivity. In turn, this data was used to develop an energy binning performance and sensitivity. In turn, this data was used to develop an energy calibration method as well as a detector uniformity calibration method.

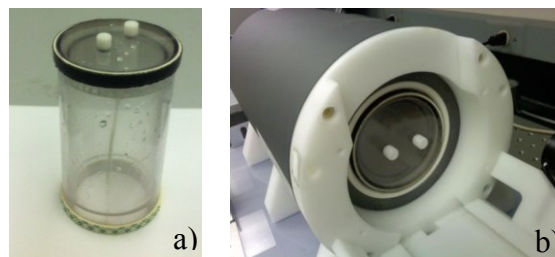


Fig. 2.18. Annular cylindrical shell phantom used for flood acquisition of SPECT/MR system a) Photograph of cylindrical shell phantom b) Phantom inserted into SPECT/MR detector after collimator has been removed

### 2.2.1.2. Measurement of SPECT/MR Detector Count Rate Performance

Because the cylindrical shell phantom is placed directly against the SPECT/MR system's detector, the system can easily be flooded if the cylindrical shell phantom is filled with too high an amount of activity. If this happens, the system will start dropping counts of detected photons, causing a reduction in count rate. Because the measurements obtained using the cylindrical shell phantom are integral to the system calibration

methods, it was important to determine how the detector performed when different amounts of activity were used to fill the phantom. To study this, the cylindrical shell phantom was filled with Tc-99m solution with activity of ranging from 10  $\mu\text{Ci}$  to 150  $\mu\text{Ci}$ . After inserting the cylindrical shell phantom into the detector, data was acquired for ten minutes and the total system count rate was determined. Results of this simple experiment are shown in Fig. 2.19.

From this, we demonstrated that the system was capable of acquiring at most approximately 200,000 counts per second (cps), and that the cylindrical shell phantom should be filled with at most 17  $\mu\text{Ci}$ . Beyond this amount, the SPECT/MR system began to drop counts, reducing the total count rate. This is very useful to know, as it shows us the highest amount of activity that can be used when acquiring data with the cylindrical shell phantom. In turn, this allows us to acquire data at the highest possible count rate, which allows us to obtain higher count flood images of the SPECT/MR system's detector while taking less time to acquire the data.

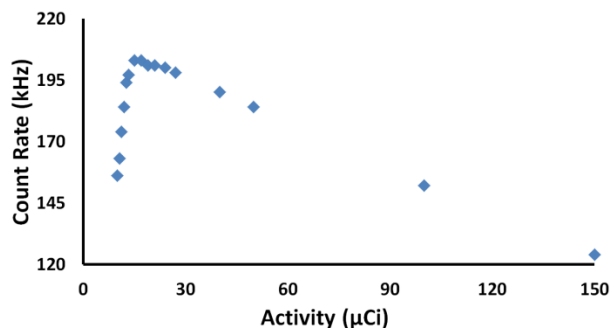


Fig. 2.19. SPECT/MR system detector count rate using the cylindrical shell phantom filled with Tc-99m at different levels of activity

## **2.2.2. Development of SPECT/MR System Calibration and Correction Methods**

The following section will discuss how the flood image data acquired using the annular shell phantom was used to develop an energy calibration and detector uniformity calibration method for the SPECT/MR System. Additionally, a method developed to correct for the effect of the Lorentz force drift that is seen in data acquired in the presence of a strong magnetic field. The procedure used to apply the developed calibration and correction methods to acquired experimental data was be discussed as well.

### **2.2.2.1. SPECT/MR Detector Energy Calibration Method**

As discussed in Section 1.3.1, traditional clinical SPECT systems utilize pulse height analyzers to determine the energy of detected gamma photons and to provide a guide to determine an energy window which accepts detected photons within the photopeak and rejects detected photons outside the energy window. These energy windows are used to identify and reject detected photons that have been scattered. If included in the acquired projection image, scattered photons will decrease image contrast of reconstructed SPECT images. The SPECT/MR system stores acquired data in a list-mode format, which means that, during an acquisition, the position, detection time, and energy of every detected gamma photon are stored. The energy calibration method that will be discussed in this section is used to generate an initial projection image from list-mode data acquired during imaging experiments. This is done by measuring and storing separate energy windows centered on the photopeak of the detected photons used for imaging for each separate detector pixel using data acquired with the annular shell phantom.



After an acquisition, the list-mode data can be binned into a matrix with dimensions 24320x1024. Each row in this matrix contains all of the photon counts acquired by a single detector pixel. For each pixel, acquired photon counts are stored in 1024 separate energy bins. As shown in Fig. 2.20, an energy spectrum for each pixel can be generated from this data. A projection image can be generated from the list-mode data by first summing a portion of each pixel's spectrum to determine the total number of detected photons within the chosen energy range. Then, each pixel in the projection image is assigned the value of the number of photons detected in the energy range during the acquisition. However, because of variations in the module ASICs, each pixel stores different energies in different bins. This is also demonstrated in Fig. 2.20. Most notably, the photopeak for Tc-99m is stored in different energy bins for each pixel. As described, the energy calibration method is used to generate energy windows centered on the photopeak of the isotope used for imaging for each separate detector pixel. These stored energy windows can then be used to process acquired experimental data. Each energy window had two parameters that we needed to determine: the energy bin that the window needed to be centered on and the width of the energy window. The following will describe how data acquired with the annular shell phantom was used to determine these parameters.

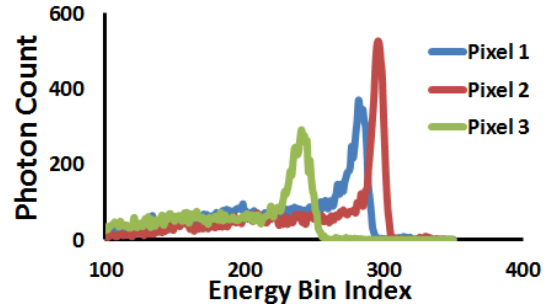


Fig. 2.20. Acquired energy spectra from three separate detector pixels from annular shell phantom

Using the acquired data from the annular shell phantom, we were able to identify the photopeak energy bin for each pixel as it corresponded with the energy bin with the highest number of detected photons. This bin was used as the bin that each energy window was centered on. To determine the width of the window used in the energy calibration process, the following procedure was used. First, for each pixel, the portion of the pixel's energy spectrum that contained the photopeak was extracted and then fit to a standard Gaussian curve. From this curve, we were able to calculate the FWHM of the energy spectrum from each pixel, and from there determined the average FWHM for all detector pixels. The average FWHM was used as the width for each energy window.

After we were had measured the photopeak bin for each pixel and determined an energy window width, we were able to develop an energy calibration method for the SPECT/MR system using data acquired with the annular shell phantom. First, for a given pixel, the bin containing the photopeak of the isotope being imaged is identified. Then, the energy bin indices for an energy window with width equal to the average energy spectrum FWHM for the isotope being used and centered on the photopeak of the pixel are stored to be used as an energy window for that pixel. This procedure is then repeated for each pixel.

At the completion of the energy calibration procedure, a complete set of energy windows to be used to process acquired experimental data is stored. These stored energy windows are integral when processing experimental data as it would not be possible to easily identify the photopeak of the isotope being used for imaging from experimental data alone. This is demonstrated in Fig. 2.21, which shows a sample energy spectrum from data acquired with the cylindrical shell phantom and from data acquired when imaging a resolution phantom when the SPECT/MR system was fitted with the GP MPH collimator. Both spectra are from the same pixel.

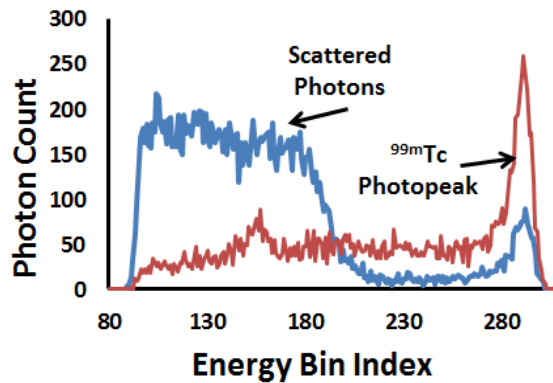


Fig. 2.21. Sample energy spectrum for same pixel from cylindrical shell phantom (red) and phantom imaging experiment (blue)

As shown, during the resolution phantom study, the energy bin with the highest number of counts is a bin that contains counts from detected photons with a much lower energy than the Tc-99m photopeak. These counts are from Compton scattered photons and if they had been included in the projection image, the contrast of the reconstructed SPECT image would be reduced. However, because we identified the Tc-99m photopeak when using the cylindrical shell phantom, scattered counts can be rejected are not

included in the projection image. The improvement in image quality that the energy calibration method has on reconstructed SPECT images will be shown in Section 3.2.3.

#### **2.2.2.2. SPECT/MR Detector Uniformity Calibration Method**

Due to variations in pixel sensitivity, there are significant uniformity distortions to any projection image acquired with the SPECT/MR system. If left unchecked, these distortions will introduce artifacts in SPECT images reconstructed from acquired projection images. For example, these non-uniformities can cause high or low pixel intensities in regions that should be uniform. They can also cause streaking artifacts to appear throughout the reconstructed image, which can degrade the reconstructed image's resolution. The purpose of the uniformity calibration method is to identify and correct for these non-uniformities.

Although all pixels have a different sensitivity, during normal operation approximately 2.5% of the pixels in the SPECT/MR detector require special consideration. If not properly identified and accounted for in the uniformity calibration process, these pixels will degrade the image quality of reconstructed images. Our uniformity calibration method corrects for non-uniformities due to both variances in pixel sensitivity as well as the detector pixels that required special consideration. After processing acquired data with the uniformity calibration method, artifacts caused by uniformity distortions are removed from the reconstructed SPECT image and the image quality is significantly improved. Data acquired using the annular shell phantom was used to generate the uniformity correction map and to identify pixels in the detector that needed special consideration. The method used to obtain the uniformity correction map and the location of pixels that needed special consideration will now be discussed.

After using data acquired with the annular shell phantom to store the location of energy windows for each pixel, the energy windows are used to produce a flood image for the entire detector from the acquired data. This is done by summing the counts from all energy bins that are within the energy window for each pixel and then setting each pixel in the flood image equal to the value of the sum. The flood image is used to study the effect of pixel sensitivity on the flood image's count distribution and to create a uniformity correction map. It is also used to identify the 2% of the detector pixels that do not function properly. These pixels have been divided into four categories: dead, malfunctioning, hypoactive, and hyperactive.

Dead pixels, if not accounted for, will introduce regions of low pixel intensity in the reconstructed image. These are pixels that never detect any photons, and the pixel value stored in the projection image for these pixels is always zero. In our SPECT/MR system, dead pixels are not a significant concern as there are only ten dead pixels throughout the entire detector. Almost just as uncommon are the pixels that were identified as malfunctioning. These pixels continuously register counts at a rate of several thousand counts per second, regardless of whether there is any activity in the detector. Although there are only eight malfunctioning pixels in the SPECT/MR detector, it is important that they are taken into account. If they remain in the projection image, they will introduce high intensity regions to the reconstructed image.

The other two pixel types, hypoactive and hyperactive pixels, are identified through analysis of the flood image. Hypoactive pixels are defined as any pixel in the detector flood image with a count that is 25% less than the mean of the flood image, while hyperactive pixels are defined as any pixel with a count that is greater than 75% of

the mean of the flood image. Without correcting for these pixels, they will introduce hot and cold spots in the reconstructed SPECT image, as well as streaking artifacts.

The acquired flood image is integral to the uniformity correction method. After generation of the flood image from the acquired list-mode data, dead, malfunctioning, hypoactive, and hyperactive pixels are all identified in the flood image, and their locations are stored. Then, to generate a uniformity correction map, the flood image is normalized by the maximum value of the pixels not considered dead, malfunctioning, hypoactive, or hyperactive. The uniformity correction map and the location of all of the nonstandard pixels are saved to process experimental projection data.

### **2.2.2.3. Application of System Calibration Method to Acquired Data**

To apply the energy calibration and uniformity calibration methods to acquired experimental data when using the SPECT/MR system as a standalone SPECT system, the following procedure is used. First, the acquired list-mode data is used to generate an initial projection image. The value of each pixel in the projection image is obtained using the energy windows that were stored in the energy calibration process. For each pixel, the sum of the energy bins in the energy window is used as that pixel's value in the initial projection image. The projection image is stored in a matrix with size 80x304. Then, the value of every pixel previously identified as dead, malfunctioning, hypoactive, or hyperactive during the uniformity calibration procedure is set to zero. The uniformity correction map generated from the flood image data is then used to correct for non-uniformities in the projection image by dividing the initial projection image by the uniformity correction map pixel by pixel. After this, the dead pixels, malfunctioning pixels, hypoactive pixels, and hyperactive pixels are corrected for. A one dimensional

linear interpolation along the axial direction of the detector is applied to the projection image to replace the values of the pixels that had been set to zero with values interpolated from surrounding pixel values. Finally, the image is changed from a two dimensional image with size 80x304 to a three dimensional image with size 80x16x19. These dimensions correspond to the dimensions of the detector as each panel of the 19 panels has dimension of 80x16. Once these steps have been taken, the projection image can be used to reconstruct a SPECT image.

#### **2.2.2.4. Lorentz Force Drift Correction Method for Data Acquired in the Presence of a Magnetic Field**

The procedure detailed in 2.2.2.3 is not sufficient to process data acquired during simultaneous SPECT/MR image acquisition. This is because during simultaneous SPECT/MR acquisition, the Lorentz force [29] causes the charged particles produced by photons interacting with the CZT detector modules to deflect inside the detector module before being collected, as shown in Fig. 2.22. If not corrected for, the deflection of the charged particles will significantly impact the image quality of reconstructed SPECT images from experimental data acquired during simultaneous SPECT/MR studies.

As shown in Equation 16, the equation for the Lorentz force repeated from Section 1.3.1.3,

$$\vec{F} = q(\vec{E} + \vec{v} \times \vec{B}) \quad (16)$$

the amount of drift that the electron experiences is determined by the strength of the magnetic field, the voltage applied across the CZT detector module, and the depth in the module that the photon interaction that produced the electron occurred in. In this work, simultaneous SPECT/MR acquisition was performed in a 3T magnetic field, and voltage

applied across each CZT detector module was 500V. It was calculated that the average drift experienced by an electron was approximately 1.6 mm. By chance, this happens to be the side length of a single pixel in our detector.

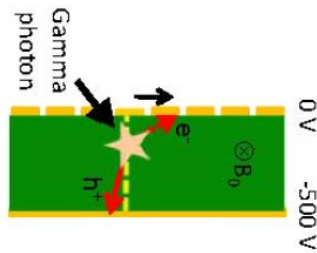


Fig. 2.22. Effect of Lorentz force on CZT Detector Module. The charged particles produced by interaction of a gamma photon with the detector will drift inside the detector module before reaching collection circuitry.

This drift causes two significant issues which need to be accounted for before acquired projection images can be used to reconstruct SPECT images. First, the drift causes detector modules to register counts from photons in a different region of the module than the photons were detected in. If a model for the drift is not included in the algorithm used to reconstruct the SPECT images from the acquired data, the drift must be corrected for while processing the acquired experimental data. Otherwise, there will be significant artifacts in the reconstructed SPECT image to the point where artifacts dominate the reconstructed image. To correct for this issue, the pixels in the projection image were shifted in the direction opposite of the drift, by the average amount of drift experienced by moving electrons inside the detector module.



The second significant issue caused by the Lorentz force drift has to do with the uniformity calibration of the SPECT/MR system's detector. Fig. 2.23 shows a sample flood image of one of the detector modules that was acquired in the presence of a magnetic field. The red arrow shows the direction that charged particles drift inside the detector module. As seen, there is a significant depletion of counts in the last column of the module. This occurs because there are no charges that drift into this column as it is at the edge of the module, while most charges that would be counted in that column have drifted to its neighboring column.

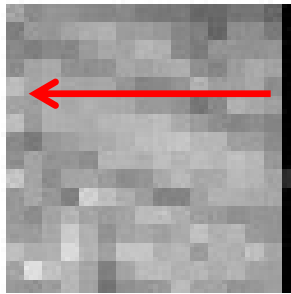


Fig. 2.23. Sample detector module flood image acquired in the presence of a magnetic field. Direction of drift of charged particles is shown with the red arrow.

As previously discussed in Section 2.2.2.2 and 2.2.2.3, special care was taken in the uniformity calibration process to correct for hypoactive pixels. Because of the depletion caused by the Lorentz force, every pixel in the last column of every detector module acts as if it was a hypoactive pixel. Practically, this means that every 16<sup>th</sup> column of projection data acquired in the presence of a magnetic field must be replaced by interpolated values from surrounding pixels. However, as described in Section 2.2.2.3, dead pixels, malfunctioning pixels, hypoactive pixels, and hyperactive pixels were all replaced through the use of a one dimensional interpolation along the axial direction of

the detector. When the projection image is missing an entire column, as is the case here, interpolation along the axial direction cannot be performed. To solve this problem, we developed a modified version of the calibration method to process data acquired in the presence of a magnetic field; this version will now be discussed.

#### **2.2.2.5. Application of System Calibration Method to Data Acquired in the Presence of a Magnetic Field**

In this section, the modified procedure used to apply the system calibration method to data acquired in the presence of a magnetic field will be described. To begin, data is acquired with the annular cylindrical shell phantom while the system is in the presence of a magnetic field. After following the same procedure for energy calibration and generation of a flood image, each pixel value in the flood image is shifted in the direction opposite of the drift caused by the Lorentz force by one pixel. The positions of dead, malfunctioning, hypoactive, and hyperactive pixels are then identified in shifted flood image. During this process, all pixels in the columns shown in Fig. 2.23 that were depleted due to the drifting are considered hypoactive pixels. All nonstandard pixels are then set to zero, and a uniformity correction map is generated by normalizing the shifted flood image by its largest pixel value. The modified uniformity correction map is then saved, and locations of nonstandard pixels are stored.

When processing acquired experimental data, the same energy calibration procedure described in Section 2.2.2.1 is used. However, prior to saving the projection image, the pixel value in the projection image is shifted in the same direction that pixels were shifted for the uniformity correction map. After the initial projection image is saved, variations in pixel sensitivity are corrected for by dividing pixel by pixel the projection

image by the modified uniformity correction map. Then, a one dimensional interpolation in the axial direction is used to correct for dead, malfunctioning, hypoactive, and hyperactive pixels as was done before. Following this interpolation, a second one dimensional interpolation is applied in the transaxial direction of the projection image to correct for the depletion caused by the drift in the last column of each detector module. After applying the second interpolation, the projection image is ready to be used to reconstruct a SPECT image.

### **2.2.3. Evaluation of the SPECT/MR System Calibration and Correction Methods**

Phantom imaging experiments were conducted with the SPECT/MR system to evaluate the effect of applying the developed system calibration methods on acquired data. In these experiments, we were imaging known structures which meant we knew what to expect from each acquired image. Therefore, we could compare our images with what was expected to evaluate our calibration methods. SPECT images were reconstructed before and after applying the system calibration methods to projection images, and the reconstructed image quality of the reconstructed SPECT images were evaluated in terms of improvement of contrast, resolution, and uniformity, as well as in terms of artifact reduction. Results of these experiments will be shown in Section 3.2.

During imaging experiments, the SPECT/MR system was fitted with the prototype GP MPH collimator described in Section 2.1.1.3. There are several reasons why we chose this collimator to evaluate our calibration methods. First, the GP MPH collimator was designed to be able to acquire sufficient projections to reconstruct artifact free SPECT images with a single projection acquisition, while the HR MPH collimator

needed at least three projection acquisitions to acquire images free of reconstruction artifacts. Furthermore, the GP MPH collimator has a higher geometric efficiency than the HR MPH collimator. Both of these factors meant that we would be able to acquire a high count projection image set with sufficient views using the GP MPH collimator in less time than it would take to acquire a comparable image using the HR MPH collimator. Additionally, when acquiring simultaneous SPECT/MR data, the collimator cannot be rotated without disrupting the acquisition of the MR image. As a result, the HR MPH collimator cannot be easily used for simultaneous SPECT/MR imaging. For these reasons, we used the GP MPH collimator during the imaging experiments to evaluate the system calibration methods.

### **2.2.3.1. Evaluation of System Calibration Method with Annular Shell Phantom**

To evaluate the effect of the uniformity calibration on the detector, two separate flood acquisitions were acquired using the cylindrical shell phantom. The data from the first set was used for energy and uniformity calibration while the data from the second set was processed as if it was an experimental projection image, following the method described in Section 2.2.2.3. The main goal of this experiment was to determine how much detector uniformity improves after application of the system calibration methods. If we were unable to obtain a uniform flood image after application of the system calibration method, we would also not be able to reconstruct artifact free SPECT images from projections processed using the same calibration. Therefore, processing a flood image was a useful initial assessment of the performance of our system calibration method.

To this end, to obtain a quantitative measurement of the improvement of the uniformity of the entire flood image after the calibration method was applied, the Integral and Differential Uniformity of the flood image was calculated before and after application of the system calibration method to the flood image using the NEMA standard method[15]. Additionally, the uniformity in particular regions of the detector were evaluated by taking line profiles through sections of the processed flood image.

### **2.2.3.2. Evaluation of System Calibration Method with Uniform Cylinder Phantom**

To assess the image uniformity of reconstructed SPECT images acquired with the SPECT/MR system, a uniform cylinder with both inner diameter and length of 28 mm and filled with a 10 mCi Tc-99m solution was imaged. Before acquisition, the center of the cylinder was placed at the center of the collimator's CVOV. While imaging, two projection acquisitions were acquired for one hour each, with 15° collimator rotation between the first and second acquisition. If the uniformity calibration method was not working properly, the SPECT image of the cylinder would have high and low intensity regions (hot and cold spots). When conducting a preclinical experiment, hot or cold spots can lead to over or underestimation of the amount of uptake of the radiopharmaceutical injected. Therefore, this study was important to determine whether the system has acceptable image uniformity after application of the uniformity calibration.

From this acquisition, we generated three distinct projection sets. The first projection set was generated using the energy calibration method, without application of any uniformity correction. To generate the second projection set, we applied our uniformity correction map to the first projection set, but did not correct for the effect of

dead, malfunctioning, hypoactive, and hyperactive pixels. Finally, the third projection set was generated after applying the complete system calibration method described in section 2.2.2.3.

SPECT images from all three projection sets were reconstructed using a 3D ML-EM method with pinhole collimator response modeled with 10 iterations. Images were reconstructed with matrix size with 121x121x121 with pixel size of 0.25 mm. For each image, a 2 mm slice of the central region was extracted. The uniformity of each SPECT image was assessed visually for uniformity artifacts. Additionally, reconstructed image uniformity was quantitatively evaluated using image profiles and calculation of integral uniformity within the reconstructed image.

### **2.2.3.3. Evaluation of System Calibration Method with Resolution Phantom**

To assess the effect of the system calibration method on reconstructed SPECT images with fine details acquired with the SPECT/MR system, the Ultra Micro Hot Spot Phantom, described earlier in Section 2.1.2, was imaged. The phantom was filled with a 35 mCi Tc-99m solution. Before acquisition, the center of the section of the phantom containing the rod segments was placed at the center of the collimator's CVOV. While imaging, two projection acquisitions were acquired for 45 minutes each, with 15° collimator rotation between the first and second acquisition. This phantom experiment allowed us to study how our system calibration method improves the resolution of reconstructed images. This is something that we could not study with the uniform cylinder experiment described in Section 2.2.3.2. We were also able to use data acquired during this experiment to evaluate the energy calibration method; specifically, this

phantom experiment allowed us to demonstrate how the contrast of an acquired image improves when the energy calibration method is applied to acquired data.

To study the effect of our uniformity correction method on the reconstructed SPECT image of the resolution phantom, we generated three projection sets from the acquired data. The first projection set was generated using the energy calibration method, without application of any uniformity correction. To generate the second projection set, we applied our uniformity correction map to the first projection set, but did not correct for the effect of dead, malfunctioning, hypoactive, and hyperactive pixels. Finally, the third projection set was generated after applying the complete system calibration method described in section 2.2.2.3.

SPECT images from all three projection sets were reconstructed using a 3D ML-EM method with pinhole collimator response modeled with 70 iterations. Images were reconstructed with matrix size with 121x121x121 with pixel size of 0.25 mm. For each image, a 2 mm slice of the central region was extracted. Each SPECT image was assessed visually for uniformity and streaking artifacts. Additionally, reconstructed image quality was quantitatively evaluated using image profiles across rods in four of the six segments of the phantom. The rod segments chosen had diameters of 2.4 mm, 2.0 mm, 1.7 mm, and 1.35 mm; the other two segments of the phantom containing rods with diameters of 1.0 mm and 0.75 mm were not evaluated because these rods could not be resolved due to the resolution of the collimator.

To evaluate the energy calibration method, a projection set from the data acquired using the Ultra Micro Hot Spot phantom was generated without first applying the energy windows stored during the energy calibration process. For each pixel, instead of only

using the sum of the energy bins within the energy windows, the entire energy spectrum was used. This meant that scattered photons that were detected were included in the projection image. The projection set was then calibrated with a uniformity correction map and that was generated from a flood image that also used the entire energy spectrum for each pixel. Correction for the effect of dead, malfunctioning, hypoactive, and hyperactive pixels was also applied. In this case, nonstandard pixels were identified using the flood image that used the entire energy spectrum for each pixel.

A SPECT image from this projection set was reconstructed using a 3D ML-EM method with pinhole collimator response modeled with 70 iterations. Images were reconstructed with matrix size with 121x121x121 with pixel size of 0.25 mm. A 2 mm slice containing the central region of the image was then extracted. The contrast between the rod and background was calculated using this image as well as the image of the resolution phantom reconstructed from the projection set processed with the energy calibration and the entire uniformity calibration method.

#### **2.2.3.4. Evaluation of System Calibration Method and Lorentz Force Correction Method with Resolution Phantom**

To evaluate the modified system calibration method developed for acquisition of simultaneous SPECT/MR images, we imaged the Ultra Micro Hot Spot phantom during a simultaneous SPECT/MR imaging experiment. Details about the procedure for this experiment will be discussed in Section 2.3.4. The goal of this experiment was to determine whether the pixel shift method described in Section 2.2.2.4 and 2.2.2.5 would be sufficient to correct for the drift that charged particles experience when acquiring SPECT data in the presence of a magnetic field.



After acquisition, two projection sets were generated. In the first set, both energy calibration and uniformity calibration were applied to the acquired data, but we did not apply the pixel shift to correct for Lorentz force drift. In the second projection set, energy calibration, uniformity calibration, and Lorentz force drift were applied. SPECT images from both projections were reconstructed with a 3D ML-EM method with pinhole collimator response modeled with 40 iterations. Both images were assessed for artifacts due to the Lorentz force shift.

To further study the effect of rotationally shifting the pixels of projection images acquired to correct for the Lorentz force drift, a set of shifted projection images were generated from the original, nonshifted, projection image acquired in the presence of a magnetic field. This projection image was rotationally shifted 3.0 mm in 0.2 mm increments in the direction opposite of the Lorentz force drift. Each shifted projection image was then reconstructed. All 16 images were evaluated in terms of appearance of artifacts due to Lorentz force shift.

### **2.3. Procedures for Experimental Evaluation of SPECT/MR System**

In this section, we will discuss phantom and preclinical experiments conducted to evaluate the SPECT/MR system. Studies discussed in this section include both standalone SPECT and SPECT/MR studies.

#### **2.3.1. Standalone SPECT Imaging of Resolution Phantom with Tc-99m**

As discussed in Section 2.2.3.3, one of the first experiments conducted with the SPECT/MR system was imaging of the Data Spectrum Ultra Micro Hot Spot phantom. Images acquired with this phantom were used to evaluate the system calibration method but we were also able to use data acquired when imaging this phantom to evaluate key

performance characteristics of the SPECT/MR system. When imaging with a phantom, the distribution of the activity in the phantom is known and the reconstructed SPECT image can easily be compared with what was expected. Therefore, imaging the Ultra Micro Hot Spot Phantom allowed us to evaluate the accuracy of the SPECT/MR system and the reconstruction method used to reconstruct SPECT images of the phantom from acquired experimental data. Furthermore, imaging the Ultra Micro Hot Spot phantom allowed us to evaluate the system resolution and to determine whether the system was capable of acquiring images at the resolutions that each of the two collimators were designed for.

Data acquired from imaging the Ultra Micro Hot Spot phantom was also used to validate the analytical and Monte Carlo simulations described in Section 2.1.2. As mentioned, the simulation results showed that when using the HR MPH collimator, to obtain a SPECT image with minimal reconstruction artifacts, three projection acquisitions with  $20^\circ$  collimator rotation were needed. Similarly, the simulations also showed that when using the GP MPH collimator, a single projection acquisition could be used to obtain a SPECT image with minimal reconstruction artifacts. Imaging the Ultra Micro Hot Spot phantom allowed us to determine whether these projection acquisition strategies were sufficient to reconstruct SPECT images from acquired experimental projection data. Additionally, this experiment also allowed us to evaluate the image quality of reconstructed SPECT images obtained when varying the number of projection acquisitions used in the reconstruction of the images.

The following procedure was used to acquire standalone SPECT images of the Ultra Micro Hot Spot Phantom with each of the collimators designed for the SPECT/MR

system. At the start of data acquisition, the phantom will be filled with a 55 mCi Tc-99m solution when using the HR MPH collimator and filled with a 37.8 mCi Tc-99m solution when using the GP MPH collimator. These phantom activities were chosen to allow us to acquire data at high count rates when using both of the collimators. Preclinical experiments conducted later used a much lower level of activity, as will be shown. For both experiments, the phantom was inserted into the system such that the center of the phantom's insert containing the rods was at the center of the SPECT/MR system's CVOV. During both experiments, projection data was acquired at six different equally spaced collimator positions. As discussed in Section 2.1.2.1, the HR MPH collimator has pinholes that are spaced  $60^\circ$  apart from each other. Thus, to obtain six equally spaced projection acquisitions, the collimator was rotated  $10^\circ$  between each acquisition. Similarly, the GP MPH collimator has pinholes that are spaced  $30^\circ$  apart from each other. Therefore, the collimator was instead rotated  $5^\circ$  between each acquisition.

In order to obtain data with low noise, it was desirable to obtain projection acquisitions at each collimator position with a high number of counts. To take into account the decay of Tc-99m during the experiment, the following acquisition strategy was used. First, after inserting the phantom and collimator into the detector, data was acquired for 30 minutes. Then, the collimator was rotated clockwise, either  $5^\circ$  or  $10^\circ$  depending on which collimator was being used, after which data was acquired again for another 30 minutes. This process continued until the sixth projection view position was reached. At the sixth projection view position, data was acquired for one hour. Then, the collimator was rotated counterclockwise by the same amount that it had been rotated, and a second set of data at that position was acquired. This process of acquiring data then

rotating the collimator counterclockwise was continued until data was acquired at each of the other projection views. At the end of the experiment, data had been acquired for one hour in each of the six collimator positions. In all cases, the acquired data was stored in a list-mode format.

After the data acquisition was finished, the list-mode data from each of the experiments were processed using the calibration method described in Section 2.2.2.3. For each of the collimators, four projection sets were generated. Table 2.3 shows the number of projection acquisitions and the rotation between projection acquisitions for each of the experimentally acquired projection sets.

It should be noted that the some of the acquisition shown in Table 2.3 are different from the simulated acquisitions shown earlier in Table 2.2. Specifically, HRC Projection Set 4 has a greater number of projection acquisitions, and GRC Projection Sets 3 and 4 were not included at all in the simulations shown earlier. This is because in this experiment, we wanted to obtain projection sets with more projection acquisitions than were simulated. The collimators in the SPECT/MR system can only be rotated to repeatable positions every  $5^\circ$ . Therefore, given the angular spacing between pinholes for both the HR MPH collimator and the GP MPH collimator, projection sets with one, two, three, and six projection acquisitions were obtained in this experiment. This allowed for acquisition of equally spaced projection acquisitions with both the HR MPH collimator and the GP MPH collimator, as shown in Table 2.3

Projection Set Name	Number of Projection Acquisitions	Angle Between Projection Acquisitions
HRC Projection Set 1	1	N/A
HRC Projection Set 2	2	30°
HRC Projection Set 3	3	20°
HRC Projection Set 4	6	10°
GPC Projection Set 1	1	N/A
GPC Projection Set 2	2	15°
GPC Projection Set 3	3	10°
GPC Projection Set 4	6	5°

When generating the projection sets acquired using the HR MPH collimator from acquired list-mode data, the list-mode data was processed such that the projections sets contained approximately the same total number of counts, regardless of the number of projection acquisitions in the projection set. Furthermore, for a projection set with more than one projection acquisition, each of the projection acquisitions had approximately the same count level. The same can be said for the four projection sets generated using data acquired using the GP MPH collimator. The data was processed in this way to allow us to study the effect that varying the number of projection acquisitions had on the reconstructed SPECT image's quality. If the total number of counts in the projection sets were not approximately equal, any improvement in image quality could potentially have come from the total number of counts in the projection set, rather than the number of projection acquisitions in the projection set.

After generation of the projection sets, SPECT images of the phantom were reconstructed using a 3D ML-EM method with modeled pinhole collimator detector response with 0.25 mm pixel size and image matrix size 120x120x120. A 4 mm slice of each reconstructed image containing the central slice was extracted. Reconstructed images were evaluated for image quality in terms of reconstruction artifacts and image

resolution at different ML-EM iterations. To evaluate the accuracy of the image reconstruction, we measured the center to center distance between adjacent rods in reconstructed images. The average of all measured center to center distances for each segment was measured, and compared with the true center to center distance.

### **2.3.2. Standalone SPECT Imaging of Mouse Skull Tc-99m MDP**

The first live animal imaging experiment conducted with the SPECT/MR system was a Tc-99m MDP bone scan of a mouse's skull. This experiment was conducted using both the High Resolution and the GP MPH collimators. The purpose of this experiment was to demonstrate that the image acquisition strategies determined using the simulations discussed in Section 2.1.2 would work during a small animal imaging experiment and to compare the performance of the HR MPH collimator with the GP MPH collimator when performing a live imaging experiment. Additionally, this experiment was used to gain experience in using the SPECT/MR system to image a live subject.

The following procedure was used for this experiment. First, a mouse was fastened to an imaging bed and then anesthetized to prevent the mouse from moving during the imaging experiment. Then, the mouse was positioned such that the center of the mouse's skull was at the center of the system's CVOV. The mouse was then injected with Tc-99m MDP. When imaging with the HR MPH collimator, 8 mCi 99mTc MDP was used, and when imaging with the GP MPH collimator, 5 mCi 99mTc MDP was used. During image acquisition with the HR MPH collimator, data was acquired at three separate positions for 13 minutes each. After each projection acquisition, the collimator was rotated by 20° before starting the next acquisition. When imaging with the GP MPH collimator, data was acquired at two separate positions for 18 minutes each. After each

acquisition, the collimator was rotated by 15° before starting the next acquisition. Different mice were used for imaging with the two collimators. Finally, both of the mice were sacrificed and their remains were disposed of safely.

The acquired data was processed using the developed calibration methods, and SPECT images were reconstructed with a 3D ML-EM with modeled pinhole collimator response and matrix size 121x121x121 with pixel size 0.25 mm. Images were evaluated at 40<sup>th</sup> ML-EM iteration, and the resolution of the two reconstructed images were compared.

### **2.3.3. Standalone SPECT Imaging of Mouse Kidneys with Gadolinium Nanoparticles Labeled with Tc-99m**

Another experiment performed to evaluate the system's performance as a standalone SPECT system was the use of Tc-99m labeled gadolinium nanoparticles to image a mouse's kidneys. The main objective of this experiment was to demonstrate that the nanoparticles could be used for imaging with the SPECT/MR system. As gadolinium can be used as an MR contrast agent, these nanoparticles could potentially be used as an agent for simultaneous SPECT/MR imaging, and this experiment served to evaluate agent's efficacy as an agent for SPECT imaging. It was assumed that the nanoparticles would be passed to the mouse's kidneys after being injected into the mouse because the nanoparticles were attached to DTPA, a drug that uptakes in kidneys [61].

The following procedure was used for this experiment. First, the SPECT/MR system was fitted with the GP MPH collimator. This collimator was used because we wanted to determine whether it was possible to acquire an image of the mouse's kidneys without having to obtain additional projection acquisitions by rotating the collimator.

Then, a mouse was fastened onto the imaging bed, given an anesthetic, and then injected with ~0.2 mL of the gadolinium nanoparticles labeled with 5 mCi of Tc-99m. After the mouse was prepared for imaging, the imaging bed was placed inside the system, with the center of the mouse's kidneys placed at the center of the system's CVOV. Data was then acquired for 5 minutes. The SPECT/MR system's acquisition software displays a preview of the projection image as it is being acquired. As expected, the Tc-99m gadolinium nanoparticles collected in the mouse's kidneys after injection. After data acquisition, the mouse was sacrificed and safely disposed of.

SPECT images of the mouse's kidney were reconstructed using a 3D ML-EM reconstruction method with pinhole collimator detector response modeled. The images were reconstructed with matrix size 121x121x121 with 0.25mm/pixel. Reconstructed images of the kidney were evaluated for reconstruction artifacts and image resolution.

#### **2.3.4. Simultaneous SPECT/MR Imaging of Resolution Phantom with Tc-99m**

To conduct simultaneous SPECT/MR imaging experiments, our SPECT/MR system was taken to a clinical 3T Philips MR system as shown in Fig. 2.24. In our experimental set up, the MR RF coil was inserted inside the collimator. The coil was then connected to the MR system's console to allow it to be used in MR image acquisition. After placing the SPECT/MR system on the MR system's bed, the SPECT/MR system was moved to the center of the MR system. Ethernet cables were run from the SPECT/MR system to a data collection box which was chained to a wall and kept as far away as possible to the MR system. The output of the data collection box was connected via an Ethernet cable to an Ethernet to Optical Fiber converter box. Optical Fibers were then run from the converter



box, through a pipe, and then out to the MR system's control room. The fibers were then connected to a second converter box, which was connected to a laptop via an Ethernet cable. This set up allowed us to control the SPECT/MR system and to store acquired SPECT data while the room housing the MR system was sealed, which is required for operation of the MR system.



Fig. 2.24. SPECT/MR System placed inside clinical MR scanner for simultaneous SPECT/MR data acquisition.

The first simultaneous SPECT/MR experiment conducted utilized the Data Spectrum Ultra Micro Hot Spot phantom. The primary objective of this experiment was to demonstrate that the system could acquire high quality simultaneous SPECT/MR images. This experiment was also used to study the effect that the MR system had on the image quality of the acquired SPECT image and the effect that the SPECT/MR system had on the acquired MR image. Because the distribution of activity in the phantom was known, as well as the phantom's structure, both the SPECT and MR images that were acquired could be compared with what was expected.

The following procedure was used for this experiment. First, the system was fitted with the GP MPH collimator and an MR RF coil was inserted into the center of the collimator. The phantom, which had been filled with a 35 mCi Tc-99m solution, was

inserted into the system such that the center of the phantom was at the center of the system's CVOV. Next, the SPECT/MR system was moved to the center of the MR system. Our MR collaborators controlling the MR system then determined a pulse sequence that would allow us to acquire an MR image at the center of phantom. It is important to note that this was not straightforward. Distortions were observed by our MR collaborators that affect the MR sequences used during MR slice selection. However, after the MR system was configured to obtain an image of the phantom, the MR image was not affected by the distortions. Then, we began acquiring SPECT data in a list-mode format while simultaneously acquiring MR data. Both SPECT and MR data acquisition lasted for ten minutes. To study the effect that the active SPECT/MR system had on the MR system's performance, the SPECT/MR system was then shut off and a second MR image of the phantom was acquired. Finally, the phantom was removed from the system and the activity was disposed of properly.

Projection images were generated from the acquired data using the system calibration and correction method described in Section 2.2.2.5. SPECT images were reconstructed using a 3D ML-EM reconstruction method with pinhole collimator detector response modeled. The images were reconstructed with matrix size  $121 \times 121 \times 121$  with 0.25 mm/pixel. A 4 mm slice of each reconstructed image containing the central slice was extracted. Reconstructed images were evaluated at different ML-EM iterations in terms of reconstruction artifacts and reconstructed image resolution. Furthermore, image quality of the phantom image acquired during simultaneous SPECT/MR acquisition was compared with a phantom image acquired during standalone SPECT acquisition.

To make a fair comparison between the image obtained during standalone SPECT acquisition and the image obtained during simultaneous SPECT/MR acquisition, a portion of the list-mode data from a single collimator acquisition from the standalone phantom SPECT experiment was extracted such that it had nearly the same number of counts as the SPECT acquisition obtained during the simultaneous SPECT/MR experiment. This was done to make sure that both images had similar noise properties. Furthermore, only data from a single projection acquisition from the standalone SPECT experiment was extracted because the collimator was not rotated during the simultaneous SPECT/MR phantom experiment. Reconstructed images of the phantom were compared at 40<sup>th</sup> ML-EM iteration.

In addition to comparing the image quality of phantom images acquired during standalone SPECT and simultaneous SPECT/MR acquisition, the accuracy of the reconstructed images were compared by measuring the center to center to distance of adjacent rods, using the same method described in Section 2.3.1. The center to center distance between adjacent rods in the 2.4 mm, 2.0 mm, 1.7 mm, and 1.35 mm segment were measured and compared with the true distances.

We also evaluated the acquired MR image of the phantom. Using the same method to measure distances between adjacent rods for the SPECT images, the distance between adjacent rods in the MR image for all six of the phantom segments were measured. This allowed us to determine whether there was any geometric distortion in the acquired MR image due to the presence of the SPECT/MR insert.

Finally, to determine whether the SPECT and MR images acquired simultaneously were in good agreement with each other, the SPECT image was

registered with the MR image using a 2D rigid body transform. The two images were then fused together.

### **2.3.5. Simultaneous SPECT/MR Imaging of Mouse Kidneys with Tc-99m MAG3**

The last experiment that will be discussed is a simultaneous preclinical SPECT/MR imaging experiment that was conducted using Tc-99m MAG3. MAG3 is a drug that is taken up into a patient's kidneys and then washes out into the bladder [62]. The main purposes of this study were to demonstrate that the SPECT/MR system was capable of simultaneously acquiring high quality SPECT and MR small animal images and to demonstrate the SPECT/MR system's capability to acquire dynamic images. Because the SPECT/MR system acquires data in a list-mode format, the acquired data can be broken up into separate time frames. Each of the time frames can be processed separately and reconstructed into a SPECT image corresponding to that time frame. The same slice in each frame image can then be stacked together in order to generate a dynamic image, showing how the MAG3 distribution changes throughout time during the experiment. Furthermore, we also used a dynamic MR pulse sequence in order to acquire MR image frames. However, because we did not attach an MR contrast agent to the MAG3, the acquired MR images do not show any changes throughout the acquisition.

The following procedure was used to conduct this experiment. First, the SPECT/MR system was taken to a 3T clinical MR system and the MR RF coil was inserted into the GP MPH collimator. Then, a mouse was fastened to the SPECT/MR system's imaging bed and a catheter was stuck into the mouse's tail vein. After this the mouse was anesthetized and the imaging bed was inserted into the SPECT/MR system

such that the center of the mouse's kidneys was placed approximately at the center of the SPECT/MR system's CVOV. The SPECT/MR system was then moved the center of the MR system. Then, our MR collaborators determined a multislice pulse sequence that allowed us to obtain an MR image of the mouse's kidney with five slices with thickness of 1 mm with 0.75 mm gap between slices. As before, this was not a straightforward task due to distortions caused by the SPECT/MR system. However, after the MR system was configured to acquire images of the mouse's kidneys, there were minimal distortions observed in the MR images. Next, the SPECT/MR system was set to acquire data in a list-mode format for 30 minutes. Our animal technician then injected ~3.5 mCi in 0.25 mL of Tc-99m MAG3 as quickly as possible. We began acquiring SPECT data before injecting the mouse with MAG3 in order to image the initial uptake of the MAG3 into the mouse's kidneys. The animal technician then left the MR system's room as quickly as possible and our MR collaborators then began acquiring MR data with a dynamic pulse sequence that allowed us to obtain a frame of the multislice image every 80 seconds. During the imaging experiment, 22 MR images were acquired. After the experiment was completed, the mouse was removed from the SPECT/MR system and carefully disposed of.

Two different projection sets were generated using the SPECT data that was acquired during this experiment. First, a single static projection acquisition was generated using all thirty minutes of the acquired list-mode data. This projection acquisition does not show the initial uptake and later washout of the Tc-99m MAG3 into the mouse's kidney. A SPECT image was reconstructed from this static projection acquisition and the kidney image was compared with the kidney image obtained in the experiment described

in Section 2.3.3. Images were reconstructed using a 3D ML-EM reconstruction method with modeled pinhole collimator response. Images had matrix size 121x121x121 with pixel size 0.25 mm and reconstructed with 25 ML-EM iterations. We also generated a static MR image averaging the 22 dynamic frames acquired with the MR system.

To study whether there was any geometric distortion in either the SPECT or MR images due to the simultaneous acquisition, we registered the static SPECT image with the static MR image. We first collapsed the SPECT image such that the slice thickness was 1 mm, which matched the slice thickness of the MR image. Then, for each static MR image slice, the corresponding static SPECT image was found. Using a 2D rigid transform, the SPECT image was registered with the MR image. Finally, the registered SPECT and MR images were fused together.

In addition to the static SPECT image, a set of dynamic SPECT images showing the initial uptake and washout of the Tc-99m MAG3 into and out of the mouse's kidneys were reconstructed. To do this, the list-mode data was extracted in ten second intervals, for a total of 180 list-mode frames. Then, each list-mode file was processed separately, leaving us with 180 projection acquisitions. Each projection acquisition corresponded to 10 seconds of data acquisition. These dynamic projection acquisitions were each reconstructed separately using a 3D ML-EM reconstruction method with modeled pinhole collimator response. Images had matrix size 121x121x121 with pixel size 0.25 mm and reconstructed with 15 ML-EM iterations. From each image, a 1 mm slice containing the kidney was extracted. A dynamic image showing the initial uptake and washout of the MAG3 with 10 second frame length was generated by stacking together the same 1mm slice from each of the 180 reconstructed images.

We also generated a dynamic fused SPECT/MR image. The dynamic SPECT image was collapsed into 80 second time frames, corresponding to the same length of time that each MR image was acquired for. Furthermore, the first 5 frames of the SPECT image were discarded, as the MR image was not acquired during this time. Then, using a 2D rigid body transform, each SPECT image frame was separately registered with the corresponding MR image frame. After this, each SPECT and MR image were fused together.

Finally, to further study the uptake and washout of the MAG3, a time activity curve was generated using the reconstructed dynamic SPECT image. Using the reconstructed images from each time frame, a 3D ROI was drawn around each of the kidneys, and the sums of the pixel intensity of the pixels inside the two ROIs for each image frame were calculated.

## **Chapter 3: Results**

### **3.1. Results of Multi-pinhole (MPH) Collimator Design, Evaluation, and Implementation**

In this section, the final designs of the two prototype MPH collimators for the SPECT/MR system will be discussed. As mentioned earlier in Chapter 2, when the designs of the two collimators implemented for the SPECT/MR system were finalized, we had only developed the area based method. The model based method was not developed until later. Therefore, the decisions made to determine the design parameters of the collimators of the SPECT/MR system were made with this method. While discussing the rationale for the final design parameters of the two collimators, the justifications will be made based on results from the area based method. Additionally, results of analytical and Monte Carlo simulations that demonstrate the imaging performance of both collimators will be shown. This section will close with demonstration that the implementation of both collimators was successful.

#### **3.1.1. Final Multi-pinhole (MPH) Collimator Designs**

##### **3.1.1.1. High Resolution Collimator Design Parameters**

As discussed, when designing the HR MPH collimator, our goal was to design a collimator with a target system resolution of 1 mm with the highest possible geometric efficiency. We were not concerned about the number of pinholes in the collimator and allowed for collimator rotation if additional views were needed for SPECT image reconstruction. From Fig 2.8, shown in the previous chapter, it is clear that the optimal collimator sleeve radius is at 24.5 mm as this is the sleeve radius with the highest geometric efficiency after we take the constraint of the MR RF coil into account.



At collimator sleeve radius of 24.5 mm, the area based method estimates that 12 pinhole projection images can be used to fully cover the detector surface. We initially considered a collimator with two rings of pinholes each containing six tilted pinholes. Simulated projections of the CVOV from each pinhole onto the detector surface can be seen in the first image of Fig. 3.1. However, after some deliberation it was decided to change the design to an 18 pinhole configuration, containing three rings of six pinholes each. In this design, the central ring of pinholes is directly above the CVOV while the two side rings of pinholes are tilted such that the maximum amount of projection multiplexing is 20%, as seen in the bottom image of Fig. 3.1. With this second design, there are six full projections and 12 half projections, which utilize similar amounts of total detector surface area.

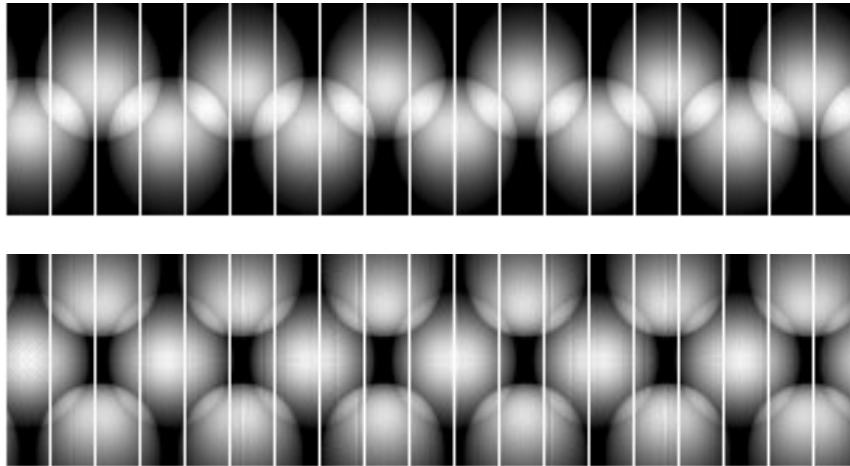


Fig. 3.1. Initial (top) and Final (bottom) Pinhole Layout for HR MPH collimator using the Area Based Method.

There were several reasons why the design for the HR MPH collimator was modified. Most importantly, the geometric efficiency of the 18 pinhole collimator at the center of the CVOV is 30% higher than the geometric efficiency of the 12 pinhole collimator's center. Secondly, as discussed in Chapter 1, the geometric efficiency of a

pinhole decreases at the edges of the pinhole's field-of-view. At the very edge of the pinhole's field-of-view, for a given collimator sleeve radius and pinhole diameter, the pinhole collimator's geometric efficiency will decrease by  $\cos(\varphi)^3$ , where  $\varphi$  is half of the cone angle of the pinhole. This is clearly demonstrated in Fig. 3.1. For any CVOV projection, the intensity of that projection is lower near the projection's edges. This decrease in intensity in the simulated projection corresponds to a decrease in detected counts by the collimator. Furthermore, as discussed in Chapter 2, the geometric efficiency of a tilted pinhole is decreased by  $\cos(\theta)^2$ , where  $\theta$  is the tilt angle. As a result of these two factors, the geometric efficiency of the 12 pinhole collimator design at the edge of the collimator's CVOV is much lower than the geometric efficiency at the center of the collimator's CVOV. This is demonstrated in Fig. 3.1; the intensity at the top and bottom row of the projection image of the 12 pinhole collimator is much lower than the intensity at the center of the collimator.

In comparison, the 18 pinhole collimator design does not have this problem. By increasing the tilt angle of the 12 pinholes, the region of each projection that has the lowest intensity is instead projected off of the edge of the detector. As a result of this truncation, additional space on the detector surface is made available, and a ring of six pinholes can be placed directly over the CVOV. Although half of each tilted pinhole projection is truncated, each pair of tilted pinholes covers the entire CVOV. When combined, each pair of tilted pinholes obtains a single complete view of the CVOV. Although the final design 18 pinholes, the 18 pinhole design obtains the same total number of views as the initial 12 pinhole collimator design. However, the increase in the

number of pinholes used led to a reorganization of the pinhole configuration that allowed for improved geometric efficiency.

### **3.1.1.2. General Purpose Collimator Design Parameters**

For the General Purpose imaging collimator, our goal was to design a collimator with target system resolution of 1.5 mm that provided a sufficient number of views to obtain an artifact free SPECT image without requiring additional collimator rotations while still having a high geometric efficiency. A stationary collimator allows for simultaneous acquisition of both SPECT and MR images without interrupting acquisition of either image. Additionally, a stationary collimator can also be used to perform studies using dynamic radiotracers with fast uptake and washout into and out of organs. When using a ring detector and a collimator that does not need to rotate, data from the organ of interest at all views can be acquired simultaneously throughout the entire experiment. After discussions, it was decided that a collimator with 36 pinholes would be sufficient number for a stationary collimator design.

The area based method was then used to determine the collimator sleeve radius needed to design a collimator with 36 pinholes. Results from the area based method showed that a collimator sleeve radius of 31.5 mm could be used. With this information, a 36 pinhole collimator was designed using Autodesk Inventor to determine a pinhole configuration that would cover the entire detector surface with pinhole projections. As before, projections of the CVOV onto the detector surface were then simulated, and results are shown in Fig. 3.2.

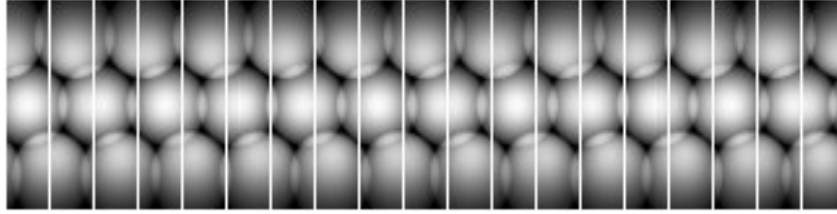


Fig. 3.2. Final Pinhole Layout for GP MPH collimator.

One significant difference between the pinhole configuration of the High Resolution and GP MPH collimators is that, while the outer rings of pinholes in the HR MPH collimator are aligned with each other, the outer rings of pinholes in the GP MPH collimator are not. This allows the GP MPH collimator to obtain a unique view of the object every 10 degrees. In comparison, the HR MPH collimator obtains a view of the object every 30 degrees. As will be demonstrated shortly, the 36 closely packed projection views obtained with the GP MPH collimator are sufficient to reconstruct artifact free SPECT images.

### **3.1.1.3. Final MPH Collimator Design Parameters**

Table 3.1 shows the final chosen design parameters for the MPH collimators designed using the area based method. As mentioned, prototypes of both the High Resolution and the GP MPH collimator were built using these parameters. Although the model based method was not developed until after the collimator designs had been finalized, it is interesting to compare the collimator designs suggested by the model based method with the actual final designs. Potential final designs determined using the model based methods are shown in Table 3.1 as well. In Table 3.1, the rows shown in red text correspond to collimator designs determined by the model based method.

When using the model based method to design the HR MPH collimator, as seen in Fig. 3.13, the model based method shows that with a collimator sleeve radius of 24.6 mm,

a pinhole collimator with three rings of eight pinholes can be implemented. For a collimator with target system resolution of 1 mm, this collimator has a geometric efficiency of  $3.6 \times 10^{-4}$  at the center of the collimator's CVOV. When compared to the actual implemented design, the geometric efficiency is improved by 16%. The geometric efficiency increases because the number of pinholes in the collimator is increased by 33%, but the total gain in geometric efficiency is less than that. This is because the tilt angle for the tilted pinholes is  $39.7^\circ$ , which causes the geometric efficiency of the tilted pinholes to have 59% of the geometric efficiency of the nontilted pinholes at the center of the CVOV. In comparison, in the implemented design of the HR MPH collimator, the tilt angle is  $30.5^\circ$ . This results in the tilted pinholes having a geometric efficiency of that is 74% of the geometric efficiency of the nontilted pinholes.

System Resolution	Collimator Sleeve Radius	# of Non Tilted Pinholes	# of Tilted Pinholes	Pinhole Cone Angle	Tilted Pinhole Cone Angle	Pinhole Aperture	Tilt Angle of Tilted Pinholes	Geometric Efficiency at Center of CVOV
1 mm	24.5 mm	6	12	$75.5^\circ$	$63.68^\circ$	0.3 mm	$30.5^\circ$	$3.1 \times 10^{-4}$
1 mm	24.6 mm	8	16	$75.14^\circ$	$55.94^\circ$	0.28 mm	$39.72^\circ$	$3.6 \times 10^{-4}$
1.5 mm	31.5 mm	12	24	$56.9^\circ$	$50.7^\circ$	0.48 mm	$26^\circ$	$6.9 \times 10^{-4}$
1.5 mm	31.2 mm	12	24	$57.48^\circ$	$50.56^\circ$	0.5 mm	$27.35^\circ$	$7.3 \times 10^{-4}$

As seen in Table 3.1, the collimator design determined by the model based method for the GP MPH collimator is nearly identical to the final collimator design that was implemented. Both collimators have three rings of 12 pinholes, and the geometric efficiencies of both of the collimators are similar. The reasons for this are as follows. First, as discussed earlier, as collimator sleeve radius increases, the estimation of the number of pinholes that can be fit on the collimator made by the area based method improves. Second, the parameters obtained from the area based method were used to

design a collimator with the same pinhole configuration that all collimators designed by the model based method have. Therefore, it is not surprising that the two methods obtained comparable results for the GP MPH collimator.

### **3.1.2. Results of Simulations Used to Evaluate Final Multi-pinhole (MPH) Collimator Designs**

#### **3.1.2.1. Simulated Analytical Projection Sets and Reconstructed SPECT Images of Resolution Phantom**

Following the procedure described in Section 2.1.2.1, we used an analytical projector with collimator detector response modeled to simulate noise free projection sets containing projection images of the Data Spectrum Ultra Micro Hot Spot phantom. Table 3.2, below, shows the total number of projection acquisitions and collimator rotation between projection acquisitions. All generated projection sets are seen in Fig. 3.3 and Fig. 3.4. As will be shown, simulated SPECT images of the resolution phantom were reconstructed from these projection sets.

Projection Set Name	Number of Projection Acquisitions	Angle Between Projection Acquisitions
HRC Projection Set 1	1	N/A
HRC Projection Set 2	2	30°
HRC Projection Set 3	3	20°
HRC Projection Set 4	4	15°
GPC Projection Set 1	1	N/A
GPC Projection Set 2	2	15°

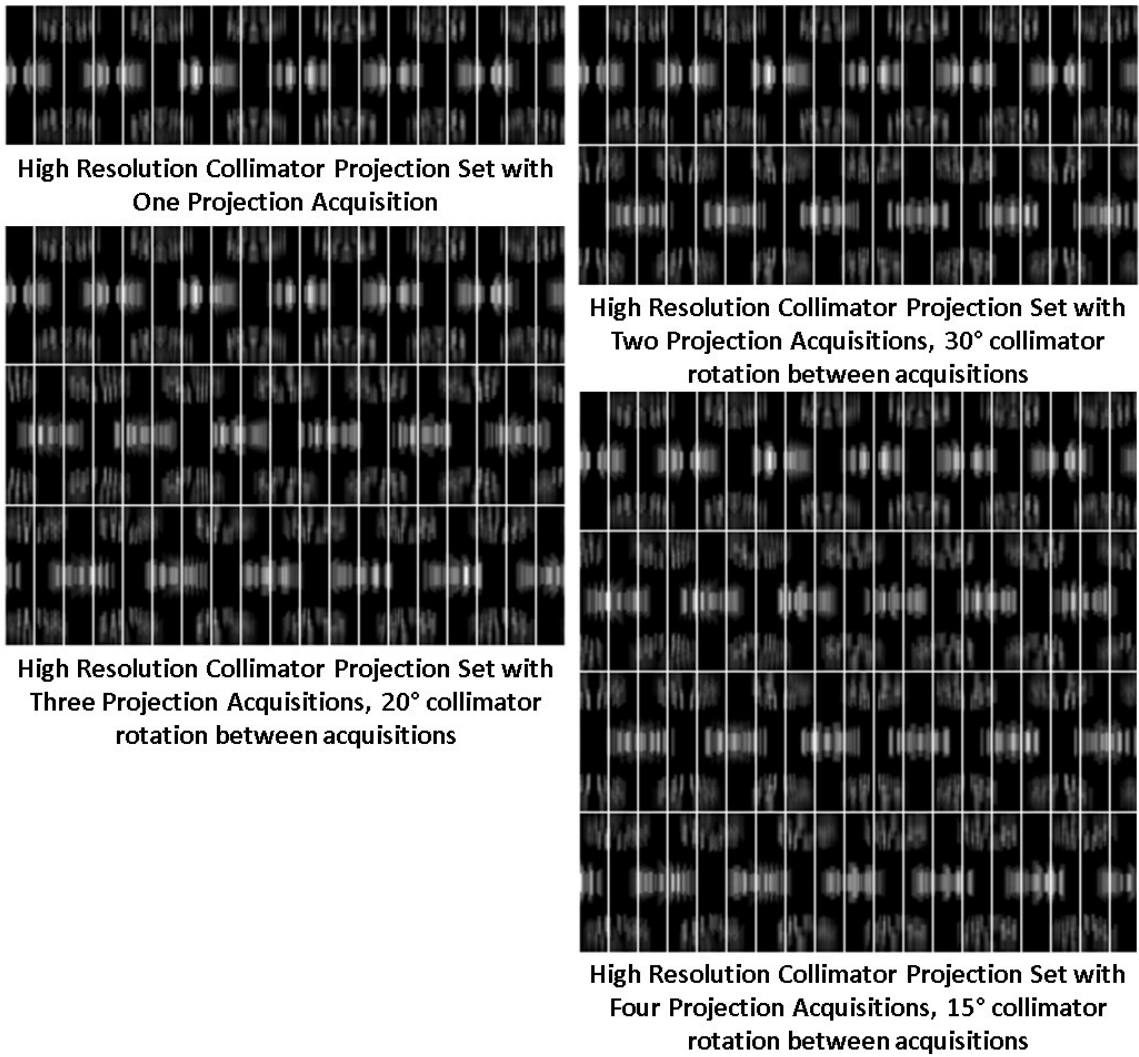


Fig. 3.3. Analytical Simulated Projection sets of the Ultra Micro Hot Spot Phantom generated using the HR MPH collimator. For projection sets with more than one projection acquisition, the amount of collimator rotation between acquisitions is given.

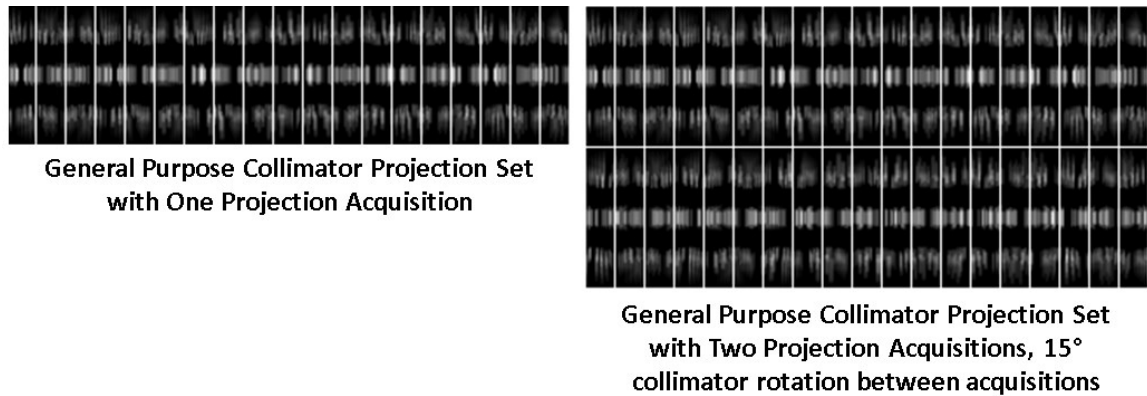


Fig. 3.4. Analytical Simulated Projection sets of the Ultra Micro Hot Spot Phantom generated using the and GP MPH collimator. For the projection sets with more than one projection acquisition, the amount of collimator rotation between acquisitions is given.

SPECT images of the resolution phantom were reconstructed using a 3D ML-EM method with modeled pinhole collimator detector response. The image quality of the simulated images was evaluated in terms of image resolution and amount of reconstruction artifacts. Fig. 3.5 shows simulated SPECT images of the resolution phantom reconstructed from the four projection sets generated to simulate use of the HR MPH collimator. Each image shown is the central slice of the reconstructed image. From visual inspection of the images, it is immediately clear that at least three projection acquisitions are needed to acquire artifact free SPECT images using the HR MPH collimator. There are significant streaking artifacts in all six segments of the reconstructed images of the resolution phantom for the projection sets containing one projection acquisition, regardless of ML-EM iteration number. This is because these projection sets do not contain a sufficient number of views of the phantom. Although image quality improves when using two projection acquisitions, streaking artifacts are still seen in the three phantom segments containing rods with diameters of 1.35 mm, 1 mm, and 0.75 mm. When three or four views are used in the reconstruction, the only



segment of that phantom that is not fully resolved is the segment with 0.75 mm diameter rods. This was expected, as the HR MPH collimator was designed to have system resolution of 1 mm.

It is also interesting to note that as ML-EM iteration number increases, the image quality of the images reconstructed using four projection acquisitions is very similar to the images reconstructed using three projection acquisitions. Because we did not observe a significant improvement in SPECT image quality when using more than three projection acquisitions in a projection set, for further simulation studies, only three projection acquisitions were used.

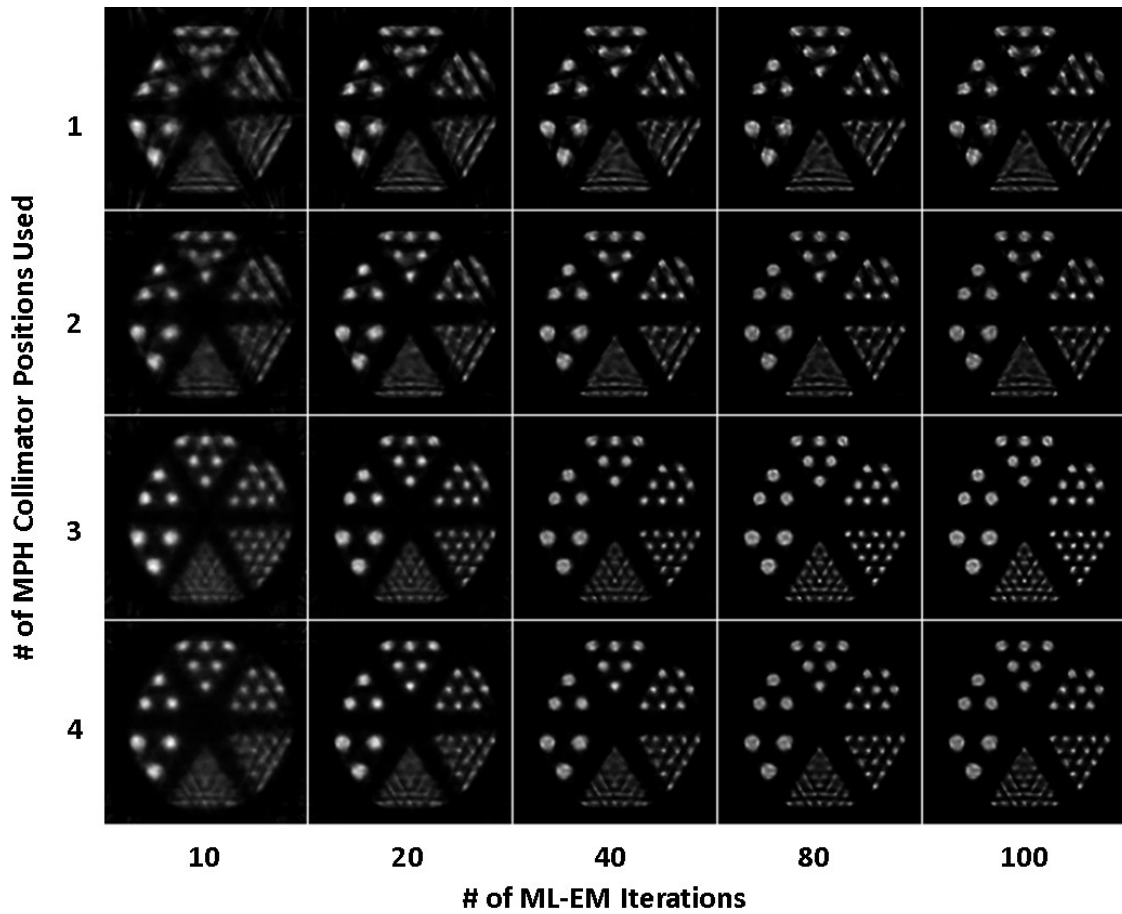


Fig. 3.5. Simulated SPECT Images reconstructed from Analytical Projection Sets Using the HR MPH collimator.

Fig. 3.6 shows simulated SPECT images of the resolution phantom reconstructed from the two projection sets generated to simulate use of the GP MPH collimator. As shown, the images reconstructed using a single projection acquisition have comparable image quality when compared with the images reconstructed using two projection acquisitions. Furthermore, there are very few changes in the reconstructed images after the 40<sup>th</sup> ML-EM iteration. Notably, after the 40<sup>th</sup> iteration, all segments of the phantom except the 1 mm and 0.75 mm segments can be fully resolved. This demonstrates that the collimator design exceeds the target system resolution of 1.5 mm. These simulation results demonstrate that the GP MPH collimator can be used to obtain artifact free

SPECT images without having to rotate the collimator to obtain additional projection acquisitions. This means that the GP MPH collimator can be used for both simultaneous SPECT/MR imaging experiments as well as fast dynamic studies. For further simulation studies with the GP MPH collimator, only a single projection acquisition was used.

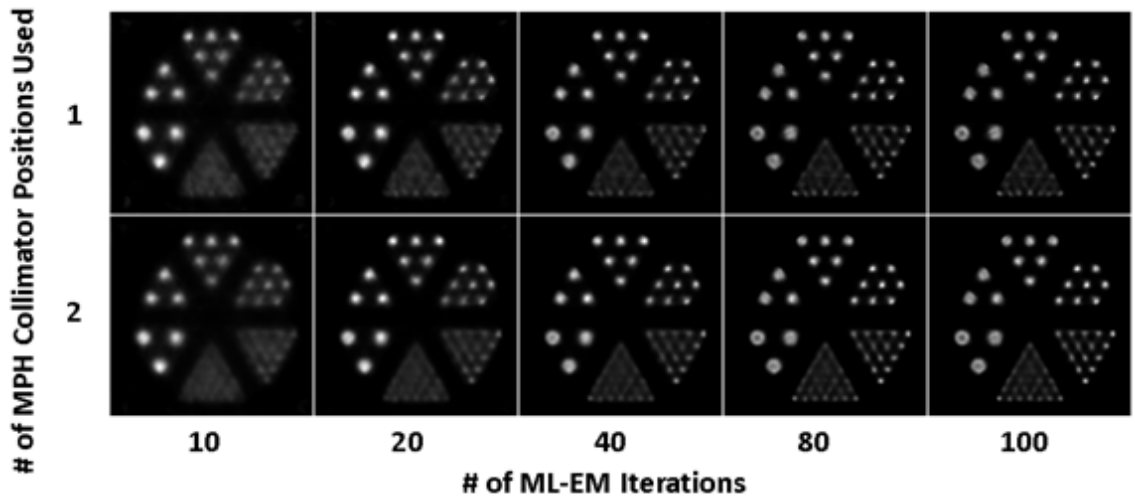


Fig. 3.6. Simulated SPECT Images reconstructed from Analytical Projection Sets Using the GP MPH collimator.

### 3.1.2.2. Simulated Analytical Projection Sets and Reconstructed SPECT Images with MOBY Phantom

As discussed in Section 2.1.2.1, we also used the MOBY phantom to evaluate the performance of both the designed collimators. This phantom allowed us to determine whether the number of projection views needed to reconstruct artifact free images of the resolution phantom were also sufficient to reconstruct artifact free images of a more biologically realistic phantom. In this study, the MOBY phantom intensity values were set to correspond to an MDP bone scan. The mouse's spine and rib cage were placed at the center of the CVOV of both collimators. Simulated projections for both the HR MPH collimator and the GP MPH collimator are shown in Fig. 3.7. For the HR MPH

collimator, as before, the projection acquisitions were separated by a collimator rotation of  $20^\circ$  between each simulated acquisition. For the GP MPH collimator, a single projection acquisition was simulated.

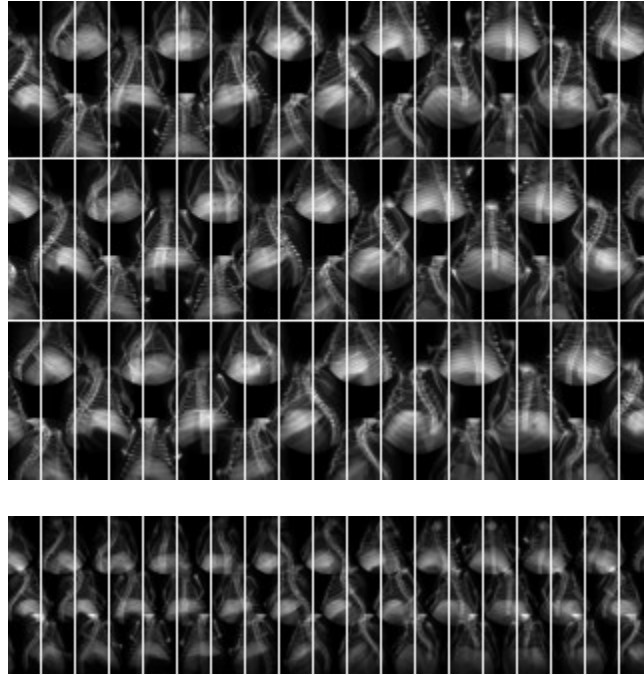


Fig. 3.7. Analytical Simulated Projection sets of the MOBY Phantom generated using the HR MPH collimator (top) and GP MPH collimator (bottom).

Fig. 3.8 shows sample slices of a simulated SPECT image reconstructed from both of the projection sets shown in Fig. 3.7. Each slice shown is separated by 1 mm increment. Furthermore, the fifth slice shown is the central slice of the reconstructed image. For comparison, the same slices from the phantom image are also shown in Fig. 3.10. The results show that by 40<sup>th</sup> ML-EM iteration, we were able to reconstruct an artifact free image from each of the two simulated projection sets. As expected, finer details of the phantom can be seen in the simulated reconstruction from the HR MPH collimator. For example, as shown, bone segments in the lower portion of the mouse's rib

age are distinct from each other in the image acquired with the HR MPH collimator, but are partially blurred together in the image acquired using the GP MPH collimator.

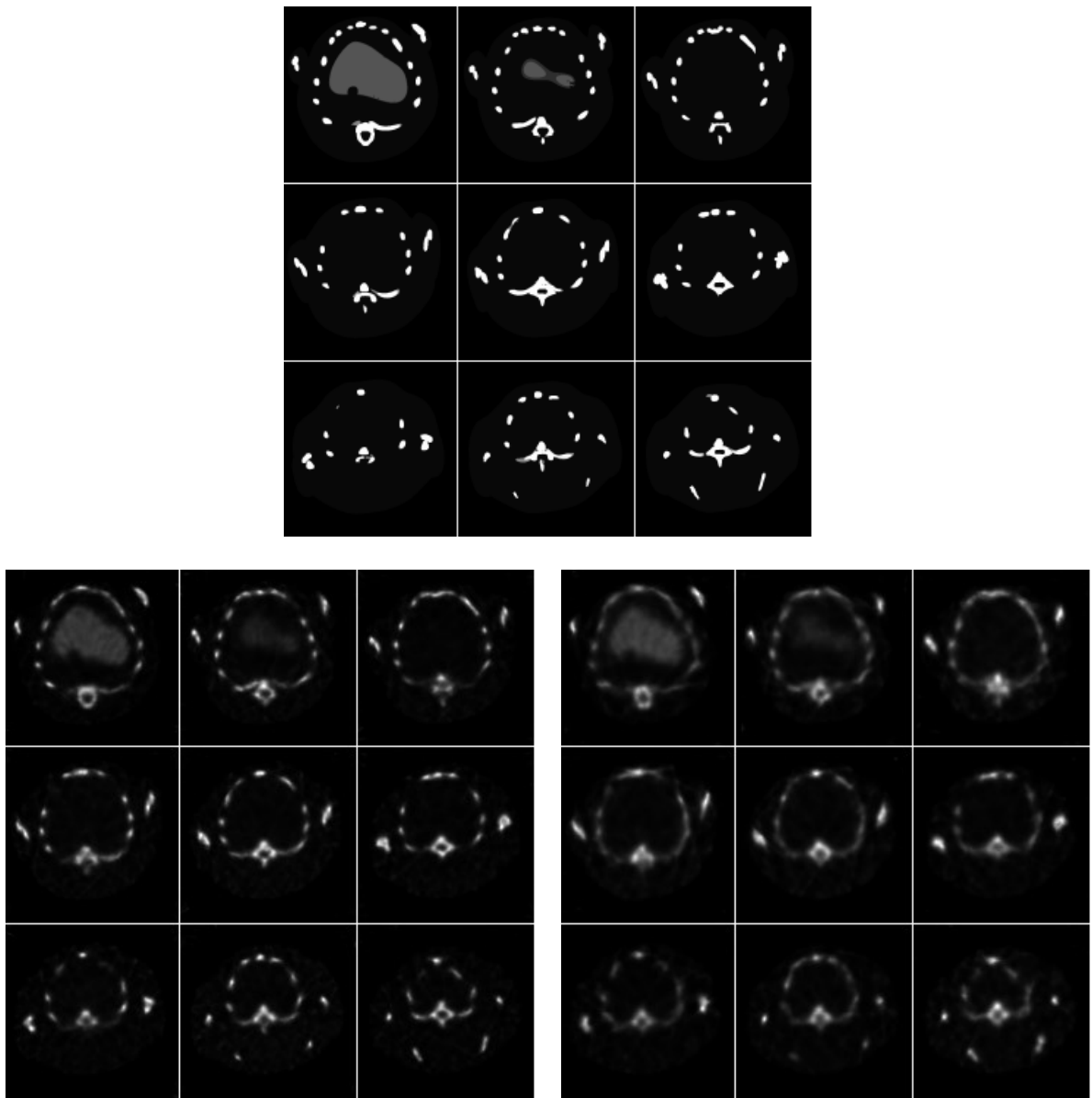


Fig. 3.8. Simulated SPECT Images of the MOBY phantom (top) reconstructed from Analytical Projection Sets Using the HR MPH collimator (lower left) and GP MPH collimator (lower right).

### 3.1.2.3. Simulated Monte Carlo Projection Sets and Reconstructed SPECT Images of Resolution Phantom

As described in Section 2.1.2.2, we used the Monte Carlo program GATE [59] to generate realistic projection sets of the resolution phantom for each of the two collimator designs. We generated one projection set for each of the collimator designs. For the HR MPH collimator, the projection set contained three projection acquisitions. Each projection acquisition was separated by a collimator rotation of  $20^\circ$  between each acquisition. For the GP MPH collimator, the projection set contained a single projection acquisition. Both of the projection sets can be seen in Fig. 3.9.

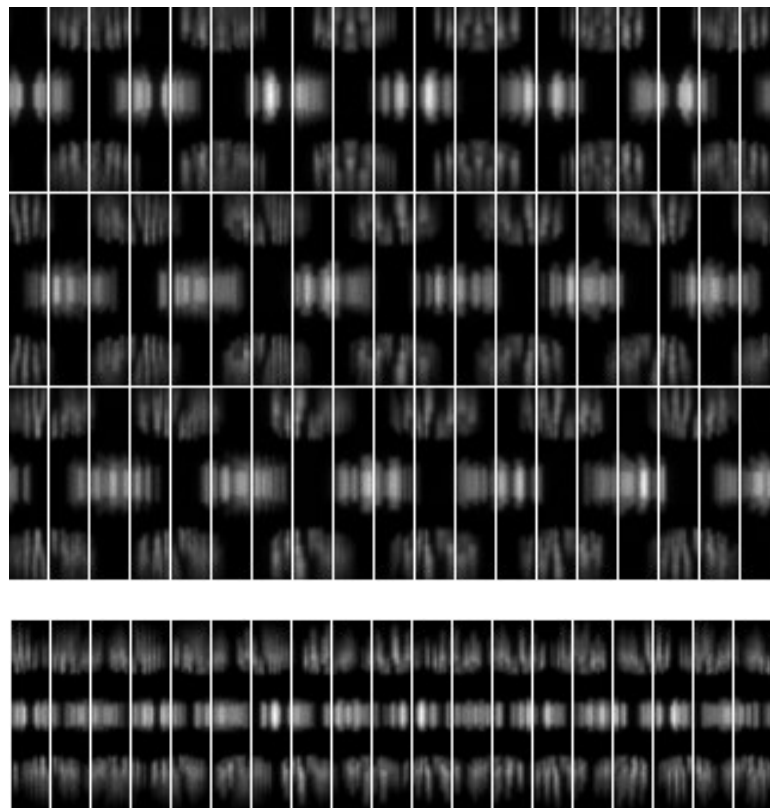


Fig. 3.9. Simulated Monte Carlo Projection Sets of the resolution phantom using the HR MPH collimator (top) and GP MPH collimator (bottom).

SPECT images of the resolution phantom were reconstructed from the projection sets generated with GATE using the same 3D ML-EM method used to reconstruct images from the analytical projections. The results of these simulations are in agreement with the results from the previous analytical simulations. As shown in Fig. 3.10, simulated SPECT images from both collimators have minimal artifacts. These results provide further evidence that three projection acquisitions with the HR MPH collimator, each separated by  $20^\circ$ , and a single projection acquisition with the GP MPH collimator both provide sufficient views for SPECT image reconstruction. Furthermore, for the image obtained with the HR MPH collimator, all phantom segments except for the segment with the 0.75 mm diameter rods were resolvable. In the image obtained with the GP MPH collimator, all segments except for the segments containing the 0.75 mm and the 1 mm diameter rods were resolvable. This demonstrates that both collimators achieve the target system resolution that they had been designed for. Interestingly, the GP MPH collimator can resolve the phantom segment containing rods with 1.35 mm diameter, showing that the image resolution exceeds the image resolution predicted when designing the collimator.

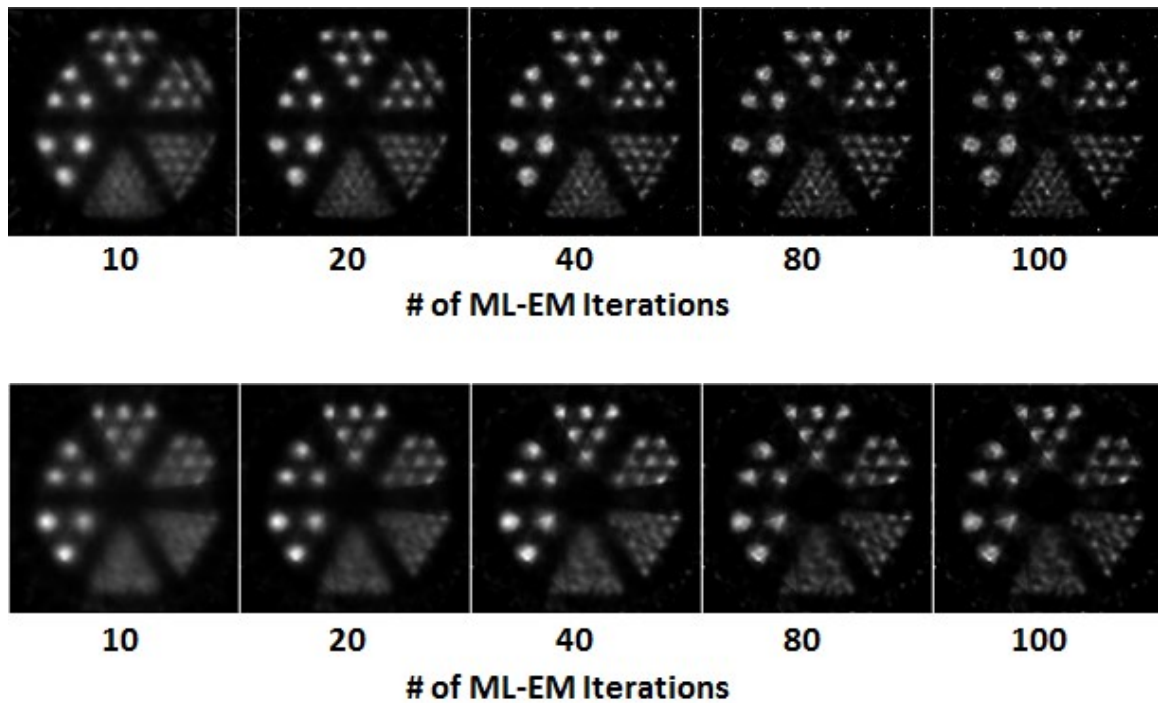


Fig. 3.10. Simulated SPECT Images reconstructed from Monte Carlo Projection Sets Using the HR MPH collimator (top) and GP MPH collimator (bottom).

### 3.1.3. Final Implementation of MR Compatible MPH Collimators

Using the method described in Section 2.1.3, prototypes of both the HR MPH collimator and the GP MPH collimator were implemented. A photograph showing both prototypes are shown in Fig. 3.11. The photograph on the left shows the HR MPH collimator after the pinholes had been inserted into the plastic shell but before it had been filled with tungsten powder and sealed. The photograph on the right shows the completed GP MPH collimator. In this photograph, the MR RF coil designed for simultaneous SPECT/MR acquisition was placed inside the collimator. After both prototype collimators were completed, they were used during experiments used to evaluate both the developed system calibration method as well as experiments to evaluate the performance of the SPECT/MR system.





Fig. 3.11. Prototype of the HR MPH collimator (left) and the GP MPH collimator (right).

## **3.2. Results of Evaluation of SPECT/MR System Calibration and Correction Methods**

The following section will show the results from the experiments described in Section 2.2.3. These experiments were used to evaluate the performance of the system calibration and correction method described in Section 2.2.2.

### **3.2.1. Effect of Nonstandard Detector Pixels on Flood Image Distribution**

The effect of the nonuniform pixels on the distribution of the flood image will now be briefly discussed using a sample data set acquired using the cylindrical shell phantom. Fig. 3.12 shows two histograms of count distributions in the flood image. The first histogram shows the count distributions of the flood image when hypoactive and hyperactive pixels are included, and the second histogram shows the count distribution of the flood image without them. In both cases, each bin shows the number of pixels in the flood image that contain counts within a certain range. For example, in Fig. 3.12a, the first bin shows the number of pixels containing 0 to 4000 counts, the second bin shows the number of pixels containing 4001 to 8000 counts, and so on. It should be noted that prior to generating these histograms, the values of the malfunctioning pixels that count

constantly were set to zero as these pixels are considered to be dead for the purposes of determining which detector pixels are hypo or hyperactive.

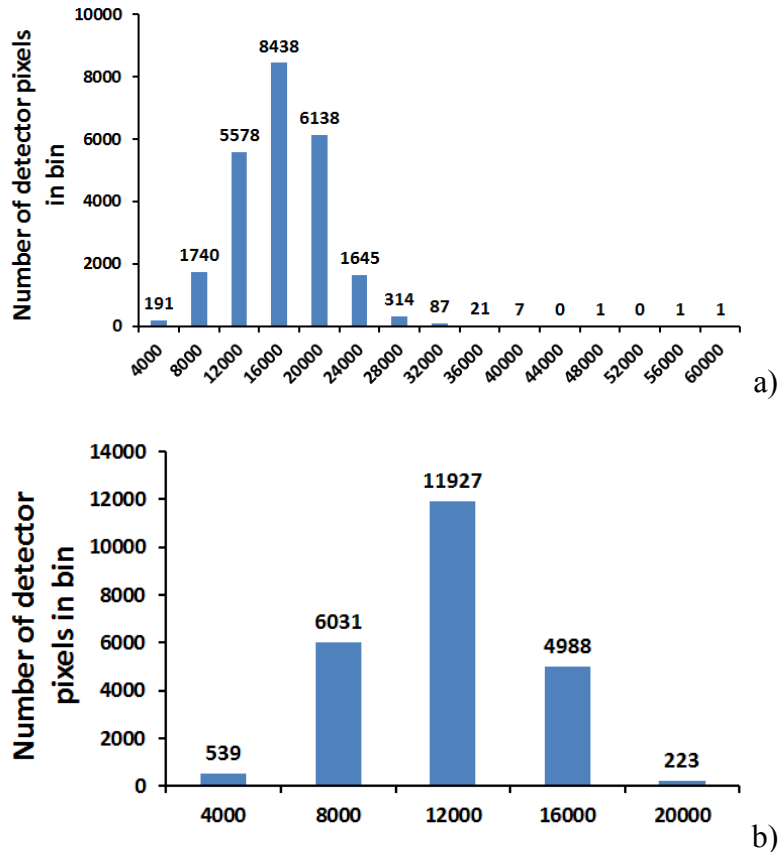


Fig. 3.12. Distribution of counts in an acquired flood image before (a) and after (b) identifying hypoactive and hyperactive detector pixels.

In the sample flood distribution shown in Fig. 3.12a, the mean pixel value is 14216. This means that hypoactive pixels have counts less than or equal to 3554, and hyperactive pixels have counts greater than 24704. As shown in Fig. 3.12a, while most of the pixels in the flood image fall within the range of 3554 to 24704, there are still pixels with higher values, including one within the range of 56000 to 60000 counts. If not corrected for, these pixels will cause high intensity streaking artifacts as well as high intensity spots in any reconstructed SPECT image containing them. The pixels with values above 24704 are considered to be hyperactive. Also notable is that there are 191

pixels in the range 0 to 4000. This bin mostly contains the dead and hypoactive pixels. Without correcting for the hypoactive and dead pixels, low intensity spots will appear in any reconstructed SPECT image containing them.

Fig. 3.12b shows the distribution of the flood image pixel values after removing dead, hypoactive, and hyperactive pixels from the flood distribution. As seen, the distribution no longer has a tail containing a small number of pixels with high count values. Furthermore, the number of pixels included in the bin for pixels with counts between 0 and 4000 has been reduced to 37% of its original value, as most of the pixels in this bin were hypoactive or dead.

### **3.2.2. Results from Evaluation of System Calibration Method with Annular Shell Phantom**

In this experiment, we applied the detector uniformity and correction methods to an independent flood image acquired using the annular shell phantom. The purpose of this experiment was to demonstrate that the developed correction methods could be used to produce a uniform flood image. Although this was a simple experiment, if we were unable to generate a uniform flood image after applying our correction methods, this would demonstrate that the correction methods were not working as expected.

A flood image of a sample module of the detector both before and after the calibration method can be seen in Fig. 3.13. Both images of this module are shown in the same image matrix. As shown, prior to applying the uniformity calibration, there is a significant nonuniformity throughout the module. This nonuniformity is corrected after application of the detector calibration method. Fig. 3.14 shows a profile that was taken across both modules. This profile further demonstrates the improvement in uniformity in

the flood image after application of the uniformity calibration and correction methods. Prior to applying the correction methods, recorded photon count values range between 2318 and 8489 counts. After the methods have been applied, recorded photon count values only range between 5544 and 5943.

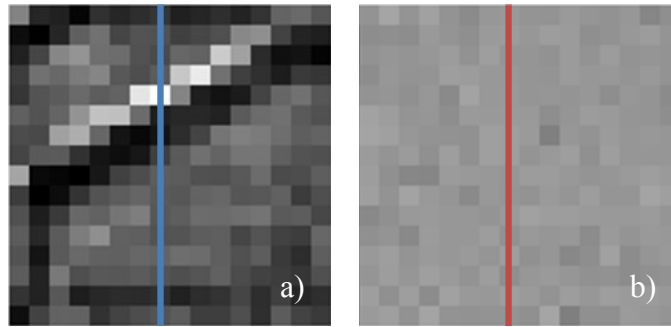


Fig. 3.13. Sample detector module showing flood image data before (a) and after (b) applying detector uniformity calibration and pixel correction. The blue and red lines correspond to the profiles shown in Fig. 3.14.

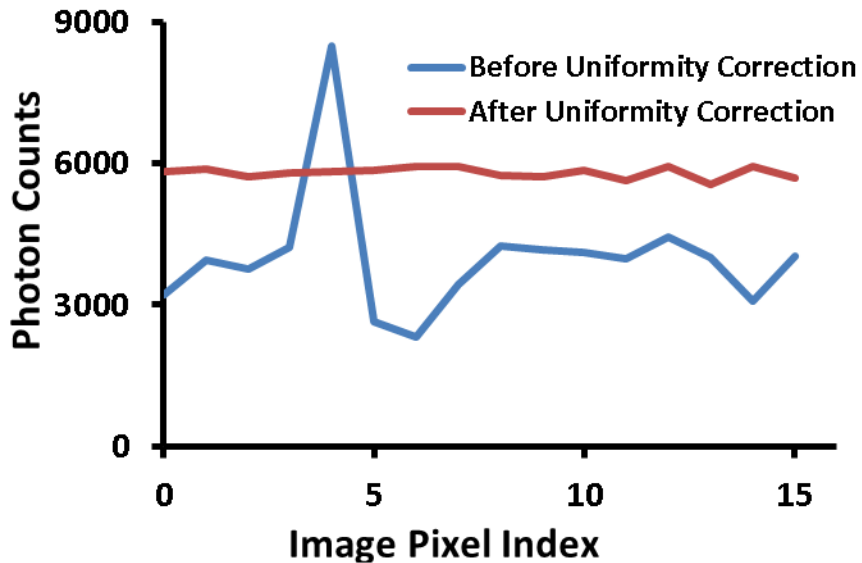


Fig. 3.14. Sample image profile across the same detector module taken before (blue) and after (red) application of uniformity correction method.

To obtain a quantitative measurement of the improvement of the uniformity of the entire detector after the calibration method was applied, the Integral and Differential Uniformity of the detector flood image was calculated using the NEMA standard method [15]. The results of this calculation are seen in Table. 3.3. As shown, there is almost a 10 times improvement in both Integral and Differential Uniformity after the uniformity correction methods are applied. This improvement in the detector uniformity results in significant improvement in image quality of reconstructed SPECT images, as will be shown.

	Before Corrections	After Corrections
Integral Uniformity	0.7606	0.0763
Differential Uniformity	0.6158	0.0647

### **3.2.3. Results from Evaluation of System Calibration Method with Uniform Cylinder Phantom**

To demonstrate that the developed uniformity correction method improves the uniformity of reconstructed SPECT images, as described in Section 2.2.3.2, we acquired projection images of a cylinder filled with Tc-99m solution and then reconstructed SPECT images of the cylinder after applying each stage of the uniformity correction method. Acquired projection images and a 2 mm slice of each reconstructed SPECT image is shown in Fig. 3.15.

Fig. 3.15a shows one of the acquired projection images of the uniform cylinder after the energy calibration method was used to obtain an initial projection image. Fig. 3.15b shows the corresponding reconstructed SPECT image of the cylinder. As shown, there are significant non-uniformities in the projection image due to both variations in

pixel sensitivity as well as hypoactive and hyperactive pixels. Similarly, in the reconstructed SPECT image of the uniform cylinder, there are many hot and cold spots in the reconstructed image, and also several streaking artifacts. Clearly, reconstructing a SPECT image from acquired data without first applying the calibration method will give an image that is not representative of what was actually imaged.

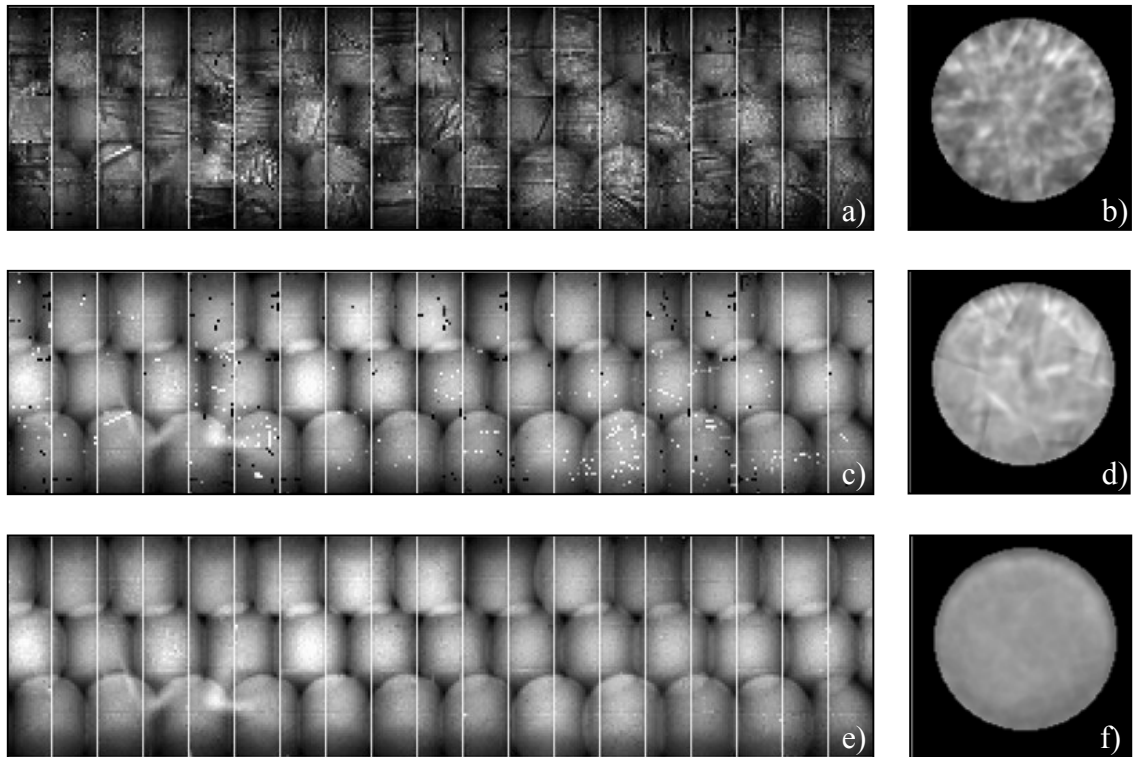


Fig. 3.15. Results of Uniform Cylinder Experiment to Evaluate System Calibration Method. (a) and (b) show projections and reconstructed SPECT of the uniform cylinder phantom before applying uniformity corrections and hypo/hyperactive pixel correction. (c) and (d) show projections and reconstructed SPECT of the uniform cylinder phantom after applying uniformity corrections but before applying hypo/hyperactive pixel correction. (e) and (f) show projections and reconstructed SPECT of the uniform cylinder phantom after applying uniformity corrections and hypo/hyperactive pixel correction.

Fig. 3.15c shows the same acquired projection view as shown in Fig. 3.15a, but after the uniformity correction map has been used to correct for variation in detector pixel sensitivity. The corresponding reconstructed SPECT image is shown in Fig. 3.15d. In this

projection image, most of the non-uniformities have been corrected, but there are still some non-uniformities due to dead, malfunctioning, hypoactive, and hyperactive pixels. These pixels can still be seen in the projection image. Dead, malfunctioning, and hypoactive pixels appear darker in the projection image, while hyperactive pixels appear brighter. An interesting example can be seen in the third detector panel from the left. This detector panel contains the detector module shown in Section 3.2.2. The severe nonuniformity shown earlier in Fig. 3.13 and Fig. 3.14 was due to a set of hyperactive pixels.

While the corresponding reconstructed SPECT image of the uniform cylinder is improved after applying the uniformity correction map, there are still artifacts in the reconstructed image. This is clearly demonstrated in Fig. 3.15d, where there are still several hot or cold spots as well as several streaking artifacts.

Finally, Fig. 3.15e shows the same acquired projection view after using the uniformity correction map and correcting for dead, malfunctioning, hypoactive, and hyperactive pixels. As shown, the pixels in the projection image Fig. 3.15c that were not consistent with their neighboring pixels have now been corrected. Additionally, the reconstructed SPECT image shown in Fig. 3.15f is very uniform. Further analysis of the uniformity of the reconstructed image will be discussed shortly. It should be noted that there was a small leak in the collimator at the time of data acquisition. This leak can be seen in the lower left corner of the projection image in Fig. 3.15e, and gives the appearance of a ‘bulging’ artifact. Our calibration method cannot correct for this leak, but it appears to have had minimal effect on the image quality of our reconstructed image of the cylinder.

To further study the improvement of the uniformity in the projection image and the reconstructed image of the uniform cylinder throughout each of the calibration steps, image profiles across both a single pinhole projection of the uniform cylinder and the horizontal axis of the reconstructed SPECT image of the uniform cylinder were. The profiles were taken before applying any corrections, after applying the uniformity correction, and after applying both the uniformity correction and the pixel correction methods. Both sets of profiles are shown in Fig. 3.16.



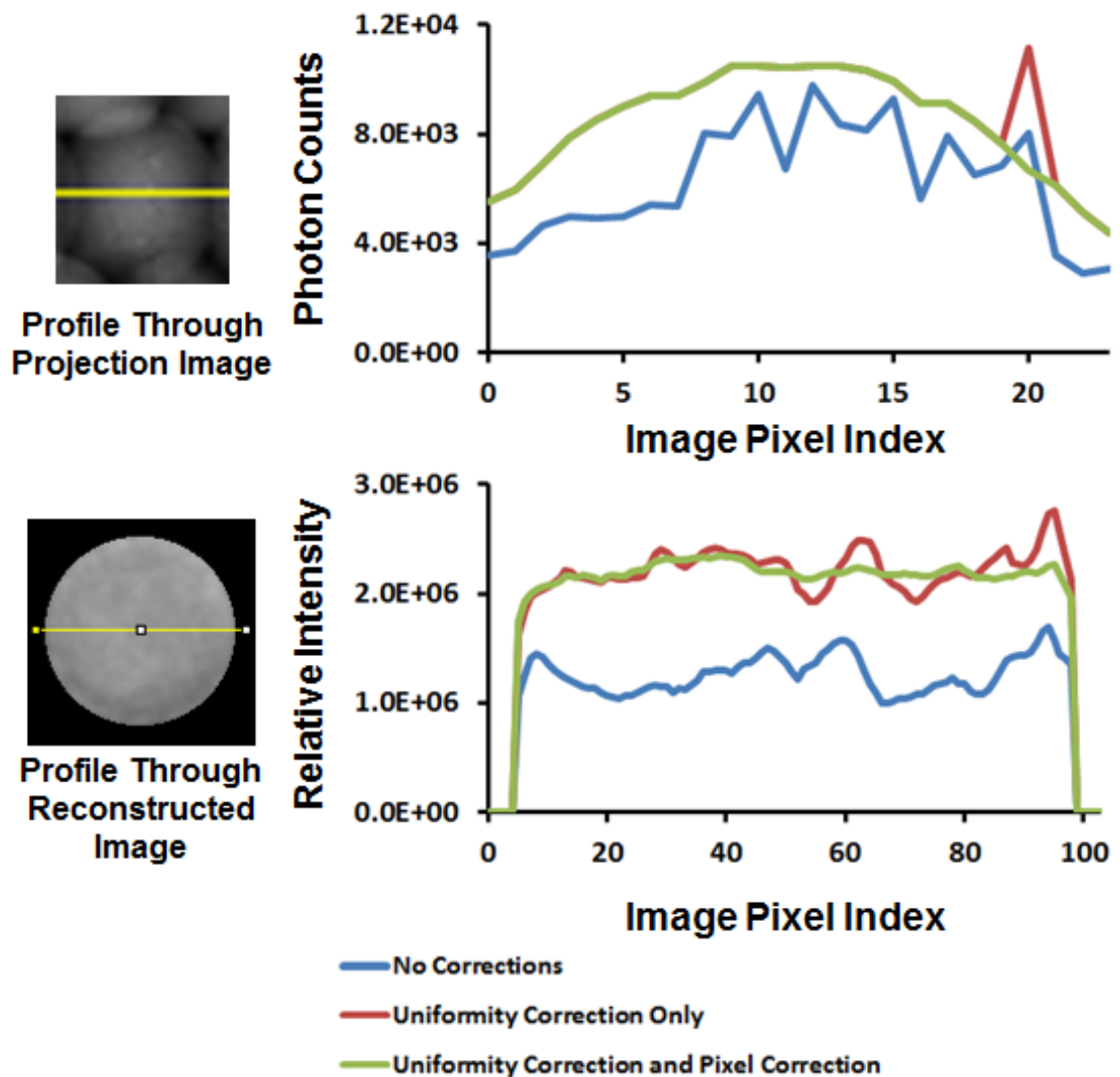


Fig. 3.16. Image profiles taken across projection image and reconstructed SPECT image of uniform cylinder phantom.

For the profile of a projection image of a uniform cylinder, we expected to obtain a curve with a maximum at the center of the projection image and minimum values at the projection edges. This is because, as described in Chapter 1, a pinhole collimator's geometric efficiency is highest at the center of the pinhole, and continuously decreases towards the edge of the pinhole by a factor of  $\cos(\theta)^3$ . However, as seen in Fig. 3.16, before applying any uniformity correction to the projection image, instead, the profile

increases and decreases several times before reaching the edge of the projection because of variations in pixel sensitivity of the detector. After the uniformity correction has been performed, the profile of the projection is closer to what was expected except for the single increase in counts near the edge of the projection image. This spike is due to a hyperactive pixel, and as is shown, after the interpolation to correct for dead, malfunctioning, hypoactive, or hyperactive pixels is performed, the spike is no longer seen in the profile.

In the profile of the reconstructed SPECT image of the uniform cylinder, ideally we would see a flat surface across the entire image profile. However, as seen in Fig. 3.16, without application of either the uniformity correction or the pixel correction, there are many fluctuations in the profile of the uniform cylinder. These fluctuations decrease after application of the pixel correction, but from Fig. 3.16 we see that some still remain. Finally, after application of uniformity correction and pixel correction, fluctuations in the image profile are minimal.

To quantitatively evaluate the uniformity of the calibration method on the uniform cylinder image, the integral uniformity of a central region of the image was calculated. The results are shown in Table 3.4. As shown, the calculated integral uniformity was 3.5 times higher when the corrections were not applied to the acquired projection image.

No Corrections	0.57
Uniformity Correction Only	0.48
All Corrections	0.16

### **3.2.4. Results from Evaluation of System Calibration Method with Resolution Phantom**

To evaluate the effect of the detector uniformity correction method on an image with details, we acquired projection images of the Data Spectrum Ultra Micro Hot Spot Phantom filled with Tc-99m solution and then reconstructed SPECT images of the phantom after applying each stage of the uniformity correction method. Acquired projection images and a 2 mm slice of each reconstructed SPECT image is shown in Fig. 3.17.

Before application of the uniformity correction map, the projection image of the phantom is riddled with non-uniformities. Several horizontal or diagonal streaks can be observed, as seen in Fig. 3.17a. These non-uniformities produce many streaking artifacts in the reconstructed SPECT image of the phantom, as shown in Fig. 3.17b. We can see the 2.4 mm, 2 mm, and 1.7 mm segment in the reconstructed SPECT image of the phantom, but the segments are blurred and the rods are not round shaped, as we would expect.

Once the uniformity correction map has been applied, detector uniformities in the projection image are no longer observed, but dead, hypoactive, and hyperactive pixels are still clearly visible, as shown in Fig. 3.17c. As is shown in Fig. 3.17d, after applying the uniformity correction map to the projection image, there is a significant improvement in the image quality of the reconstructed image of the phantom. The 2.4 mm, 2 mm, 1.7 mm, and 1.35 mm segments of the phantom can now be resolved. Furthermore, there is a clear improvement in the image contrast. However, there are still some streaking artifacts due to hyperactive pixels. Two examples can be seen in Fig. 3.17d, one streaking artifact

can clearly be seen next to the 1.35 mm segment on the rightmost of the image, and another can be seen in one of the rods of the 2.4 mm segment.

The fully corrected projection image is seen in Fig. 3.17e. In this projection, the various rod segments of the phantom can be seen in the projection image, and the malfunctioning pixels no longer have pixel values that are much higher or lower than their neighboring pixels.

The SPECT image reconstructed from the projection set in Fig. 3.17e is shown in Fig. 3.17f. While the improvement in image quality is not as drastic when compared with the change in image quality between images in Fig. 3.17b and Fig. 3.17d, there are still some improvements when comparing the image quality between Fig. 3.17d to Fig. 3.17f. In particular, the streaking artifacts seen in the 1.35 mm segment and the 2.4 mm segment in Fig. 3.17d are no longer present.

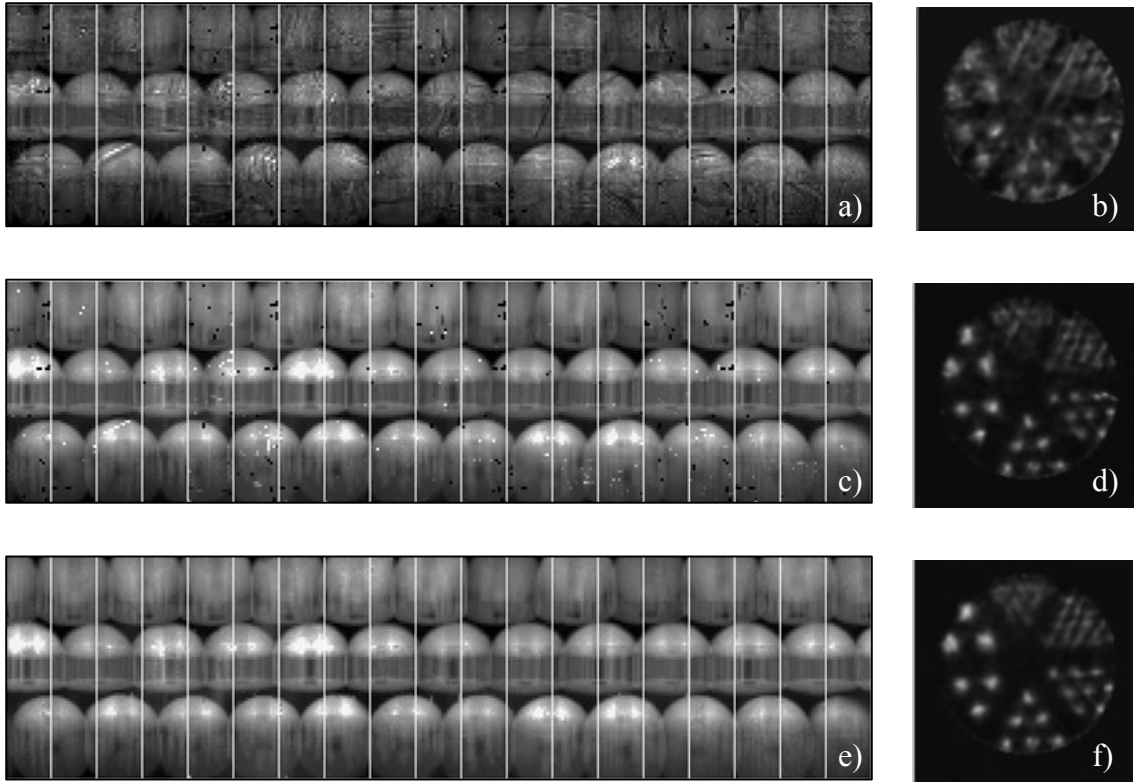


Fig. 3.17. Results of Resolution Phantom Experiment to Evaluate System Calibration Method. (a) and (b) show projections and reconstructed SPECT of the uniform cylinder phantom before applying uniformity corrections and hypo/hyperactive pixel correction. (c) and (d) show projections and reconstructed SPECT of the uniform cylinder phantom after applying uniformity corrections but before applying hypo/hyperactive pixel correction. (e) and (f) show projections and reconstructed SPECT of the uniform cylinder phantom after applying uniformity corrections and hypo/hyperactive pixel correction.

To analyze improvement in image quality Image profiles were taken through each of the resolvable segments of the reconstructed SPECT image of the Ultra Micro Hot Spot Phantom. For each phantom segment, the same profile was taken before any corrections were applied, after uniformity correction was applied, and after uniformity correction and pixel correction were both applied. This allowed us to further study the effect that the calibration method had on the reconstructed images of the Ultra Micro Hot Spot Phantom. These profiles are shown in Fig. 3.18.

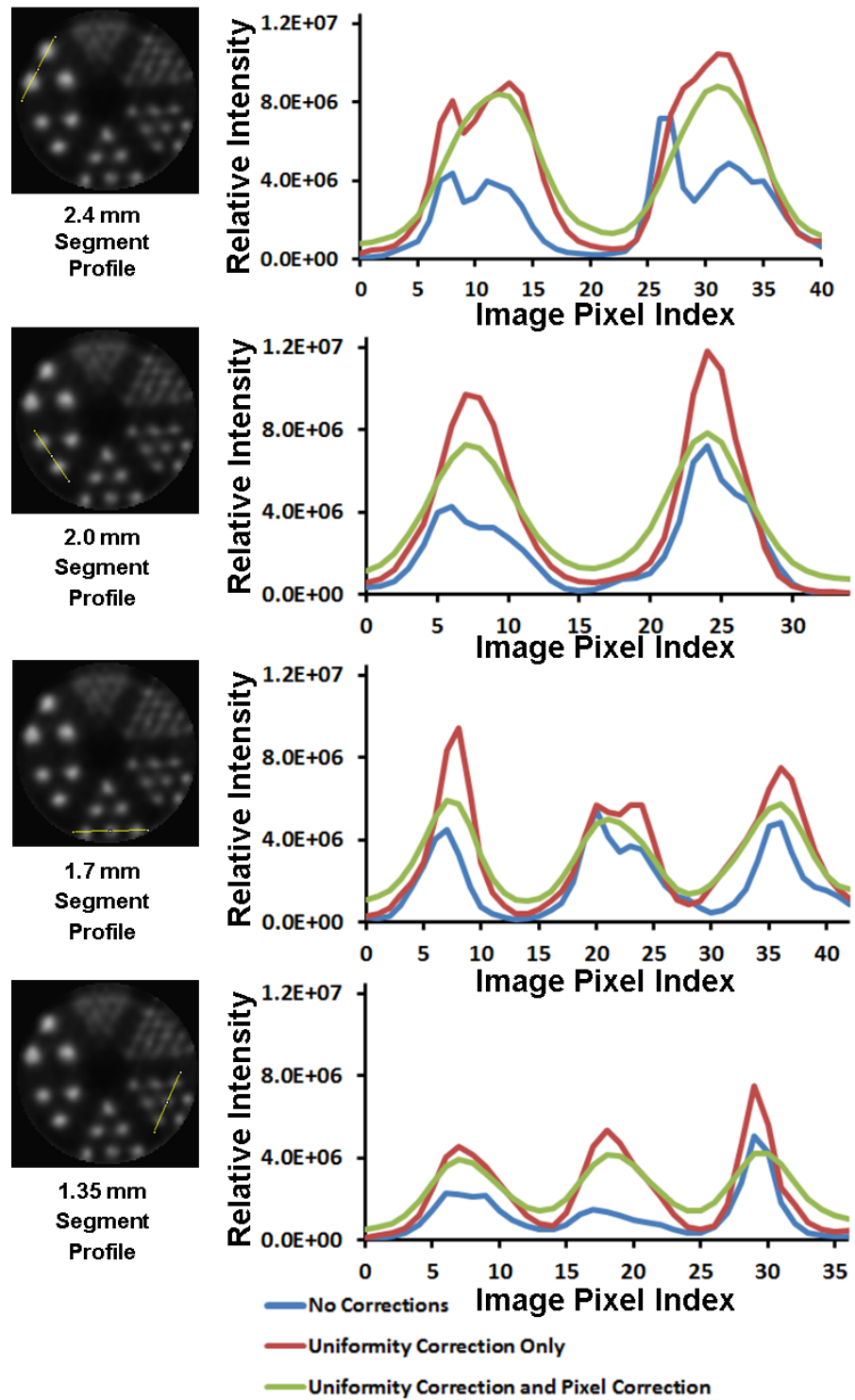


Fig. 3.18. Image Profiles to Study the Effect of the System Calibration Method on reconstructed images of Resolution Phantom.

As shown in Fig. 3.18, prior to applying the detector uniformity correction, the profiles of the rods do not have the appearance we would expect. For example, as seen in the profile of the 2.4 mm segment, for both rods, the pixel with the highest intensity value is not at the center of the rod. Furthermore, both of the rods have a jagged profile when we would expect to see a smooth one. After application of the uniformity correction, one of two rod profiles in the 2.4 mm segment has a single peak, but the other rod profile still has a defect. Finally, after applying both uniformity correction and pixel correction, both of the rod profiles are smooth and have a single peak, as was expected. The profiles of the other three segments of the phantom exhibit similar improvement after application of the calibration methods. It is also worth noting that while the intensity of the peaks increases after the calibration method is applied, the variation in the peaks of the profiles of each of the rods is reduced after both the uniformity correction and the pixel correction methods were applied. The profile of the 1.7 mm rod segment is an especially good example of this. Before correction of hyperactive pixels, the leftmost rod profile has a much higher peak than the other two rod profiles. Rod profiles should have nearly the same peaks because all rods have are filled with solution with the same activity concentration.

We were also able to use data acquired from this experiment to evaluate the developed energy calibration method. As described in Section 2.2.3.3, a projection set from the data acquired using the Ultra Micro Hot Spot phantom was generated without first applying the energy windows stored during the energy calibration process. A sample image reconstructed from this projection set can be seen in Fig. 3.19a, and is compared with an image of the phantom reconstructed from a projection set generated using the

energy calibration method in Fig. 3.19b. Both phantom images are shown in the same image matrix, and it is clear from the images as well as the image profile seen in Fig. 3.20 that after application of the energy calibration, image contrast was significantly improved. Calculations showed that contrast improved by 26%.

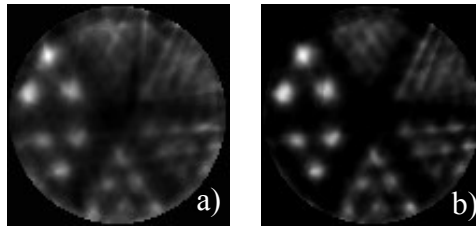


Fig. 3.19. SPECT images of the Ultra Micro Hot Spot phantom reconstructed from projection sets generated without (a) and with (b) energy calibration.

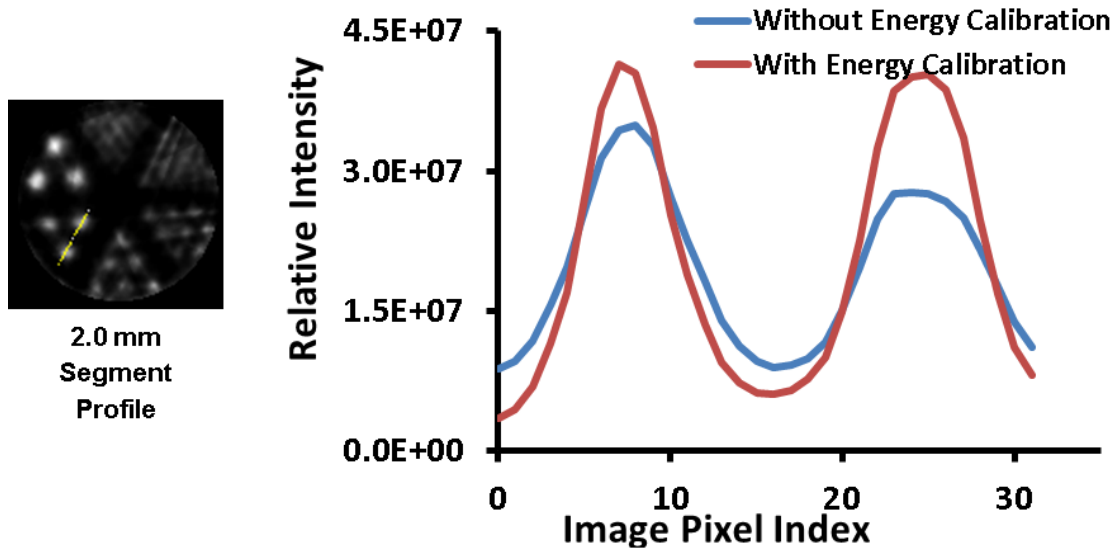


Fig. 3.20. Image profile across the 2.0 mm segment of the SPECT image of the Resolution Phantom with and without application of energy calibration method.



### 3.2.5. Results from Evaluation of System Calibration Method and Lorentz Force Correction Method with Resolution Phantom

To evaluate the Lorentz force correction method, the Ultra Micro Hot Spot phantom was imaged during a simultaneous SPECT/MR imaging experiment. Fig. 3.21 shows an image of the Ultra Micro Hot Spot phantom reconstructed before and after applying the Lorentz force correction method. As is shown, there is a tremendous improvement in image quality between the two images. If the Lorentz force correction method is not applied, the image of the phantom is dominated by artifacts. The 2.4 mm segment of the phantom can barely be seen when the Lorentz force correction method is not applied. However, after application of the correction method, the 2.4 mm, 2.0 mm, 1.7 mm, and 1.35 mm segment of the phantom are clearly resolved. These are the same four segments that are seen in the standalone reconstructed SPECT image of the phantom.

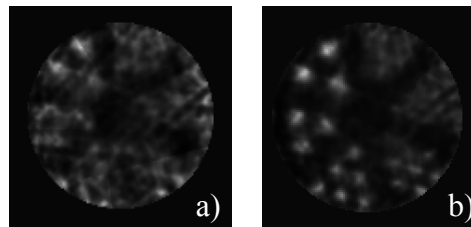


Fig. 3.21. SPECT images of the Ultra Micro Hot Spot phantom reconstructed from projection sets acquired in the presence of a magnetic field without (a) and with (b) correction for drift caused by Lorentz force.

As discussed in Section 2.2.3.4, we further studied the effect of rotationally shifting the pixels of projection images acquired to correct for the Lorentz force drift by

generating a set of shifted projection images. The original projection image was rotationally shifted 3.0 mm in 0.2 mm increments in the direction opposite of the Lorentz force drift. Each shifted projection image was then reconstructed. The results are shown below, in Fig. 3.22. As seen, image quality dramatically improves as the shift of the projection image approaches 1.6 mm. However, as the amount of shift passes 1.6 mm, image quality starts to degrade again. This was expected because, as was discussed earlier in this chapter, the average shift caused by the strength of the magnetic field and the strength of the voltage applied across the CZT modules of the detector was calculated to be approximately 1.6 mm.

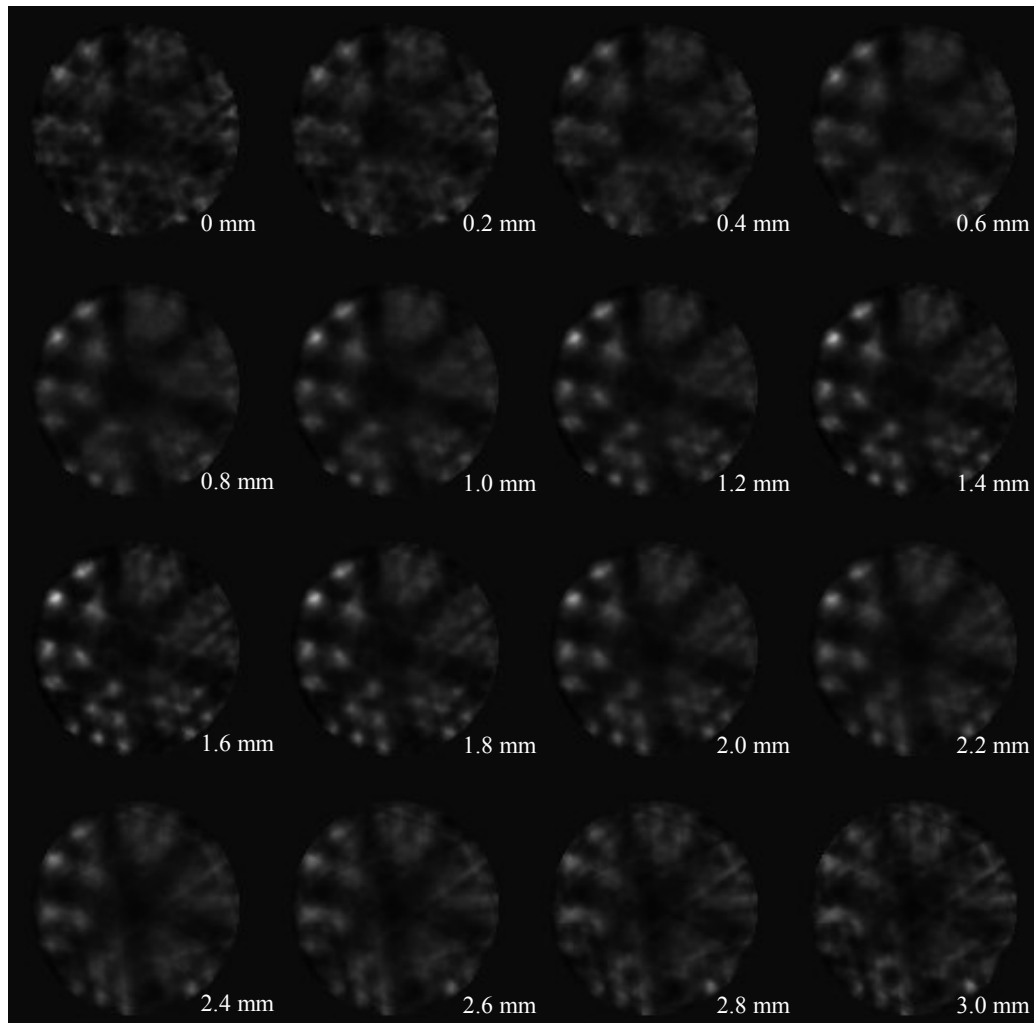


Fig. 3.22. Effect of shifting projection image acquired in the presence of a magnetic field during simultaneous SPECT/MR image acquisition by various amounts.

### 3.3. Results of Experimental Evaluation of SPECT/MR System

In this section, results from the experiments conducted to evaluate the performance of our SPECT/MR system will be discussed. Acquired projection images and reconstructed SPECT images will be shown, along with analysis of the images. Preliminary results from this evaluation were shown in [63].

### **3.3.1. Results of SPECT Imaging Experiment with Resolution Phantom**

This section will show images of the Data Spectrum Ultra Micro Hot Spot Phantom acquired using both the HR MPH collimator and the GP MPH collimator. Reconstructed image quality is evaluated in terms of reconstruction artifacts and image resolution as the number of acquired projection views used in the reconstruction and the number of ML-EM iterations used are varied.

#### **3.3.1.1. Acquired Projection Sets of Resolution Phantom**

As described in Section 2.3.1, eight total projection sets were generated from data acquired during this experiment. Four projection sets contained projection images acquired with the HR MPH collimator, while the other four contained projection images acquired with the GP MPH collimator. All projection sets acquired with the same collimator had nearly the same total number of counts. Furthermore, for projection sets with more than one projection acquisition, each projection acquisition within the projection set had approximately the same number of counts. The number of counts in the projection sets was kept approximately equal to ensure that all reconstructed images have similar noise levels. This meant that any improvement in image quality in images reconstructed from projection sets with more than one projection acquisition was due to the additional projection acquisitions rather than the additional counts provided by the projection acquisition. Table 3.5 shows the collimator used for each projection set, the number of projection acquisitions in each projection set, the amount of angular rotation between projection sets, the total number of counts in each projection set, and the average number of counts in each projection acquisition of projection sets with more than one projection acquisitions.

Table 3.5: Parameters for Experimentally Acquired Projection Sets of Resolution Phantom for HR MPH collimator (HRC) and GP MPH collimator (GPC)				
Projection Set Name	# of Projection Acquisitions	Angle Between Projection Acquisitions	Total Number of Counts in Projection Set	Average Number of Counts in Each Projection Acquisition
HRC Projection Set 1	1	N/A	$1.11 \cdot 10^8$	n/a
HRC Projection Set 2	2	$30^\circ$	$1.11 \cdot 10^8$	$5.55 \cdot 10^7$
HRC Projection Set 3	3	$20^\circ$	$1.10 \cdot 10^8$	$3.66 \cdot 10^7$
HRC Projection Set 4	6	$10^\circ$	$1.11 \cdot 10^8$	$1.85 \cdot 10^7$
GPC Projection Set 1	1	N/A	$1.63 \cdot 10^8$	n/a
GPC Projection Set 2	2	$15^\circ$	$1.58 \cdot 10^8$	$7.9 \cdot 10^7$
GPC Projection Set 3	3	$10^\circ$	$1.55 \cdot 10^8$	$5.16 \cdot 10^7$
GPC Projection Set 4	6	$5^\circ$	$1.76 \cdot 10^8$	$2.93 \cdot 10^7$

The projection sets for each collimator that contained a single projection acquisition are shown in Fig. 3.23.

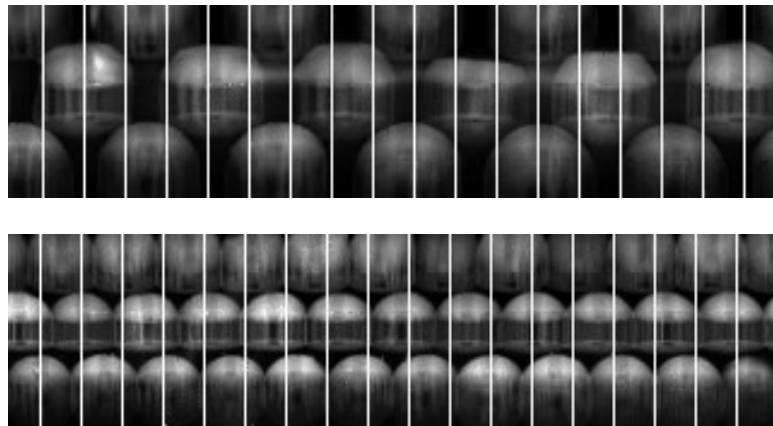


Fig. 3.23. Sample experimental projection acquisitions of the Ultra Micro Hot Spot Phantom using the HR MPH collimator (top) and GP MPH collimator (bottom)

### 3.3.1.2. Reconstructed SPECT Images of Resolution Phantom

Sample SPECT images of the phantom reconstructed using each of the four projection acquired using the HR MPH collimator at varying ML-EM iterations are shown in Fig. 3.24. As expected from the simulation results, images reconstructed using projection sets containing one or two projection acquisitions have reconstruction artifacts. More views are needed to obtain an artifact free reconstructed SPECT image of the

phantom. The results show that a projection set containing three projection acquisitions is sufficient to reconstruct a SPECT image with minimal artifacts. As expected, five of the six collimator segments can be resolved when sufficient iterations are used, showing that the collimator can reach its designed target system resolution of 1 mm. To successfully resolve the phantom segment containing the 1 mm diameter rods, at least 40 ML-EM iterations were needed.

When the projection set containing six views is used to reconstruct an image of the phantom, image quality continues to improve. Most notably, in the image reconstructed using six views, the smallest segment of the phantom can be partially resolved. Rods closer to the outer edge of the phantom can be distinguished from each other. However, rods closer to the center of the phantom are still blurred together. As the smallest segment of the phantom contains rods with 0.75 mm in diameter, this result suggests that the HR MPH collimator can be used to obtain images with submillimeter resolution, if a sufficient number of projection acquisitions are used in the reconstruction. This result is due to the model of the collimator detector response that was included in the ML-EM reconstruction software.

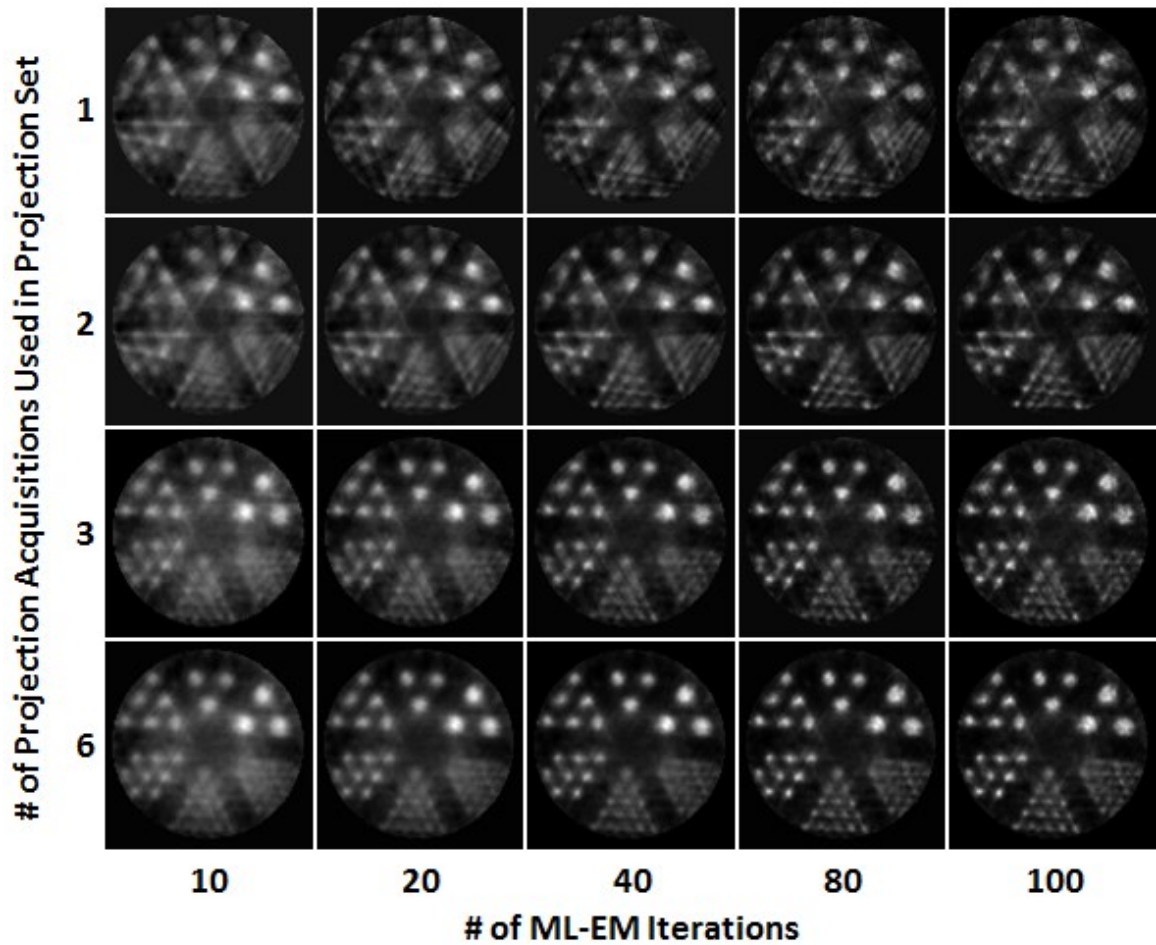


Fig. 3.24. Reconstructed images of the Ultra Micro Hot Spot Phantom acquired using the HR MPH collimator with different number of projection acquisitions and ML-EM iterations.

Sample SPECT images of the phantom reconstructed using each of the four projection sets acquired using the GP MPH collimator at varying ML-EM iterations are shown in Fig. 3.25. The results show that one projection acquisition is sufficient to obtain a reconstructed SPECT image when using the GP MPH collimator. Furthermore, as shown, four of the six segments of the phantom can be resolved. Even though the GP MPH collimator was designed with target system resolution of 1.5 mm, the rods with diameter of 1.35 mm can be resolved when at least 80 ML-EM iterations are used. The target system resolution is exceeded because of the collimator detector response model

included in the ML-EM reconstruction software. Although the reconstructed image's resolution does not improve when projection sets with more projection acquisitions are used to reconstruct images of the phantom, image quality improves as the number of projection acquisition increases. Specifically, as more projection acquisitions are used in the reconstruction, the phantom rods become rounder.

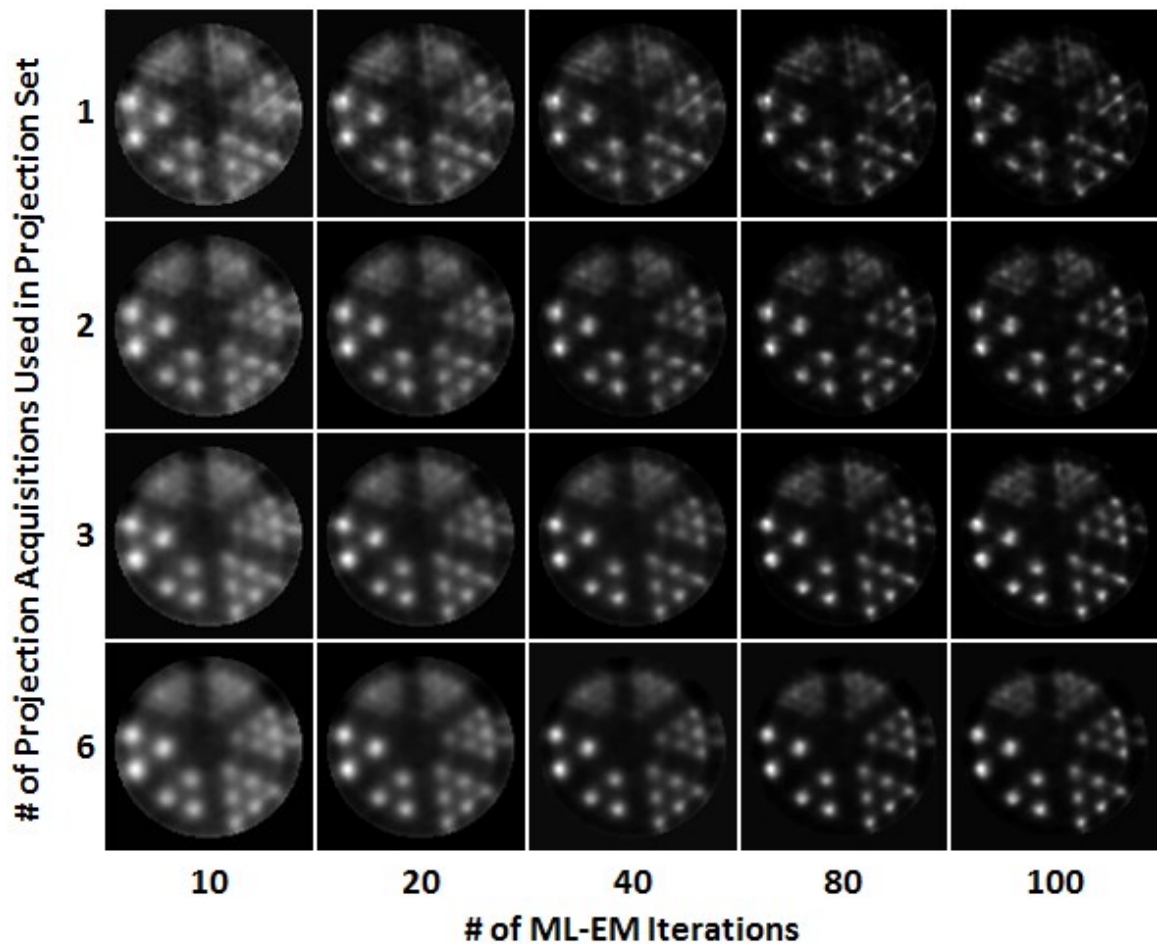


Fig. 3.25. Reconstructed images of the Ultra Micro Hot Spot Phantom acquired using the GP MPH collimator with different number of projection acquisitions and ML-EM iterations.



### 3.3.1.3. Analysis of Resolution Phantom SPECT Images

As mentioned in Section 2.3.1, to evaluate the accuracy of the reconstructed image of the phantom, the center to center distance between adjacent rods in each segment was measured. This analysis was performed using images reconstructed using all six projection acquisitions from each of the phantom experiments. For each phantom image, distance between adjacent rods in each completely resolved phantom segment was measured. Therefore, ROIs were drawn around each rod in the 2.4 mm, 2 mm, 1.7 mm, 1.35 mm, and 1 mm phantom segment for the image acquired with the HR MPH collimator and ROIs were drawn around each rod in the 2.4 mm, 2 mm, 1.7 mm, and 1.35 mm segment for the image acquired with the GP MPH collimator. Then, the distance between the center of mass of each adjacent rod in each segment was calculated. All of the calculated distances for each segment for each image were then averaged together. The results of the calculations are shown in Table 3.6. As shown, the percent error when comparing the expected distance to the reconstructed image's distance was minimal. This analysis demonstrates that the SPECT/MR system is capable of acquiring accurate images for objects held within the system's CVOV for both collimators.

	HR MPH collimator Measurements (mm)	Percent Error from HR MPH collimator Measurements	GP MPH collimator Measurements (mm)	Percent Error from GP MPH collimator Measurements
2.4 mm segment	4.49	6.39%	4.45	7.22%
2 mm segment	3.85	3.53%	3.83	4.22%
1.7 mm segment	3.17	6.55%	3.19	5.96%
1.35 mm segment	2.56	4.83%	2.66	1.34%
1 mm segment	1.89	5.21%	N/A	N/A

### **3.3.2. Results of SPECT Imaging Experiment of Mouse Skull with Tc-99m MDP**

This section will show images of a mouse skull using Tc-99m MDP that were acquired using both the HR MPH collimator and the GP MPH collimator. Reconstructed image quality is evaluated in terms of reconstruction artifacts and reconstructed image resolution.

#### **3.3.2.1. Acquired Projection Sets of Mouse Skull Acquired with Tc-99m MDP**

After following the procedure described in Section 2.3.2, two projection sets containing data from the experiment were generated. The first projection set contained data acquired using the HR MPH collimator. This projection set contained three projection acquisitions, with 20° collimator rotation between each projection acquisition. The second projection set contained data acquired using the GP MPH collimator. This projection set contained two projection acquisitions, with 15° collimator rotation between acquisitions. Sample projection acquisitions from each of the two collimators can be seen in Fig. 3.26.

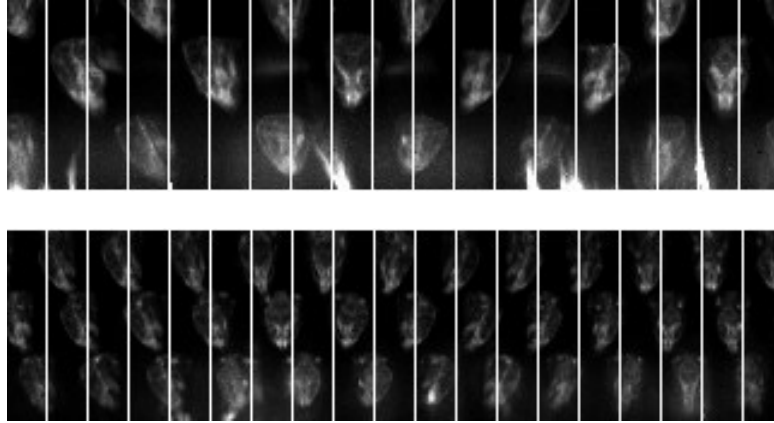


Fig. 3.26. Sample experimental projection acquisitions of a mouse's skull obtained using Tc-99m MDP Bone scan Study using the (top) HR MPH collimator and (bottom) GP MPH collimator

### **3.3.2.2. Reconstructed SPECT Images of Mouse Skull Acquired with Tc-99m MDP**

Fig. 3.27 shows selected slices from the SPECT image acquired using both the HR MPH collimator and the GP MPH collimator. Both images have been reconstructed using 40 ML-EM iterations. In the images shown, every fourth slice is displayed, meaning that slices are separated by 1 mm. Regions in the images outside of the mouse's skull have been set to a low image intensity value in order to improve the contrast in the image between different parts of the skull. The reconstructed SPECT images seen in Fig. 3.27 demonstrate the high image quality that the SPECT/MR insert is capable of achieving when acquiring preclinical images. As was expected, sharper image details can be seen in the image acquired with the HR MPH collimator. In both images, we did not observe any artifacts due to reconstruction.

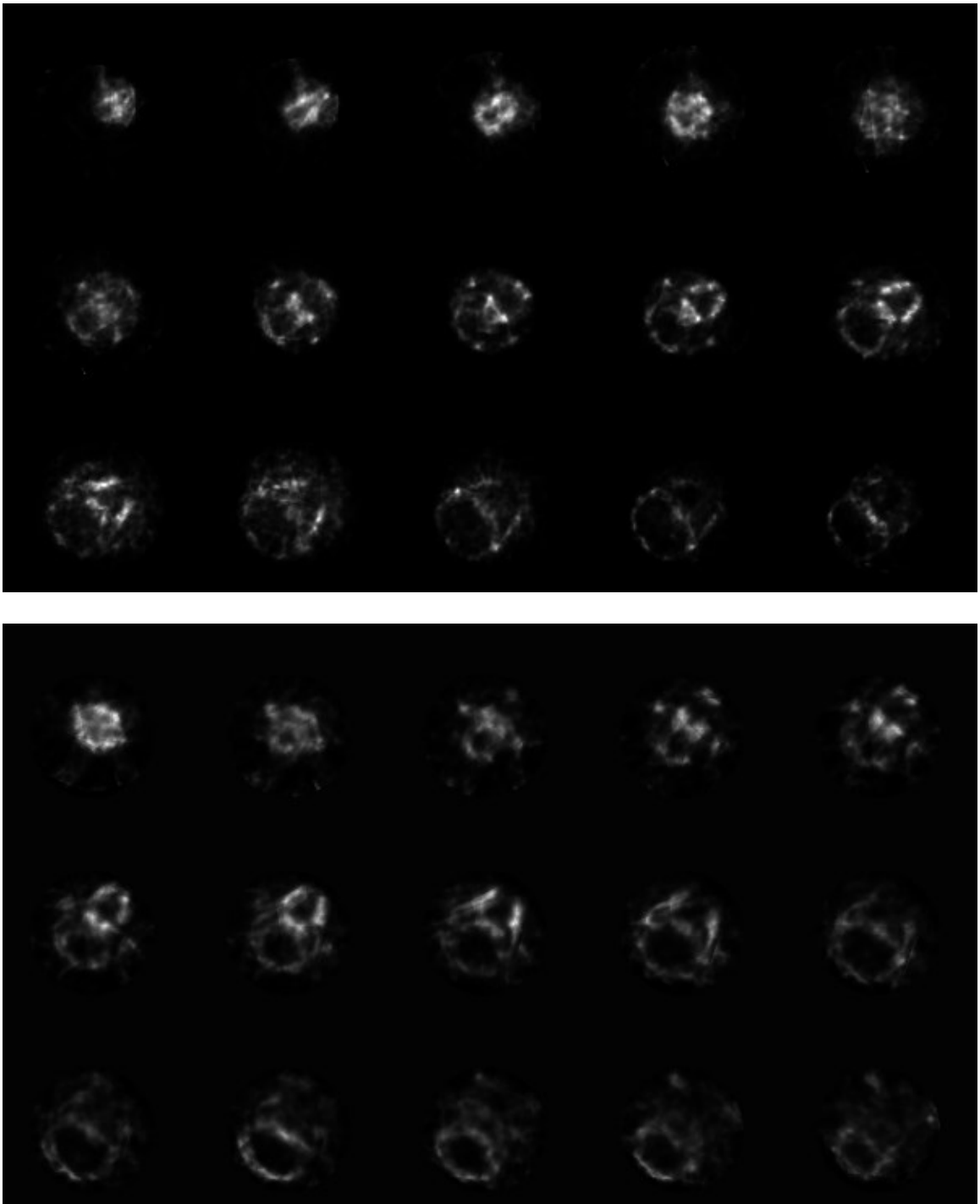


Fig. 3.27. Reconstructed SPECT Images of mouse skull obtained using Tc-99m MDP using the (top) HR MPH collimator and (bottom) GP MPH collimator

### **3.3.3. Results of SPECT Imaging Experiment of Mouse Kidneys Imaged with Gadolinium Nanoparticles Labeled with Tc-99m**

This section will show images of mouse kidneys acquired the GP MPH collimator acquired using Gadolinium Nanoparticles Labeled with Tc-99m. Reconstructed image quality is evaluated in terms of reconstruction artifacts and reconstructed image resolution.

#### **3.3.3.1. Acquired Projection Set of Mouse Kidneys Acquired with Gadolinium Nanoparticles Labeled with Tc-99m**

Data acquired during this experiment was used to generate a projection set containing a single projection acquisition. The final projection set is shown in Fig. 3.28. As was expected, because the gadolinium nanoparticles contained DTPA, there was significant uptake of the gadolinium nanoparticles in the mouse's kidneys.

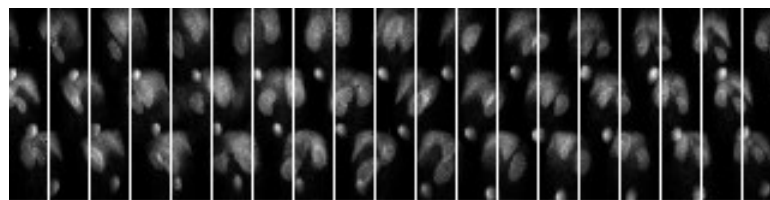


Fig. 3.28. Sample experimental projection acquisition of a mouse kidney acquired using gadolinium nanoparticles labeled with Tc-99m

#### **3.3.3.2. Reconstructed SPECT images of Mouse Kidneys Acquired with Gadolinium Nanoparticles Labeled with Tc-99m**

Reconstructed SPECT images of the mouse kidney acquired using the gadolinium nanoparticles are seen in Fig. 3.29. From this experiment, several interesting aspects of the SPECT/MR system were demonstrated. First, as was expected, an image of a mouse's kidneys with high image quality can be obtained using the GP MPH collimator when

only one collimator position was used during data acquisition. Secondly, this experiment demonstrates the value of the high geometric efficiency of the GP MPH collimator. Even though data was only acquired for 5 minutes, and only ~5 mCi of activity was injected into the mouse, we were still able to use the GP MPH collimator to obtain a high quality SPECT image with low noise. Most importantly, with this experiment we demonstrated that we could use the nanoparticles to obtain preclinical images, and that the nanoparticles would be a viable agent for simultaneous SPECT-MR imaging experiments. Furthermore, this experiment demonstrated that we can use the GP MPH collimator to obtain a high quality image of a mouse kidney without rotation of the collimator.

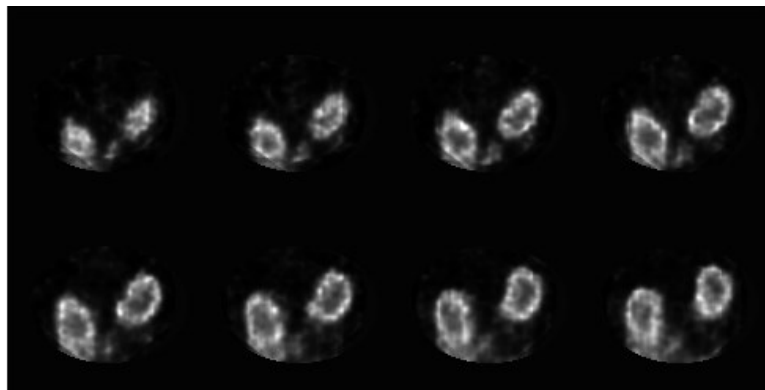


Fig. 3.29. Reconstructed SPECT Images of mouse kidney obtained using gadolinium nanoparticles labeled with Tc-99m

### **3.3.4. Results of Simultaneous SPECT/MR Imaging Experiment with Resolution Phantom**

This section will show SPECT images of the Data Spectrum Ultra Micro Hot Spot Phantom acquired using the GP MPH collimator while simultaneously acquiring an MR image of the phantom. Reconstructed image quality is evaluated in terms of reconstruction artifacts and image resolution as the number of acquired projection views used in the reconstruction and the number of ML-EM iterations used are varied.

Furthermore, image quality of the image acquired during simultaneous SPECT/MR acquisition is compared with the image quality of an image of the phantom obtained during standalone SPECT acquisition.

#### **3.3.4.1. Acquired Projection Sets of Resolution Phantom with Tc-99m Obtained During Simultaneous SPECT/MR Experiment**

After following the procedure described in Section 2.3.4, a projection set containing a single projection acquisition of the resolution phantom was obtained. The projection set is shown below in Fig. 3.28. It is noted that this projection image is noisier than the projection image of the resolution phantom obtained with the GP MPH collimator shown earlier in Fig. 3.30. This is due to the fact that a shorter acquisition time was used to acquire the projection image shown below.

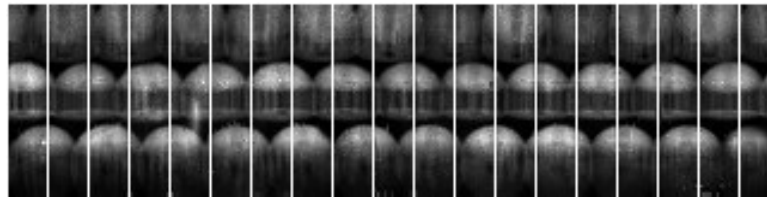


Fig. 3.30. Projection Image of Resolution Phantom Acquired During Simultaneous SPECT/MR Study

#### **3.3.4.2. Reconstructed SPECT Image of Resolution Phantom with Tc-99m Obtained During Simultaneous SPECT/MR Experiment**

SPECT images of the resolution phantom reconstructed from the projection set seen in Fig. 3.30 are shown below in Fig. 3.31. To reduce noise in the reconstructed phantom image, slices in the axial direction were summed together. The slice thickness in each of the reconstructed images shown is 4 mm. Finally, to maximize the contrast of the rod image, region of the image outside of the phantom rods was masked with a low pixel

intensity value. As shown, all of the segments in the phantom except for the 1 mm and the 0.75 mm segments can be resolved. This was expected, as both the simulation results as well as the standalone SPECT experimental results discussed earlier gave the same result.

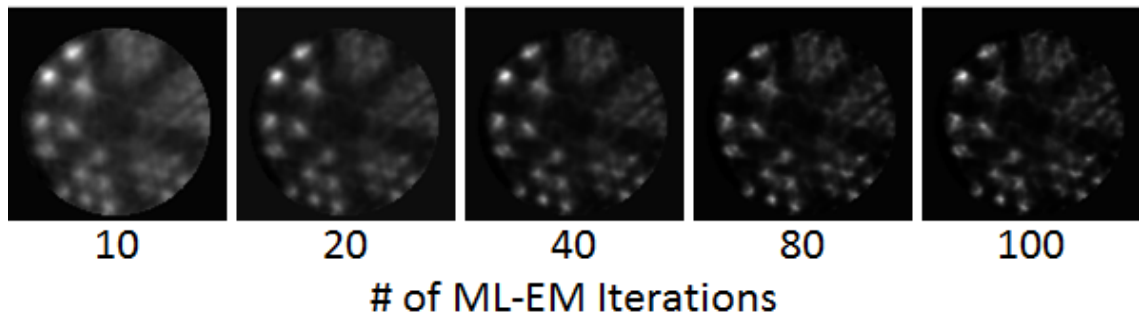


Fig. 3.31. Reconstructed SPECT images of Ultra Micro Hot Spot Phantom acquired during simultaneous SPECT/MR study

### **3.3.4.3. Analysis of SPECT and MR Images of Resolution Phantom with Tc-99m Obtained During Simultaneous SPECT/MR Experiment**

The SPECT image of the phantom acquired during simultaneous SPECT/MR acquisition was compared with a SPECT image of the phantom obtained during a standalone SPECT experiment. Even though we were able to obtain a SPECT image of the phantom during simultaneous SPECT/MR acquisition, as shown in Fig. 3.31, it was important to determine whether the presence of the MR system affected the performance of the SPECT/MR system.

To make a fair comparison, we generated a projection set containing a single projection acquisition with data acquired with the GP MPH collimator during a standalone SPECT experiment. Both projection sets had approximately the same number of counts to ensure that the results had similar noise properties. The two reconstructed SPECT images are shown below in Fig. 3.32.



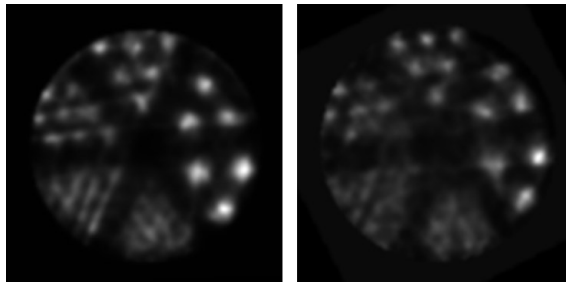


Fig. 3.32. Reconstructed SPECT images of Resolution Phantom acquired during (left) standalone SPECT acquisition and during (right) simultaneous SPECT/MR image acquisition

From Fig. 3.32, it is clear that the SPECT image acquired during simultaneous SPECT/MR acquisition has comparable image quality to the image acquired during standalone SPECT acquisition. Although there are some minor differences in the shape of the rods of the two images, this could be attributed to noise or the fact that both of the images were reconstructed using a single projection acquisition. As was shown in Section 3.3.1.2, the shape of the rods in the reconstructed image improves when more projection acquisitions are used.

To further compare the two SPECT images, the distance from adjacent rods in the 2.4 mm, 2 mm, 1.7 mm, and 1.35 mm segments were measured in both images using the same procedure discussed earlier in Section 3.3.1.3. Table 3.7 shows the average distance between adjacent rods for both the standalone SPECT image and the SPECT image that was acquired during simultaneous SPECT/MR acquisition. As shown, there is very little difference in the average rod distances of the SPECT image acquired during standalone SPECT acquisition and during simultaneous SPECT/MR acquisition, showing that there is minimal, if any, distortion in the SPECT image acquired during while an MR image was acquired simultaneously.

Table 3.7 Average Distance Between Rods in Image of Resolution Phantom and Percent Error in SPECT images acquired standalone SPECT and during simultaneous SPECT/MR acquisition				
	Standalone SPECT Acquisition (mm)	Percent Error for Standalone SPECT Acquisition	Simultaneous SPECT/MR Acquisition (mm)	Percent Error for Simultaneous SPECT/MR Acquisition
2.4 mm segment	4.64	3.14%	4.77	0.54%
2 mm segment	4.16	4.07%	3.90	2.50%
1.7 mm segment	3.44	1.34%	3.23	4.99%
1.35 mm segment	2.83	4.88%	2.78	3.09%

It was also important to evaluate the MR image that was acquired during this imaging experiment. In order to determine whether the SPECT and MR images acquired simultaneously were in good agreement with each other, the SPECT image was registered with the MR image using a 2D rigid body transform. The two images were then fused together. Fig. 3.33 shows the SPECT and MR images obtained during simultaneous SPECT/MR acquisition as well as the registered and fused SPECT and MR image. As shown, the SPECT and MR image are in good agreement with each other.

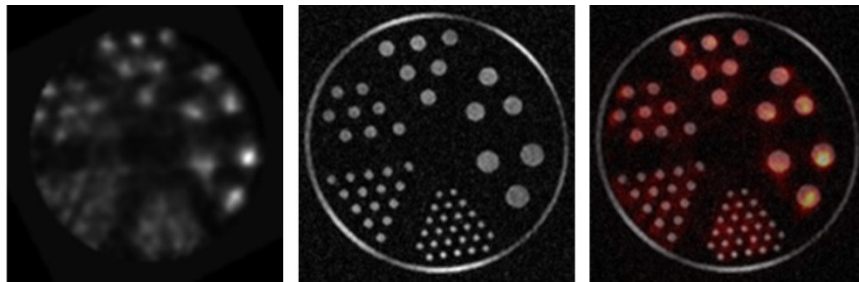


Fig. 3.33. Simultaneously Acquired SPECT and MR Images of the Ultra Micro Hot Spot Phantom. SPECT Image (left), MR Image (center), Fused Image (right)

To further determine whether there was any distortion in the MR image due to the presence of the SPECT/MR system, the distance between adjacent rods in the MR image for all six of the phantom segments were measured using the same method described in Section 2.3.1. As seen in Table 3.8, in all six segments of the phantom image acquired by

the MR system, the average distance is very close to the true phantom rod distance. This suggests that there is minimal, if any, geometric distortion in the MR image despite the fact it was acquired simultaneously with a SPECT image.

Table 3.8. Average Distance Between Rods in Image of Ultra Micro Hot Spot Phantom and Percent Error in MR image during simultaneous SPECT/MR acquisition		
	Simultaneous SPECT/MR Acquisition (mm)	Percent Error for Simultaneous SPECT/MR Acquisition
2.4 mm segment	4.73	1.39%
2 mm segment	3.91	2.04%
1.7 mm segment	3.32	2.1%
1.35 mm segment	2.71	0.58%
1 mm segment	2.00	~0%
0.75 mm segment	1.49	0.16%

### **3.3.5. Results of Simultaneous SPECT/MR Imaging Experiment of Mouse Kidneys with Tc-99m MAG3**

This section will show acquired projection images and reconstructed SPECT images of mouse kidneys obtained using Tc-99m MAG3 while simultaneously acquiring a set of dynamic MR images of the mouse kidneys. Both static and dynamic SPECT and MR images will be shown, as well as a time activity curve generated from the dynamic SPECT image.

#### **3.3.5.1. Acquired Projection Sets of Mouse Kidneys Imaged with Tc-99m MAG3 Obtained During Simultaneous SPECT/MR Experiment**

As described in Section 2.3.5, the static projection set generated from data acquired during this experiment contains a single a single projection acquisition that uses all of the SPECT data acquired during the imaging experiment. This projection

acquisition does not show the initial uptake and later washout of the Tc-99m MAG3 into the mouse's kidney. Instead however, the static projection acquisition allows us to obtain a clear image of the mouse's kidney similar to the image shown earlier in Section 3.3.3. The static projection image is shown below in Fig. 3.34.

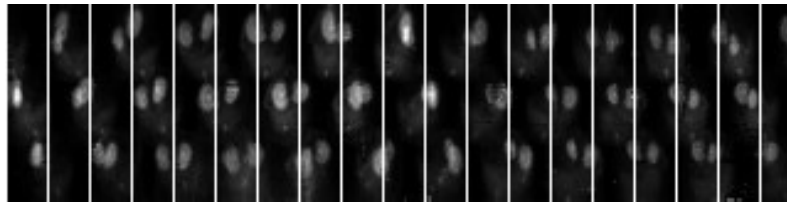


Fig. 3.34. Static projection image of mouse kidney obtained using Tc-99m MAG3 during simultaneous SPECT/MR imaging experiment

In addition to the static projection set, we also generated a dynamic projection set. As described in Section 2.3.5, each projection acquisition in the dynamic set represented 10 seconds of acquired data. Because SPECT data was acquired for 30 minutes, there were a total of 180 projection acquisitions in the dynamic projection set. The same portion of the first 10 projection acquisitions, corresponding to the first 100 seconds of data acquisition can be seen in Fig. 3.35. As shown, initially there is no discernible projection image. This is because SPECT acquisition was started before the mouse was injected with Tc-99m MAG3. However, by Frame 5, projection images of the kidney start to become visible, and the kidneys are clearly seen in Frame 8-10. The projection images in Fig. 3.35 are much noisier than the projection image shown above in Fig. 3.33 because each projection set only contains 10 seconds of acquired data. Nevertheless, as will be shown in Section 3.3.5.2, they can still be used to reconstruct a SPECT image of the mouse's kidney.

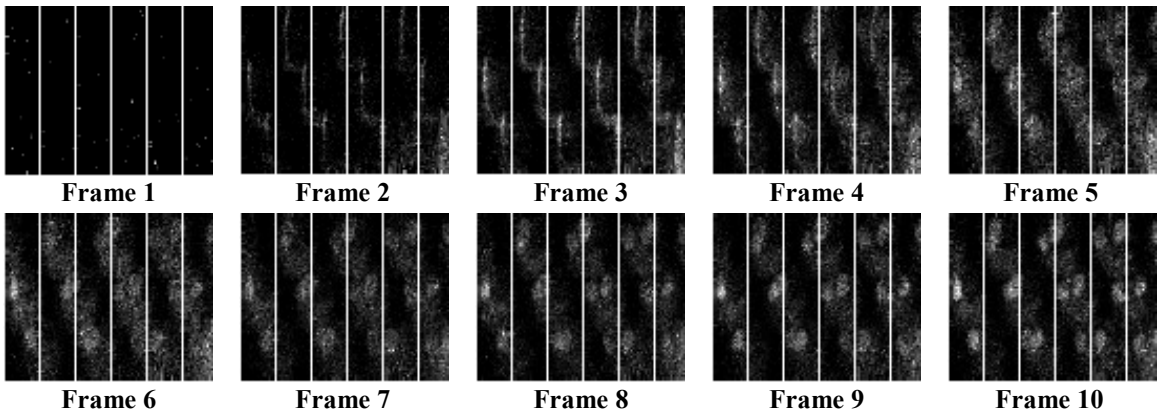


Fig. 3.35. Projection Images from First Ten Frames of MAG3 Study to Reconstruct a Dynamic Image

### **3.3.5.2. Reconstructed SPECT Image of Mouse Kidneys with Tc-99m MAG3 Obtained During Simultaneous SPECT/MR Experiment**

A static SPECT image of the mouse kidney was reconstructed from the static projection acquisition shown in Fig. 3.34. After the SPECT image was reconstructed, the image was rotated and resliced such that the SPECT image would show the kidney at the same orientation in the acquired static MR image. Sample slices of this image are shown in Fig. 3.36, below, along with the corresponding slices of the static MR image of the kidney. Image quality of the SPECT images is comparable to the kidney images seen earlier in Section 3.3.3.

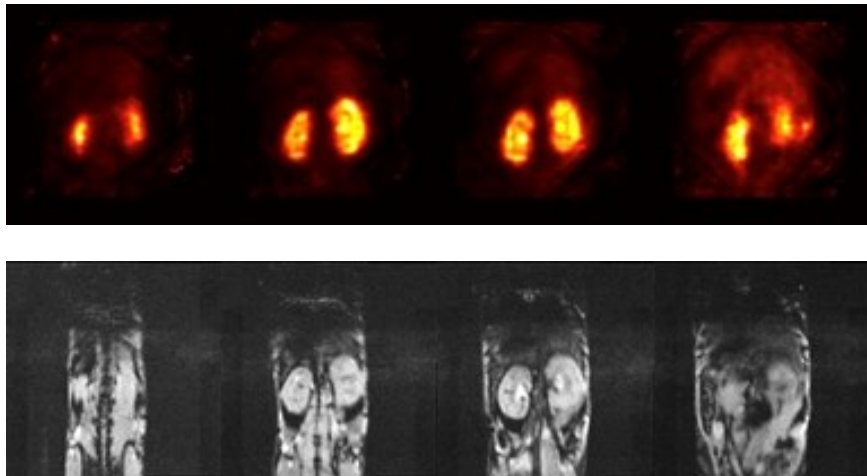


Fig. 3.36. Reconstructed static MAG3 SPECT image of mouse kidneys (top) and MR image of kidneys averaged from 22 dynamic MR frames (bottom)

To generate the dynamic SPECT image, the 180 dynamic projection acquisitions were reconstructed separately to produce a dynamic image with 10 second frame length. The first ten image frames of the image can be seen in Fig. 3.37. As shown, the image shows the initial uptake and later washout of the MAG3. The first few slices of the image show the MAG3 passing up through the tail vein and into the mouse's bloodstream. Soon after, the initial uptake is seen as an image of the kidneys take form. In the complete dynamic image, for the first three minutes, the pixel intensity of the kidneys increases, showing that the amount of MAG3 in the kidneys is still increasing. After this, the pixel intensity begins to decrease because the MAG3 has started washing out of the kidneys. Furthermore, Fig. 3.37 also shows the first three image frame of a sample slice of the acquired MR image. These three frames represent 240 seconds of MR data acquisition. Because we did not use any MR contrast agent during this experiment, the acquired MR image only shows the mouse's anatomy. As such, the image acquired in each time frame does not change.

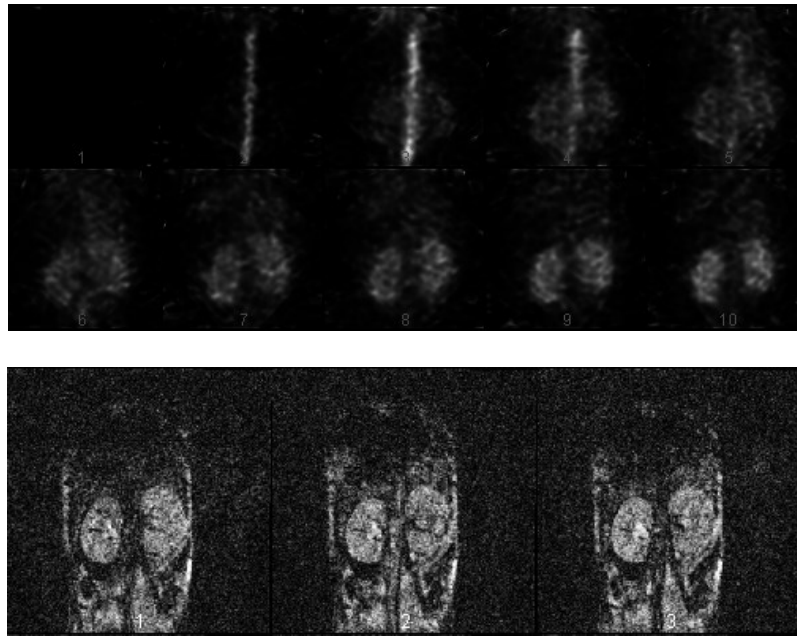


Fig. 3.37. Dynamic Images From SPECT/MR MAG3 study (top) First Ten Frames of Reconstructed SPECT Image (bottom) First Three Frames of Acquired MR Image

### **3.3.5.3. Analysis of Image of Mouse Kidneys with Tc-99m MAG3 Obtained During Simultaneous SPECT/MR Experiment**

As discussed in Section 2.3.5, to determine whether there was any geometric distortion in either the SPECT or MR images due to the simultaneous acquisition, we registered the static SPECT image with the static MR image and then fused the two images together. The resulting fused image can be seen in Fig. 3.38. As shown, there is very good agreement between the SPECT and the MR image, after the images have been registered and fused.

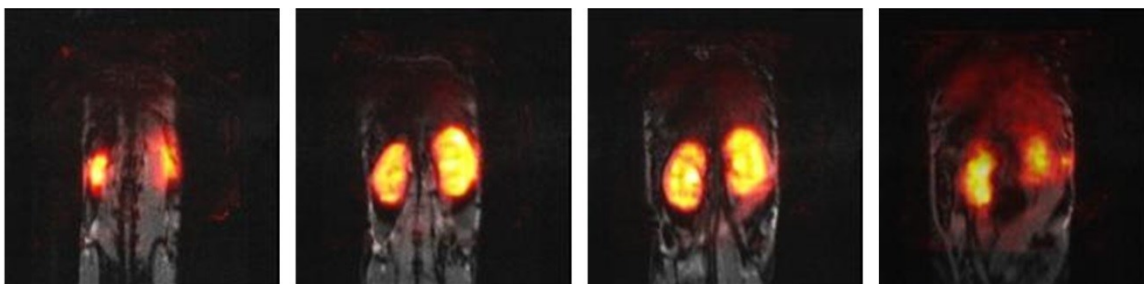


Fig. 3.38. Fusion of static SPECT and MR images from MAG3 experiment.

We also generated a dynamic fused SPECT/MR image, following the procedure described in Section 2.3.5. The resulting dynamic SPECT/MR image can be seen in Fig. 3.39. We again observed very good agreement between the SPECT image and the MR image, after they had been registered and fused, as was expected.

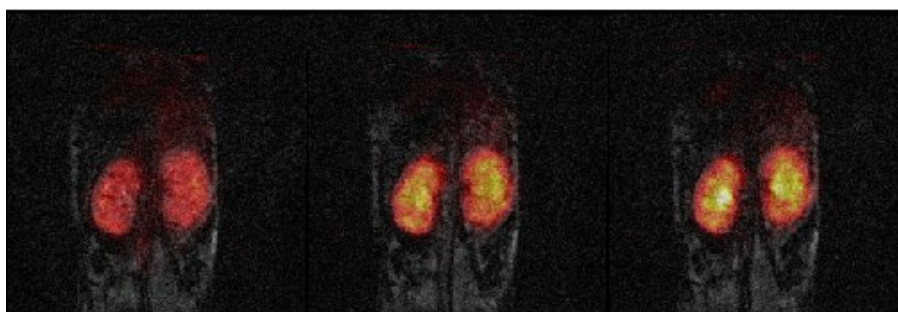


Fig. 3.39. First three frames of fused dynamic SPECT and MR images from MAG3 experiment.

Finally, to study the uptake and washout of the MAG3, a time activity curve was generated using the reconstructed dynamic SPECT image with 10 second time frame, following the method described in Section 2.3.5. The plot for each of the kidneys can be seen in Fig. 3.40. As shown, the peak of the uptake occurs at 200 seconds, after which the MAG3 begins to washout. The time activity curve that was acquired during our experiment was comparable to a time activity curve that we found in the literature [62].



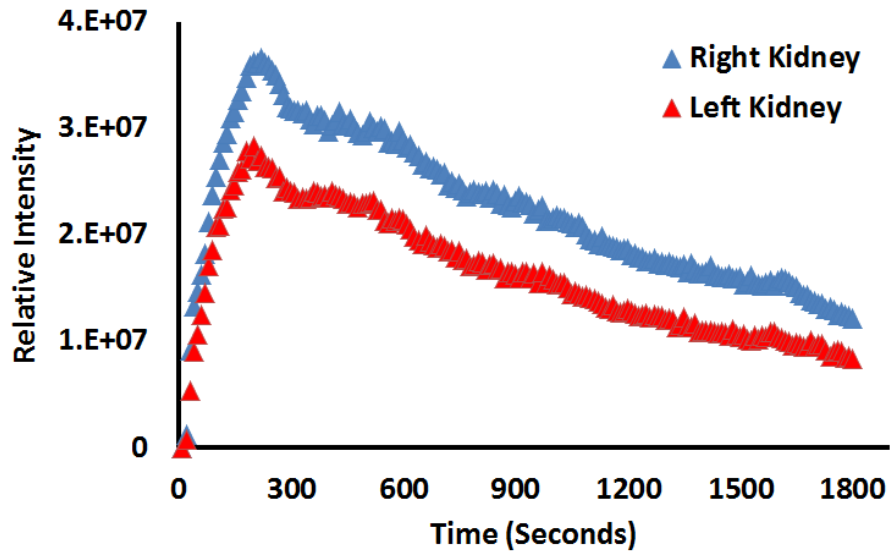


Fig. 3.40. Time activity curve generated from dynamic SPECT/MR Tc-99M MAG3 study.

## **Chapter 4: Discussion and Future Work**

### **4.1. Discussion**

The goal of this dissertation was to discuss key contributions towards the development of an MR compatible SPECT insert capable of simultaneously acquiring SPECT and MR images. These contributions include the development and evaluation of a MPH collimator design method and a system calibration method. As was shown through an initial evaluation of the SPECT/MR system, these two methods played an important role in bringing the SPECT/MR system to a point where it can be used to conduct simultaneous SPECT/MR imaging experiments. Although the SPECT/MR system discussed in this dissertation is not the first to be developed, as far as can be determined by searching through the literature, this SPECT/MR system has the potential to have the highest performance of any current simultaneous SPECT/MR systems due to the system's capability of acquiring images with high resolution while still maintaining a high collimator sensitivity. Previously developed SPECT/MR systems have poorer reconstructed image resolution than our system's reconstructed image resolution. Furthermore, our SPECT/MR system is large enough such that an entire mouse can be inserted into the SPECT/MR system which allows for the imaging of any organ in the mouse's body. The following section will detail the key points in each of the dissertation chapters that described work that was done with the SPECT/MR system.

#### **4.1.1. Discussion of Collimator Design Method**

MPH collimator design is a multiple parameter problem. For a given detector geometry, there are many different possible collimators that can be used. Therefore, as demonstrated, it is very important to develop systematic design methods that allow for

comparison of collimator performance characteristics when different collimator design parameters are changed. Both of the MPH collimator design methods developed in this thesis, the area based method and the model based method, are suited to do this.

The biggest difference between the two collimator design methods, however, is that the model based method also predetermines the pinhole layout to be used when implementing the collimator. Because of this, more realistic estimations can be made in terms of determining the number of pinholes to be used in the collimator as well as the collimator's geometric efficiency at the center of the collimator's CVOV. It should be noted however that for both methods, but especially when using the area based method, the design of the collimator should be evaluated by using a technical drawing program to create a 3D model of the collimator with the parameters determined by the design method used. In addition to allowing us to visually inspect the design of the collimator, the 3D model also allowed us to measure the amount of surface area on the detector used by each pinhole's projection. This was used to calculate the percentage of projection multiplexing between adjacent pinhole projections and ensured that the total amount of multiplexing for each pinhole projection was less than 20%. Finally, it is interesting to note that the two collimator design methods developed can be easily adapted for other SPECT detector ring type geometries.

We used the area based method to design two MPH collimators for the SPECT/MR system. Each collimator was designed for different imaging purposes. The first collimator was designed for high resolution SPECT imaging, while the second collimator was designed for stationary SPECT imaging. The resolutions of both collimators were first evaluated through a simulation study, and later through actual

imaging experiments with a resolution phantom. Simulations and experimental results showed that the HR MPH collimator was capable of obtaining a SPECT image of the resolution phantom where the 0.75 mm segment of the phantom was partially resolved, while the 1 mm segment of the phantom was fully resolved. This suggests that the HR MPH collimator can be used to obtain SPECT images with submillimeter resolution, ranging between with resolution ranging between 0.75 mm and 1 mm, if sufficient number of projection acquisitions is obtained. However, in order to obtain SPECT images free of reconstruction artifacts, it is necessary to rotate the HR MPH collimator to obtain additional projection acquisitions. As of now, at least three projection acquisitions must be obtained in order to reconstruct an image that is free of reconstruction artifacts from the reconstruction. Furthermore, even more projection acquisitions are needed in order to obtain a reconstructed image with submillimeter resolution.

In comparison, the GP MPH collimator has a sufficient number of pinholes such that enough views are obtained to be able to reconstruct a SPECT image free of reconstruction artifacts without having to rotate the collimator to obtain additional projection acquisitions. However, as more pinholes were added to the collimator, each pinhole had to be moved further away from the collimator's field of view. This decreased the magnification of each pinhole and allowed more pinhole projections to cover the detector surface area. However, as magnification decreased, the minimum achievable collimator resolution increased due to the SPECT/MR system's intrinsic resolution. Therefore, the GP MPH collimator could not be designed to have as high of a resolution as the HR MPH collimator. As was shown through simulations and experimental results, the GP MPH collimator's resolution ranges between 1 mm and 1.35 mm.

After we had determined the final design parameters for the High Resolution and GP MPH collimators, we implemented MR compatible prototypes of both collimators. These collimators were implemented entirely out of nonmagnetic materials so that they could be taken safely into an MRI system's operating room for simultaneous SPECT/MR imaging.

#### **4.1.2. Discussion of System Calibration Method**

As was shown in this dissertation, system calibration is a very important aspect of the development of an imaging system. Without proper system calibration, the quality of the images acquired by the system will be degraded. In fact, system calibration can improve a reconstructed SPECT image's contrast and resolution, and also significantly decrease the artifacts seen in the image. In this dissertation, we discussed both an energy calibration method and detector uniformity correction method. Additionally, we also demonstrated a simple correction for the drift in charged particles in the SPECT/MR system's detector modules, which is caused by the Lorentz force during simultaneous SPECT/MR image acquisition.

Our SPECT/MR system acquires data in a list-mode format. Each pixel of the system's detector records the entire energy spectrum of detected photons. The range of energies of detected photons used to generate an acquired projection image is determined during post processing, rather than while experimental data is being acquired. Therefore, it is very important to be able to identify the photopeak of the isotope that is being used through careful energy calibration. This allows us to only include nonscattered photons in the projection image. As shown, energy calibration improves the contrast of reconstructed images. In order to identify the photopeak of each detector pixel, we

measured the energy spectra of each pixel using a cylindrical shell phantom. This phantom allowed us to measure the energy spectra while minimal scattered photons were acquired. In turn, this made it possible to identify the location of each pixel's photopeak systematically. The location of each pixel's photopeak were used to store unique energy windows for each pixel which were then used to process experimental data and properly reject scattered photons that were acquired by the detector during experimental data acquisition. In a phantom study, the developed energy calibration improved the contrast of reconstructed SPECT image by 26%.

This dissertation also discussed the development and evaluation of a detector uniformity calibration method. Using the cylindrical shell phantom, we were able to measure the sensitivity of each of the detector pixels. If not corrected for, non-uniformities in the projection image caused by variations in detector pixel sensitivity would introduce artifacts in the reconstructed SPECT image. Data acquired using the cylindrical shell phantom was used to generate a uniformity correction map which was applied to acquired experimental data in order to remove non-uniformities from the projection image. However, ~2.5% of the pixels in projection images of acquired experimental data were not properly corrected by the uniformity correction map. This is because they were either dead, malfunctioning, hypoactive, or hyperactive. To correct for these pixels, their pixel values were replaced by interpolation from surrounding pixel values. After these two stages of detector uniformity were completed, experimental results showed that image quality of reconstructed images was substantially improved. Without the system calibration method developed, any reconstructed SPECT images obtained by the SPECT/MR system were dominated by artifacts.

Finally, this dissertation also discussed how the calibration method was adapted for acquisition of SPECT images during simultaneous SPECT/MR experiments. While the calibration method is largely the same, one additional step must be taken. Pixel values must be shifted to take into account the drift of charged particles in the detector modules during experimental data acquisition. After correcting for this drift, image quality of experimental images is significantly improved.

#### **4.1.3. Discussion of Experimental Evaluation**

Several imaging experiments were conducted to evaluate the performance of the SPECT/MR system. Each of the experiments demonstrates a different feature of the SPECT/MR system. For instance, the resolution phantom imaging experiment and the MDP mouse skull imaging experiment both demonstrate that high resolution images can be obtained when using the HR MPH collimator. The resolution phantom imaging experiment also shows that the GP MPH collimator can be used to obtain a SPECT without having to rotate the collimator while still reaching the system resolution that the collimator was designed for. We also conducted a kidney imaging experiment using gadolinium nanoparticles labeled with Tc-99m in order to study their potential use as an agent for simultaneous SPECT/MR imaging. This experiment also showed us that we could acquire a high quality image of a mouse's kidney when using the GP MPH collimator when acquiring data for a short period of time. The image shown was reconstructed from data that was only acquired for five minutes.

Most importantly, however, were the simultaneous SPECT/MR phantom and mouse experiments. The simultaneous SPECT/MR imaging experiment showed us that we could in fact acquire SPECT and MR images simultaneously. The SPECT image

acquired of the Ultra Micro Hot Spot phantom had image quality that was comparable to the image of the phantom that was acquired in our laboratory during standalone SPECT data acquisition. When fused together, the SPECT and MR images of the Ultra Micro Hot Spot phantom that were acquired simultaneously had good agreement with each other. Additionally, the simultaneous SPECT/MR mouse kidney experiment demonstrated that the system was capable of acquiring high quality SPECT images and MR images during an actual preclinical experiment. This experiment demonstrated that the system can also be used to acquire fast dynamic SPECT images with the GP MPH collimator. Data acquired during this study was used to generate projection acquisitions containing only 10 seconds of acquired data. Although these images were noisy, we were able to reconstruct reasonable quality SPECT images from these projection sets, to generate a dynamic SPECT image.

#### **4.1.4. Significant Contributions**

As discussed, the work in this dissertation was part of a larger project: the development of the world's first MR compatible SPECT insert capable of obtaining high resolution SPECT images of any part of a mouse. When this insert is placed into an MR system, high quality SPECT and MR images can be obtained simultaneously. The specific contributions of this dissertation to the overall project fall into three main categories: SPECT MPH collimator design, SPECT system calibration, and SPECT/MR system experimental evaluation.

The following section will discuss the significant contributions made over the course of this project. First, as discussed, the collimator is an integral piece of hardware for any SPECT imaging system. Without the development of the MPH collimators



discussed in this dissertation, our SPECT/MR system would not have been able to acquire SPECT images. The simulations conducted allowed us to evaluate the imaging performance of both collimators prior to their implementation, and the positive simulation results gave us the confidence needed to move the collimators from the design stage to the implementation stage. As demonstrated, we developed a method to fabricate MR compatible MPH collimators, and we were able to use these collimators to acquire projection images with our SPECT/MR system.

Although the model based method for evaluating cylindrical MPH collimator design parameters was not used to design the prototype MPH collimators, it provided useful insights into the problem and will be a very helpful tool going forward in future designs. For example, this method is very robust, and can be used for design of MPH collimators for any sort of ring detector system. In fact, we are currently in the early stages of designing a new ring type detector system, and the model based method is being used to design the MPH collimators for the system.

The development of a repeatable system calibration for the SPECT/MR system was another significant contribution of this work. In addition to being repeatable, the developed system calibration method is also relatively straightforward to perform. All measurements needed are obtained from a single imaging experiment, that is, the acquisition of the flood image using the annular shell phantom. Without the system calibration method, as shown earlier, reconstructed SPECT image quality from the acquired experimental projection images have very poor image quality. This was demonstrated through a series of phantom studies, which show how SPECT image quality improves as the different steps of the system calibration method are applied.

After the development of MPH collimators and a system calibration method for the SPECT/MR system, the performance of the system was evaluated through both phantom and small animal studies. As was shown, we conducted rigorous phantom studies with both collimators designed for the system. The results of the phantom studies showed that the collimators could obtain SPECT images at their designed resolution, and also showed us the minimum number of collimator rotations needed to obtain artifact free SPECT images with each collimator. Furthermore, this phantom study allowed us to validate our simulation results.

We also performed a SPECT/MR phantom study which showed that SPECT images could be acquired during simultaneous SPECT/MR imaging. The image quality and resolution of the phantom image matched closely with phantom images acquired during a standalone SPECT acquisition demonstrating.

Finally, the dynamic SPECT/MR imaging experiment using Tc-99m MAG3 to image a mouse's kidneys ties all aspects of the project together and can be considered a capstone to the project. This experiment demonstrated that we could obtain simultaneous SPECT/MR images of a live animal with our SPECT/MR system, with minimal distortion to both the SPECT and MR image. Additionally, to obtain a dynamic image of the uptake and washout of the Tc-99m MAG3 into and out of the kidney, we binned the acquired list-mode data into 10 second frames and reconstructed each frame separately. We were able to do this because of the design of the GP MPH collimator. The dynamic SPECT image obtained from this study demonstrates that the GP MPH collimator can be used to obtain artifact free SPECT images without additional collimator rotations, as the collimator was designed for. Furthermore, without the development of the system

calibration method, the SPECT kidney image would have had significantly poorer image quality. When applied to data acquired in the presence of a strong magnetic field, the developed system calibration method corrects for both non-uniformities as well as the drift of charged particles in the detector module due to the Lorentz force.

#### **4.1.5. Future Work**

Although much has been done to bring the SPECT/MR insert to its current state, there are still many areas where work on the system can be continued. Areas of future work include improving the SPECT/MR hardware, gaining a better understanding of how the SPECT/MR insert and the MR system interact with each other, and continuation of preclinical experiments to find procedures that take advantage of being able to acquire SPECT and MR image data simultaneously.

Manufacturing new MPH collimators is one area where work on the SPECT/MR hardware can continue. The MPH collimators that were discussed were designed to have a spherical field-of-view of 30 mm. While this field-of-view size is sufficient for imaging mice, it is too small to image a rat. Either of the collimator design methods discussed could be used to design collimators with a larger field-of-view to allow for rat imaging without truncation of any parts of the rat's body. However, to account for the larger MR RF coil that we be needed for MR imaging of a rat, the collimator sleeve will have to have a larger diameter to still allow the coil to fit inside the collimator. This could potentially limit the imaging resolution of the collimator because of the fixed intrinsic resolution of the SPECT/MR insert's detector. Fortunately, because rats are larger in size than mice, a high resolution collimator designed to image rats would not need to have as high a resolution as a high resolution collimator designed to image mice.

In addition to manufacturing collimators with a larger field-of-view, it would also be interesting to design collimators that can image radioisotopes that emit higher energy photons than Tc-99m does. For instance, we once attempted to image a mouse's brain using a drug called DATSCAN [64], which is labeled with I-123. However, I-123 emits gamma photons with energy of 159 keV. After processing the acquired data, we found that the collimator did not have sufficient shielding to block photons and we had significant radiation leakage through the walls of the collimator shell. Very recently, a new company has developed an additive manufacturing method that can be used to manufacture complex structures out of solid tungsten. Unlike the high density tungsten powder used for our current collimator shielding, the material used in the additive manufacturing method has density that is 89% of tungsten. Furthermore, the company has shown that the material used in this manufacturing process is MR compatible [65]. If this method was used to manufacture high energy collimators, 4 mm of the material used would be sufficient to block 99.99% of photons emitted from I-123. This additive manufacturing method would simplify the collimator manufacturing process. Instead of building separate solid tungsten inserts to fit into a plastic shell, all parts of the collimator could be built using additive manufacturing. Another advantage that additive manufacturing would have over the current collimator manufacturing method is that, after repeated use, it has been observed that a small portion of the high density tungsten powder used as shielding settled. As a result, tiny radiation leaks in the collimator shielding have occurred. A collimator made using the additive manufacturing method would not have this issue.

Another aspect of this project that has potential for further research is the method used for correcting for the Lorentz force drift. While shifting each pixel in the projection image in the direction opposite of the drift significantly reduces artifacts in the reconstructed SPECT image, shifting all pixels by the same amount is only a first order correction that shifts by the average drift caused by the Lorentz force. Not all charged particles in the CZT modules drift by the same amount. The amount that a charged particle drifts depends on the depth at which the interaction that created the charged particle occurs. The deeper the interaction occurs, the less the amount of drift. This is because a charged particle created deeper in the CZT module will travel less inside the module before it reaches the CZT module's anode. A better correction for the effect that the Lorentz force has on the CZT modules in the SPECT/MR detector could be developed by using a Monte Carlo method to create a distribution for the depth dependent drift. This information could be used to further improve the reconstructed images acquired during simultaneous SPECT/MR experiments.

The most important work to be continued, however, is to better understand how the SPECT/MR insert interacts with the MR system when the insert has been taken into the MR system. During simultaneous SPECT/MR experiments, we observed that simply the presence of the SPECT/MR insert decreases the MR system's SNR. The SNR decreases even further when the SPECT/MR insert is active. This loss in SNR limits the pulse sequences that can be used. For instance, higher SNR would allow us to use pulse sequences that acquire images at a faster rate, and potentially allow us to acquire fast MR dynamic images. Although improvement in the shielding decreases the SNR loss, there are still other interactions that the SPECT/MR system has with the MR system that are

still not entirely understood. For instance, we have observed some geometric distortions with the MR acquisition which causes some issues when trying to obtain a particular slice in the transaxial direction. Future work to better understand and characterize these distortions through calibration experiments could be conducted.

Additionally, the MR system also affects the performance of the SPECT/MR insert in ways that are still not entirely understood. During data acquisition using the annular cylindrical shell, we have noticed that the count rate of the SPECT/MR system was significantly less than what was expected. Future studies could be conducted to better understand why the decrease in count rate occurs, and whether there is any potential way to stop this from happening.

Finally, further preclinical experiments that take advantage of simultaneous SPECT/MR data acquisition can be conducted. The gadolinium nanoparticles labeled with Tc-99m showed initial promise during the standalone SPECT imaging experiment discussed in Chapter 3. Using the nanoparticles as a contrast agent for an MR image while also acquiring a SPECT image is potentially a good starting point for further simultaneous SPECT/MR preclinical studies.

## References

- [1] S. R. Cherry, "Multimodality imaging: beyond PET/CT and SPECT/CT," *Semin Nucl Med*, vol. 39, pp. 348-53, Sep 2009.
- [2] P. E. Kinahan, *et al.*, "Attenuation correction for a combined 3D PET/CT scanner," *Med Phys*, vol. 25, pp. 2046-53, Oct 1998.
- [3] B. H. Hasegawa, *et al.*, "Description of a Simultaneous Emission-Transmission Ct System," *Medical Imaging Iv : Image Formation*, vol. 1231, pp. 50-60, 1990.
- [4] T. F. Lang, *et al.*, "Description of a Prototype Emission-Transmission Computed-Tomography Imaging-System," *Journal of Nuclear Medicine*, vol. 33, pp. 1881-1887, Oct 1992.
- [5] T. Beyer, *et al.*, "A combined PET/CT scanner for clinical oncology," *J Nucl Med*, vol. 41, pp. 1369-79, Aug 2000.
- [6] D. W. Townsend and T. Beyer, "A combined PET/CT scanner: the path to true image fusion," *Br J Radiol*, vol. 75 Spec No, pp. S24-30, Nov 2002.
- [7] D. W. Townsend, *et al.*, "PET/CT today and tomorrow," *J Nucl Med*, vol. 45 Suppl 1, pp. 4S-14S, Jan 2004.
- [8] O. Schillaci, "Hybrid SPECT/CT: a new era for SPECT imaging?," *Eur J Nucl Med Mol Imaging*, vol. 32, pp. 521-4, May 2005.
- [9] A. K. Buck, *et al.*, "Spect/Ct," *Journal of Nuclear Medicine*, vol. 49, pp. 1305-1319, Aug 2008.

- [10] G. Delso, *et al.*, "Performance measurements of the Siemens mMR integrated whole-body PET/MR scanner," *J Nucl Med*, vol. 52, pp. 1914-22, Dec 2011.
- [11] H. Zaidi, *et al.*, "Design and performance evaluation of a whole-body Ingenuity TF PET-MRI system," *Phys Med Biol*, vol. 56, pp. 3091-106, May 21 2011.
- [12] W. D. Heiss, "The potential of PET/MR for brain imaging," *European Journal of Nuclear Medicine and Molecular Imaging*, vol. 36, pp. 105-112, Mar 2009.
- [13] D. J. Wagenaar, *et al.*, "Rationale for the combination of nuclear medicine with magnetic resonance for pre-clinical imaging," *Technology in Cancer Research & Treatment*, vol. 5, pp. 343-350, Aug 2006.
- [14] B. Fei, *et al.*, "An MRI-based Attenuation Correction Method for Combined PET/MRI Applications," *Proc SPIE*, vol. 7262, Feb 27 2009.
- [15] S. R. Cherry, *et al.*, *Physics in Nuclear Medicine Third Edition*. Philadelphia: Saunders, 2003.
- [16] G. L. Zeng, *et al.*, "Single-Photon Emission Computed Tomography," in *Emission Tomography: The Fundamentals of PET and SPECT*, M. N. Wernick and J. N. Aarsvold, Eds., ed San Diego: Elsevier Academic Press, 2004.
- [17] J. L. Prince and J. M. Links, *Medical Imaging Signals and Systems*: Pearson Prentice Hall, 2006.
- [18] D. S. Lalush and M. N. Wernick, "Iterative Image Reconstruction," in *Emission Tomography: The Fundamentals of PET and SPECT*, M. N. Wernick and J. N. Aarsvold, Eds., ed San Diego: Elsevier Academic Press, 2004, pp. 443-467.



- [19] F. Beekman and F. van der Have, "The pinhole: gateway to ultra-high-resolution three-dimensional radionuclide imaging," *Eur J Nucl Med Mol Imaging*, vol. 34, pp. 151-61, Feb 2007.
- [20] F. J. Beekman and B. Vastenhouw, "Design and simulation of a high-resolution stationary SPECT system for small animals," *Phys Med Biol*, vol. 49, pp. 4579-92, Oct 7 2004.
- [21] F. P. Difilippo, "Design and performance of a multi-pinhole collimation device for small animal imaging with clinical SPECT and SPECT-CT scanners," *Phys Med Biol*, vol. 53, pp. 4185-201, Aug 7 2008.
- [22] D. P. McElroy, *et al.*, "Performance evaluation of A-SPECT: A high resolution desktop pinhole SPECT system for imaging small animals," *Ieee Transactions on Nuclear Science*, vol. 49, pp. 2139-2147, Oct 2002.
- [23] K. Vunckx, *et al.*, "Single and multipinhole collimator design evaluation method for small animal SPECT," *Ieee Transactions on Medical Imaging*, vol. 27, pp. 36-46, Jan 2008.
- [24] R. J. Jaszczak, *et al.*, "Pinhole collimation for ultra-high-resolution, small-field-of-view SPECT," *Phys Med Biol*, vol. 39, pp. 425-37, Mar 1994.
- [25] R. Accorsi and S. D. Metzler, "Analytic determination of the resolution-equivalent effective diameter of a pinhole collimator," *IEEE Trans Med Imaging*, vol. 23, pp. 750-63, Jun 2004.

- [26] S. D. Metzler, *et al.*, "Analytic determination of pinhole collimator sensitivity with penetration," *Ieee Transactions on Medical Imaging*, vol. 20, pp. 730-741, Aug 2001.
- [27] R. Van Holen, *et al.*, "Design and performance of a compact and stationary microSPECT system," *Medical Physics*, vol. 40, 2013.
- [28] D. J. Wagenaar, *et al.*, "Advantages of semiconductor CZT for medical imaging - art. no. 67070I," *Penetrating Radiation Systems and Applications Viii*, vol. 6707, pp. I7070-I7070, 2007.
- [29] D. J. Griffiths, *Introduction to Electrodynamics*. Prentice Hall, 1999.
- [30] J. W. Tan, *et al.*, "Experimental study of the response of CZT and CdTe detectors of various thicknesses in strong magnetic field," *Nuclear Instruments & Methods in Physics Research Section a-Accelerators Spectrometers Detectors and Associated Equipment*, vol. 652, pp. 153-157, Oct 1 2011.
- [31] S. Azman, *et al.*, "A nuclear radiation detector system with integrated readout for SPECT/MR small animal imaging," *2007 Ieee Nuclear Science Symposium Conference Record, Vols 1-11*, pp. 2311-2317, 2007.
- [32] A. Seret and F. Bleeser, "Intrinsic uniformity requirements for pinhole SPECT," *J Nucl Med Technol*, vol. 34, pp. 43-7, Mar 2006.
- [33] G. T. Gullberg, "An analytical approach to quantify uniformity artifacts for circular and noncircular detector motion in single photon emission computed tomography imaging," *Med Phys*, vol. 14, pp. 105-14, Jan-Feb 1987.

- [34] L. A. Shepp and Y. Vardi, "Maximum likelihood reconstruction for emission tomography," *IEEE Trans Med Imaging*, vol. 1, pp. 113-22, 1982.
- [35] K. Lange and R. Carson, "EM reconstruction algorithms for emission and transmission tomography," *Journal of computer assisted tomography*, vol. 8, pp. 306-16, 1984.
- [36] B. F. Hutton, *et al.*, "Iterative Reconstruction Methods," in *Quantitative Analysis in Nuclear Medicine Imaging*, H. Zaidi, Ed., ed New York: Springer Science, 2006, pp. 110-140.
- [37] A. P. Dempster, *et al.*, "Maximum Likelihood from Incomplete Data Via Em Algorithm," *Journal of the Royal Statistical Society Series B-Methodological*, vol. 39, pp. 1-38, 1977.
- [38] S. C. Bushong, *Magnetic Resonance Imaging Physical and Biological Principles Second Edition*. St. Louis: Mosby, 1996.
- [39] S. Ha, *et al.*, "Development of a new RF coil and gamma-ray radiation shielding assembly for improved MR image quality in SPECT/MRI," *Phys Med Biol*, vol. 55, pp. 2495-504, May 7 2010.
- [40] M. J. Hamamura, *et al.*, "Development of an MR-compatible SPECT system (MRSPECT) for simultaneous data acquisition," *Phys Med Biol*, vol. 55, pp. 1563-75, Mar 21 2010.

- [41] L. J. Meng, *et al.*, "Design study of an MRI compatible ultra-high resolution SPECT for in vivo mice brain imaging," *2007 Ieee Nuclear Science Symposium Conference Record, Vols 1-11*, pp. 2956-2960, 2007.
- [42] J. W. Tan, *et al.*, "A Prototype of the MRI-Compatible Ultra-High Resolution SPECT for in Vivo Mice Brain Imaging," *2009 Ieee Nuclear Science Symposium Conference Record, Vols 1-5*, pp. 2800-2805, 2009.
- [43] R. Van Holen and S. Vandenberghe, "Optimization of a stationary small animal SPECT system for simultaneous SPECT/MRI," *2013 Ieee Nuclear Science Symposium and Medical Imaging Conference (Nss/Mic)*, 2013.
- [44] M. R. Bernsen, *et al.*, "The role of preclinical SPECT in oncological and neurological research in combination with either CT or MRI," *European Journal of Nuclear Medicine and Molecular Imaging*, vol. 41, pp. S36-S49, May 2014.
- [45] D. Salvado, *et al.*, "Collimator Design for a Brain SPECT/MRI Insert," *Ieee Transactions on Nuclear Science*, vol. 62, pp. 1716-1724, Aug 2015.
- [46] K. Van Audenhaege, *et al.*, "Design and simulation of a full-ring multi-lofthole collimator for brain SPECT," *Physics in Medicine and Biology*, vol. 58, pp. 6317-6336, Sep 21 2013.
- [47] D. Meier, *et al.*, "Development of Pre-Clinical SPECT for MRI," *World Congress on Medical Physics and Biomedical Engineering, Vol 25, Pt 2 - Diagnostic Imaging*, vol. 25, pp. 798-801, 2009.

- [48] D. Meier, *et al.*, "A SPECT Camera for Simultaneous SPECT/MRI," *2009 Ieee Nuclear Science Symposium Conference Record, Vols 1-5*, pp. 2313-2318, 2009.
- [49] B. M. W. Tsui, *et al.*, "Design and Development of MR-Compatible SPECT Systems for Simultaneous SPECT-MR Imaging of Small Animals," *Medical Imaging 2011: Physics of Medical Imaging*, vol. 7961, 2011.
- [50] B. M. W. Tsui, *et al.*, "High Performance SPECT system for Simultaneous SPECT-MR Imaging of Small Animals," *2011 Ieee Nuclear Science Symposium and Medical Imaging Conference (Nss/Mic)*, pp. 3178-3182, 2011.
- [51] G. S. Mok, *et al.*, "Quantification of the Multiplexing Effects in Multi-Pinhole Small Animal SPECT: A Simulation Study," *IEEE Trans Nucl Sci*, vol. 56, pp. 2636-2643, 2009.
- [52] G. S. P. Mok, *et al.*, "The effects of object activity distribution on multiplexing multi-pinhole SPECT," *Physics in Medicine and Biology*, vol. 56, pp. 2635-2650, Apr 21 2011.
- [53] M. C. M. Rentmeester, *et al.*, "Optimizing multi-pinhole SPECT geometries using an analytical model," *Physics in Medicine and Biology*, vol. 52, pp. 2567-2581, May 7 2007.
- [54] P. Nillius and M. Danielsson, "Theoretical Bounds and System Design for Multipinhole SPECT," *Ieee Transactions on Medical Imaging*, vol. 29, pp. 1390-1400, Jul 2010.

- [55] J. Y. Xu, *et al.*, "SPECT Data Acquisition and Image Reconstruction in a Stationary Small Animal SPECT/MRI System," *Medical Imaging 2010: Physics of Medical Imaging*, vol. 7622, 2010.
- [56] *Ultra-Micro Phantoms*. Available:  
[http://www.spect.com/pub/Ultra\\_Micro\\_Hot\\_Spot\\_and\\_Defrise\\_Phantoms.pdf](http://www.spect.com/pub/Ultra_Micro_Hot_Spot_and_Defrise_Phantoms.pdf)
- [57] W. P. Segars, *et al.*, "Development of a 4-D digital mouse phantom for molecular imaging research," *Molecular Imaging and Biology*, vol. 6, pp. 149-159, May-Jun 2004.
- [58] A. I. Brenner, *et al.*, "The bone scan," *Seminars in nuclear medicine*, vol. 42, pp. 11-26, 2012.
- [59] S. Jan, *et al.*, "GATE: a simulation toolkit for PET and SPECT," *Physics in Medicine and Biology*, vol. 49, pp. 4543-4561, Oct 7 2004.
- [60] A. M. Samoudi, *et al.*, "Analysis of eddy currents induced by transverse and longitudinal gradient coils in different tungsten collimators geometries for SPECT/MRI integration," *Magn Reson Med*, Nov 26 2014.
- [61] A. Piepsz, *et al.*, "Measurement of Separate Kidney Clearance by Means of Tc-99m-Dtpa Complex and a Scintillation Camera," *European Journal of Nuclear Medicine*, vol. 2, pp. 173-177, 1977.
- [62] M. N. Tantawy, *et al.*, "Assessment of renal function in mice with unilateral ureteral obstruction using 99mTc-MAG3 dynamic scintigraphy," *BMC nephrology*, vol. 13, p. 168, 2012.

- [63] A. Rittenbach, *et al.*, "Continuing Evaluation of an MR Compatible SPECT Insert for Simultaneous SPECT-MR Imaging of Small Animals," *2013 Ieee Nuclear Science Symposium and Medical Imaging Conference (Nss/Mic)*, 2013.
- [64] A. Antonini and R. DeNotaris, "PET and SPECT functional imaging in Parkinson's disease," *Sleep Medicine*, vol. 5, pp. 201-206, Mar 2004.
- [65] K. Deprez, *et al.*, "Rapid additive manufacturing of MR compatible multipinhole collimators with selective laser melting of tungsten powder," *Medical Physics*, vol. 40, Jan 2013.

## **Curriculum Vitae**

### **Journal Publications**

C. Chang, A. Chan, X. Lin, T. Higuchi, J. Terrovitis, J. Afzal, **A. Rittenbach**, D. Sun, S. Vakrou, K. Woldemichael, B. O'Rourke, R. Wahl, M. Pomper, B. Tsui, M. Abraham, "Cellular Bioenergetics Is an Important Determinant of the Molecular Imaging Signal Derived From Luciferase and the Sodium-Iodide Sympporter," *Circulation Research*. 112(3) 2013: 441-450.

### **Conference Proceedings**

**A. Rittenbach**, J. Xu, A. El-Sharkawy, W. Edelstein, K. Parnham, J. Hugg, B. Tsui, "Continuing evaluation of an MR compatible SPECT insert for simultaneous SPECT-MR imaging of small animals," *Nuclear Science Symposium and Medical Imaging Conference (NSS/MIC)*, 2013 IEEE.

**A. Rittenbach**, J. Xu, B. Tsui, "Acquisition strategies of a dual head rotating 4-Segment Slant-Hole (R4SSH\_ SPECT System for Improved Myocardial Perfusion SPECT Imaging," *Nuclear Science Symposium and Medical Imaging Conference (NSS/MIC)*, 2011 IEEE.

**A. Rittenbach**, J. Xu, J. Hugg, B. Tsui, "The design of optimal MPH collimators for a seamless SPECT detector ring," *Nuclear Science Symposium and Medical Imaging Conference (NSS/MIC)*, 2011 IEEE.



B. Tsui, J. Xu, **A. Rittenbach**, S. Chen, A. El-Sharkawy, W. Edelstein, X. Guo, A. Liu, J. Hugg, "High Performance SPECT system for simultaneous SPECT-MR imaging of small animals," *Nuclear Science Symposium and Medical Imaging Conference (NSS/MIC), 2011 IEEE*.

### **Conference Abstracts**

**A. Rittenbach**, C. Wu, F. Beekman, B. Tsui, "Uniformity Correction of a Small Animal SPECT System with Spiral Step Data Acquisition," *J Nucl Med*. 2015; 56 (Supplement 3): 1807.

**A. Rittenbach**, J. Xu, C. Liu, M. Razavian, M. Sadeghi, B. Tsui, "Application of a direction regional activity characterization approach to focal uptake activity quantification in pinhole SPECT," *J Nucl Med*. 2014; 55 (Supplement 1):2119.

B. Tsui, J. Xu, **A. Rittenbach**, A. Fabbri, V. Cencelli, "Limited-Angle Low Dose SPECT Imaging of Small Organs and Pediatric Patients Using a Low-Cost High Performance Compact Camera," Poster presentation *at the 2013 IEEE Nuclear Science Symposium and Medical Imaging Conference (NSS/MIC), Seoul, Korea, October 27 - November 2, 2013*.

A. Fabbri, V. Cencelli, J. Xu, **A. Rittenbach**, M. Galasso, B. Tsui, "Sub-millimeter resolution SPECT using a low-cost compact camera based on a continuous NaI(Tl) crystal and PSPMT array," *J Nucl Med*. 2013; 54 (Supplement 2):2161.

**A. Rittenbach**, J. Xu, K. Parnham, J. Hugg, B. Tsui, “System Characterization of a CZT detector Based MR Compatible Small Animal SPECT System,” Poster presentation *at the 2012 IEEE Nuclear Science Symposium and Medical Imaging Conference (NSS/MIC), Anaheim, California, October 29 - November 3, 2012.*

**A. Rittenbach**, J. Xu, A. El-Sharkawy, W. Edelstein, A. Liu, K. Parnham, J. Hugg, B. Tsui, “System calibration method for a CZT detector based ring-type small animal SPECT system,” J Nucl Med. 2012; 53 (Supplement 1):2392.

B. Tsui, J. Xu, **A. Rittenbach**, A. El-Sharkawy, W. Edelstein, A. Liu, K. Parnham, J. Hugg, “The development of a high-resolution insert for simultaneous SPECT-MR imaging of small animals,” J Nucl Med. 2012; 53 (Supplement 1):2401.

B. Tsui, J. Hugg, J. Xu, **A. Rittenbach**, S. Chen, A. El-Sharkawy, W. Edelstein, X. Gui, A. Liu, “A High-Resolution SPECT System for SPECT-MR Imaging of Small Animals,” Poster presentation *at the 2011 World Molecular Imaging Congress, San Diego, CA, September 7-10, 2011.*

**A. Rittenbach**, J. Xu, A. Liu, J. Hugg, B. Tsui, “The design and evaluation of optimal MPH collimators for a SPECT-MR system,” J Nucl Med. 2011; 52 (Supplement 1):1951.

**A. Rittenbach**, J. Xu, S. Chen, L. Shao and B. Tsui, “The Optimal Design and Evaluation of a RMSVASH Collimator for Clinical Myocardial Perfusion SPECT.”

Poster presentation *at the 2010 IEEE Nuclear Science Symposium and Medical Imaging Conference (NSS/MIC), Knoxville, TN, October 29 - November 3, 2012.*

### **Invited Talks**

**A. Rittenbach**, J. Xu, A. El-Sharkawy, W. Edelstein, K. Parnham, J. Hugg, B. Tsui, “Collimator Design, System Calibration, and Initial Evaluation of an MR Compatible SPECT System for Simultaneous SPECT/MR Imaging of Small Animals,” *Presented at NIST Seminar Series, Gaithersburg, MD, December 2014.*

**A. Rittenbach**, J. Xu, A. El-Sharkawy, W. Edelstein, A. Liu, K. Parnham, J. Hugg, B. Tsui, “System calibration method for a CZT detector based ring-type small animal SPECT system,” *Presented at the 2012 Workshop on Small Animal SPECT Imaging, Tucson, AZ, November 2012.*

**A. Rittenbach**, X. Li, J. Xu, J. Hugg, B. Tsui, “The Design and Evaluation of Optimal MPH Collimators for Two Ring-Type Small Animal SPECT systems,” *Presented at the 2010 Workshop on Small Animal SPECT Imaging, Tucson, AZ, December 2010.*

Andrew Rittenbach was born on January 24<sup>th</sup>, 1987 in Point Pleasant, NJ. He obtained a BE in Electrical Engineering at the Cooper Union for the Advancement of Science and Arts in 2009, graduating cumma sum laude. In the fall of 2009, he moved to Baltimore and joined the Department of Electrical Engineering at Johns Hopkins University and became a graduate research assistant in the Division of Medical Imaging Physics. He received an MS in Electrical Engineering from Johns Hopkins University in 2011. Andrew's research interests include SPECT collimator optimization, SPECT and PET system calibration, and preclinical SPECT and PET imaging.